Charles University in Prague
Faculty of Mathematics and Physics

DOCTORAL THESIS

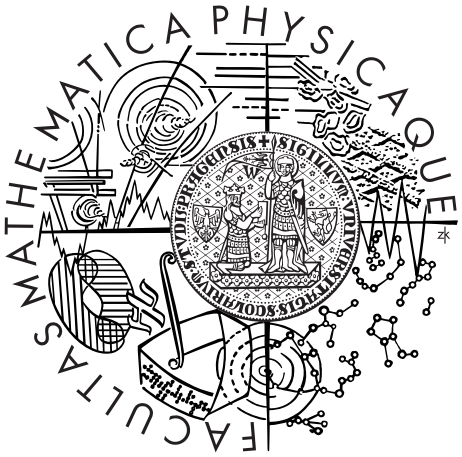

Zbyněk Drásal

Measurement of Time-Dependent CP Violation in $B^0 \to \eta_c K^0_S$ at Belle Experiment, Optimisation Studies of the Belle II Vertex Detector

Institute of Particle and Nuclear Physics

Supervisor: Dr. Zdeněk Doležal
Study programme: Subnuclear Physics

Prague 2013

Věnováno mamince.
Dedicated to my mother.

Velice rád bych využil této příležitosti a poděkoval všem, díky nimž jsem se mohl aktivně zapojit do vývoje vrcholového dráhového detektoru pro experiment Belle II a zároveň bych jim chtěl poděkovat za jedinečnou příležitost, díky níž jsem mohl spolupracovat s vědci z celého světa v jedné z vedoucích výzkumných laboratoří světa, KEKu (Japonsko), a podílet se tak na měření jevu CP narušení na experimentu Belle. Toto měření mohlo být realizováno na v současné době největším vzorku $B\bar{B}$ dat na světě.

Obzvláště jsem velice vděčný prof. Christianu Kieslingovi za to, že mě vřele přijal za svého člena pracovního týmu v Max-Planck Institutu v Mnichově. Zároveň bych mu chtěl poděkovat za jeho profesionální přístup a mnoho cenných rad, které mi v souvislosti s touto prací předal, a to od technické problematiky vrcholového detektoru DEPFET až po zodpovězení různých otázek týkajících se fyziky elementárních částic. Dále bych chtěl výrazně poděkovat Dr. Jeremymu Dalsenovi, bez jehož pomoci a zkušeností bych byl stěží schopen technicky zvládnout celou Belle analýzu. A nejen on mi v tom výrazně pomohl. Rád bych zároveň poděkoval i dalším členům MPI kolektivu, zvláště pak Koljovi Prothmannovi, Andreasu Mollovi, Martinu Ritterovi a Veronice Čobanové. Nikdy nekončící diskuze a velice přátelská atmosféra mi navždy zůstanou v hlavě. Z MPI ještě nemohu opomenout a chtěl bych mu zvláště poděkovat, Dr. Alexejovi Raspiarezovi. Jsem mu extrémně vděčný, že se se mnou podělil o své cenné vědecké zkušenosti, které byly následně úspěšně aplikovány při rozvoji Belle II softwaru. Navíc jsem získal tu možnost se od něho v průběhu několika zajímavých diskuzí hodně naučit v oblasti HEP simulací.

Mimo to bych velice rád vyjádřil své poděkování všem vědeckým pracovníkům z KEKu, obzvláště pak Dr. Karimu Trabelsovi, prof. Yoshihide Sakaiovi a prof. Takanori Harovi. Dr. Karim Trabelsi, ačkoliv velice zaneprázdněný jako fyzikální koordinátor celého experimentu Belle, mi byl vždy velice nápomocen při fyzikální analýze, byl ochoten diskutovat složité problémy i problémy triviálního rázu a vždy mi poskytl cenné rady k jejich vyřešení. Díky úsilí prof. Yoshihida Sakaie, prof. Takanori Hary, prof. Christiana Kieslinga a vědeckému programu japonské vlády JSPS mi byla nabídnuta jedinečná příležitost strávit více jak čtyři měsíce v japonské laboratoři KEK a mít tak možnost se přímo v Japonsku aktivně účastnit upgradu experimentu Belle II.

Nakonec bych chtěl vyjádřit své poděkování Dr. Zdeňkovi Doležalovi, svému školiteli, za jeho naprosto profesionální přístup, spoustu cenných rad, které mi v průběhu celého PhD studia předal, a za nepolevující podporu. A nejen za to, životně důležitou součástí celé práce byla i výrazná finační podpora, bez níž by práce na japonském experimentu byla jen stěží představitelná. Současně bych chtěl poděkovat všem svým spolupracovníkům z Ústavu

částicové a jaderné fyziky v Praze, za jejich celkově přátelskou pracovní atmosféru a bezvadnou podporu. Zvláště pak Dr. Petru Kvasničkovi za četné a velice inspirativní diskuze ohledně nejen statistiky, Dr. Pavlu Řezníčkovi za živé diskuze týkající se B fyziky a spoustu námětů, které mě přivedly ke zdárnému řešení. Mimo to bych chtěl poděkovat dalším členům našeho kolektivu za spoustu podnětných komentářů, a to Dr. Petru Kodyšovi a Jánu Scheirichovi.

A samozřejmě nesmím opomenout obrovskou a nikdy nekončící podporu vlastní rodiny. Moc jim za to děkuji.

Prohlašuji, že jsem tuto disertační práci vypracoval samostatně a výhradně s použitím citovaných pramenů, literatury a dalších odborných zdrojů.

Beru na vědomí, že se na moji práci vztahují práva a povinnosti vyplývající ze zákona č. 121/2000 Sb., autorského zákona v platném znění, zejména skutečnost, že Univerzita Karlova v Praze má právo na uzavření licenční smlouvy o užití této práce jako školního díla podle 60 odst. 1 autorského zákona.

V Praze dne 13. prosince 2013

On the occasion, I would like to express my deepest gratitude to all the people who have actively involved me in the upgrade of the Belle II vertex detector and simultaneously, have given me a unique chance to touch the world's largest $B\bar{B}$ data sample acquired by Belle experiment and let me work together with other scientists from around the world in one of the leading scientific organizations, KEK (Japan), on the measurement of CP violation.

Particularly, I'm more than grateful to prof. Christian Kiesling for accepting me warmly as a member of his team at Max-Planck Institut in Munich, for his professional approach and a lot of valuable advice in many possible aspects, from technical questions regarding DEPFET vertex detector to various elementary particle physics related questions concerning my analysis. Further, I owe my great thanks to Dr. Jeremy Dalseno, without his help and experience I'd be barely able to technically handle the whole Belle analysis chain. Moreover, I have learnt a lot from him during many interesting discussions. Besides, I'd also like to thank other members of the MPI team, especially to Kolja Prothmann, Andreas Moll, Martin Ritter and Veronika Chobanova. The never ending vivid discussions and more than friendly atmosphere will remain memorable. From the MPI team I can't forget to thank, in special, Dr. Aliaksei Raspiareza. I'm extremely grateful for sharing his research experience which has been successfully applied in the development of Belle II software framework. Moreover, I have learnt a lot from him during several helpful discussions covering all possible aspects of MC simulations in HEP.

Besides the MPI team, I'd like to express my deepest thanks and appreciation to all KEK people, especially to Dr. Karim Trabelsi, prof. Takanori Hara and prof. Yoshihide Sakai. Dr. Karim Trabelsi, though very busy as a physics coordinator of the Belle experiment, has always been willing to help me with the analysis, to discuss possible issues, either trivial or complex, and to provide valuable hints to solve all appeared problems. Moreover, he exactly knew how to push me forward and get over the difficulties. Thanks to prof. Yoshihide Sakai and prof. Takanori Hara I've got a unique chance to spend more than four months in KEK laboratory within a JSPS scientific program and to actively work at the upgrade of the Belle II vertex detector.

Finally, I'm very grateful to my supervisor Dr. Zdeněk Doležal for his completely professional approach, valuable advice and continuous support and encouragement. And not only that, the vital part has also become the financial support without which my work on a Japanese experiment would be hardly possible. Simultaneously, I owe my thanks to all people at the Institute of Particle and Nuclear Physics in Prague, for their friendly atmosphere and a great support. Especially, I'd like to thank Dr. Peter Kvasnička for many inspiring discussions regarding not only statistics, Dr. Pavel Řezníček

for vivid discussions regarding B physics and lots of hints he has offered to solve my analysis problems. Besides, I'd like to thank other members of our team, Dr. Peter Kodyš and Ján Scheirich, for many productive comments they've had during my work.

Last but not least, I'd like to express my thanks to my family for great support and endless patience.

I declare that I carried out this doctoral thesis independently, and only with the cited sources, literature and other professional sources.

I understand that my work relates to the rights and obligations under the Act No. 121/2000 Coll., the Copyright Act, as amended, in particular the fact that the Charles University in Prague has the right to conclude a license agreement on the use of this work as a school work pursuant to Section 60 paragraph 1 of the Copyright Act.

Prague, December 13, 2013

Název práce: *Měření CP narušení na experimentu Belle v rozpadech $B^0 \to \eta_c K^0_S$ metodou tzv. časové analýzy, optimalizace vrcholového detektoru pro experiment Belle II.*
Autor: *Zbyněk Drásal*
Katedra: *Ústav částicové a jaderné fyziky*
Vedoucí disertační práce: *Doc. RNDr. Zdeněk Doležal, Dr., ÚČJF*
E-mail vedoucího: *Zdenek.Dolezal@mff.cuni.cz*

Abstrakt: Disertační práce se zabývá dvěma nezávislými tématy. V první části jsou prezentována měření větvících poměrů a parametrů CP narušení v rozpadech $B^0(B^\pm) \to \eta_c K^0_S(K^\pm)$, $\eta_c \to p\bar{p}$. Konkrétně jde o měření úhlu $\sin 2\phi_1$: $\mathcal{S}_{CP} = 0.68^{+0.38}_{-0.46} \pm 0.13_{\text{syst}}$, a parametru tzv. přímého CP narušení: $\mathcal{A}_{CP} = 0.00^{+0.23}_{-0.31} \pm 0.08_{\text{syst}}$. Těchto výsledků bylo dosaženo na výsledném vzorku dat, 772×10^6 $B\bar{B}$ párů, nabraných japonským experimentem Belle na e^+e^- asymetrickém urychlovači KEKB, naladěném na produkci rezonance $\Upsilon(4S)$. V druhé části je popsán náš přístup k MC simulacím odezvy vrcholového detektoru Belle II (upgrade experimentu Belle) na vysokoenergetické částice. Vrcholovým detektorem označujeme 2 vrstvy pixelových senzorů DEPFET (PXD) a 4 vrstvy křemíkových oboustranných stripových detektorů (SVD). MC simulace, včetně rekonstrukce částic, byly implementovány do modulárního softwarového prostředí ILC projektu, a to za účelem optimalizace vrcholového detektoru Belle II. Z dosažených výsledků zde prezentujeme detailní studii očekávaného rozložení materiálu v tomto detektoru, optimalizaci konečného designu pixelového detektoru a studium jeho pracovní odezvy v očekávaném vysokém QED pozadí a dále studii instalace tzv. dopředných SVD senzorů ve vrcholovém detektoru a její vliv na rozlišení a množství detekovaných hitů. Na závěr uvádíme studii očekávaného rozlišení vrcholového detektoru v tzv. impakt parametru.

Klíčová slova: *Belle, CP narušení, $\sin 2\phi_1$, $c\bar{c}$ rezonance, Belle II, vrcholový detektor, pixelový detektor, DEPFET, stripový detektor, SVD, MC simulace, ILC, digitizace, clustering, pattern recognition, tracking, rozlišení, impakt parametr*

Title: *Measurement of Time-Dependent CP Violation in $B^0 \to \eta_c K^0_S$ at Belle Experiment, Optimisation Studies of the Belle II Vertex Detector*
Author: *Zbyněk Drásal*
Department: *Institute of Particle and Nuclear Physics*
Supervisor: *Dr. Zdeněk Doležal, IPNP*
Supervisor's e-mail address: *Zdenek.Dolezal@mff.cuni.cz*

Abstract: This doctoral thesis deals with two independent topics. In the first part we present a measurement of branching ratio(s) and time-dependent CP violation parameters in $B^0(B^\pm) \to \eta_c K^0_S(K^\pm)$, $\eta_c \to p\bar{p}$. The values of CP violation parameters have been found as follows; $\sin 2\phi_1$, denoted as an $\mathcal{S}_{CP}$ parameter, equals: $\mathcal{S}_{CP} = 0.68^{+0.38}_{-0.46} \pm 0.13_{\,\mathrm{syst}}$, the direct CP violation parameter, denoted as an $\mathcal{A}_{CP}$, is: $\mathcal{A}_{CP} = 0.00^{+0.23}_{-0.31} \pm 0.08_{\,\mathrm{syst}}$. These results have been obtained with the final data sample of 772×10^6 $B\bar{B}$ pairs collected at $\Upsilon(4S)$ resonance with a Belle detector at the KEKB e^+e^- asymmetric collider machine in Japan. In the second part, we present our approach to the MC simulation of Belle II vertex detector and its response to high energy particles. Belle II represents an upgrade of current Belle experiment and its designed vertex detector will consist of 2 layers of DEPFET pixel detectors (PXD) and 4 layers of double-sided silicon micro-strip detecters (SVD). The MC simulation together with a charged particle reconstruction have been developed and implemented within a modular based ILC software framework in order to find an optimal design of the Belle II vertex detector. From final optimisation studies, we present a detailed study of expected material distributions in the vertex detector, optimisation of the final pixel detector layout and its performance in expected harsh QED based background, influence study of slanted SVD detectors installation in forward region and its impact on resolution and hit occupancy, and finally, a study of expected impact parameter resolution of the whole vertex detector.

Keywords: *Belle, CP violation, $\sin 2\phi_1$, $c\bar{c}$ resonance, Belle II, vertex detector, pixel detector, DEPFET, micro-strip detector, SVD, MC simulation, ILC software, digitization, clustering, pattern recognition, tracking, resolution, impact parameter*

Preface

In 2009, having worked actively on the development of Depfet-based vertex pixel detector for a future International Linear Collider (ILC), the Depfet collaboration [1], together with our Prague experimental group, made a strategic step forward and joined a new emerging Belle II project [2] in Japan. The main aim of such a decision was to apply the Depfet technology in a real running experimental environment. With the decision in mind, the Depfet collaboration made a commitment to build a new vertex pixel detector (based on Depfet technology) for the Belle II detection system. The Belle II experiment is an upgrade of Belle [3], a successful B-factory experiment having been operated in Japan in 1999 – 2010. This project represents currently the only "Super" B-factory experiment in the world; with a plan to collect 50 times more data compared to Belle and thus, to allow investigation of various extensions to the Standard model through precision measurements in the B, charm and τ sectors. Its first data taking is planned to start early in 2016 [4, 5].

Simultaneously with our efforts within the Belle II collaboration, the Prague experimental group was offered an interesting opportunity to actively participate in the Belle ICPV physics group, focused on Indirect CP Violation. For precise measurements of such effects a time-dependent technique is commonly used and the analysis precision is then closely related to the determination of B vertices, so-called B vertexing. As intuitively clear, vertexing precision goes hand in hand with a deep understanding of detection mechanisms, electronics effects and consequently, in understanding of arising systematic effects in used vertex detectors. So with our participation in the Depfet hardware development, it's natural, we've got another unique chance to touch the world's largest data sample with its strong impact on understanding of CP violation effects. The data were collected over more than a decade at KEKB collider by Belle and even now, this data sample provides physicists with a unique tool for investigation of various fascinating CP violation phenomena within the B sector and related heavy flavour physics.

As clear from the historical prospective, the whole PhD work has been mainly connected with the development of various types of vertex detectors,

their application in particle physics and with the physics analysis, the precision of which would not be possible with absence of such devices. The detectors in focus have not just been Depfet pixel detectors, as mentioned above, but also micro-strip silicon vertex detectors. In summary, three individual topics have been covered:

The first task was to develop a full MC simulation (digitization) with the aim to simulate in detail the response of Depfet pixel and silicon micro-strip vertex detectors. All the software was written within the framework intended for ILC simulation studies and further, its correctness was verified (for pixel detectors by B. Schwenker [6]) using various test beam data.

After the Prague group joined the Belle II collaboration, the digitization software was extended within the ILC framework with a full simulation chain, including Geant4 simulation of a new Belle II vertex detector, simplified pattern recognition, track fitting procedure (taken over from the ILC software) and a standalone analysis. The main focus of the second task was to provide a Belle II vertex group with an efficient tool for the optimization of various pixel/strip detector parameters (both technological and physics related) and thus, to improve the future physics performance of the Belle II vertex detector. This software was developed in a close collaboration with K. Prothmann [7] during several stays of the author at the Max-Planck Institute in Munich.

Finally, the third task represents the main topic of this doctoral thesis and is dedicated to the time-dependent CP violation measurement in $B^0(B^\pm) \to \eta_c K^0_S(K^\pm)$.

Considering all the pros and cons, the author of this thesis has decided to focus mainly on the most actual topic, the physics analysis of CP violation measurement at Belle, and to include the older topics just in a form of published proceedings (exclusively written by the author of the thesis), only with a brief introduction and summary of the most important results. The physics analysis on CP violation is in detail described in the first part, the Belle II vertex detector related analyses in the second part. The reasons are mainly clarity and simplicity; to consistently describe only one topic in detail. Moreover, the first two topics have been already shown at several Belle II general meetings, some results are included in the Belle II TDR [5] and most importantly, the detailed description of both analyses have been published in terms of PoS (Proceedings of Science) at two international conferences: Vertex (2011) [8] and HQL - Heavy Quarks and Leptons (2012) [9]. That's the main reason, why the author believes that results of the first two topics are already well established and known to the whole Belle II collaboration and don't have to be covered in detail here.

Contents

Part I

Belle Physics Analysis

1 Introduction

In the Standard model (SM) of elementary particle physics, the CP violation occurs due to a single irreducible complex phase in the Cabbibo-Kobayashi-Maskawa (CKM) quark-mixing matrix [10, 11]. Recently, mixing-induced CP violation has been clearly observed by the BaBar [12] and Belle [13] Collaborations in all statistically significant $b \to c\bar{c}s$ induced decays, such as e.g. $B \to J/\psi K^0_{\rm S}$ (CP-odd eigenstate) or $B \to J/\psi K^0_{\rm L}$ (CP-even eigenstate). These decays that proceed dominantly through the colour suppressed $b \to c\bar{c}s$ transition are sensitive to angle ϕ_1, one of the angles of the Kobayashi-Maskawa (KM) unitarity triangle, defined as $\phi_1 \equiv arg[-V_{\rm cd}V^*_{\rm cb}/V_{\rm td}V^*_{\rm tb}]$[a]. Relevant Feynman diagrams contributing to these transitions are shown in Figure 1.1. The left diagram, colour suppressed tree graph, represents a dominant contribution. The right one, a strong (electroweak) penguin graph represents a minor contribution (in case of electroweak interaction, the gluons are replaced by Z or γ). Considering a Wolfenstein parametrization of the CKM matrix [14], it can be shown that the penguin diagram with heavy quarks in the loop (c, t) has the same weak phase as the tree graph. The one with u quark has a different weak phase and thus, introduces some theoretical uncertainty on $\sin 2\phi_1$ measurement. Fortunately, the uncertainty is estimated to be less than 1% [15] and therefore, a real ϕ_1 angle, not only its effective value, can be measured.

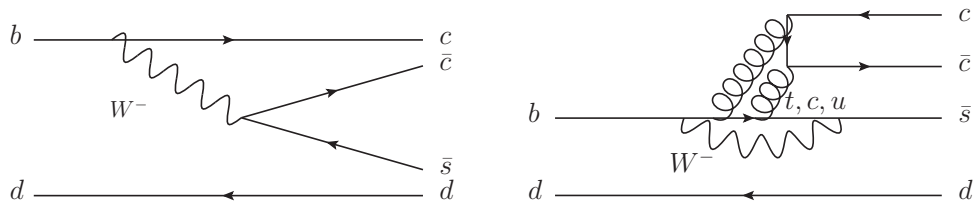

Fig. 1.1: Tree and penguin diagrams for $b \to c\bar{c}s$ induced decays, such as $B \to J/\psi K^0_{\rm S}$ (with 3-gluon exchange in the penguin graph) or $B \to \eta_{\rm c} K^0_{\rm S}$.

The physics analysis, presented in this part of the thesis, is concerned

[a] Another naming convention for ϕ_1 angle, β, is also used.

with the measurement of branching ratio and time-dependent CP violation parameters in $B \to \eta_c K^0_S$. In general, the physics lying behind such decay is very similar to that of $B \to J/\psi K^0_S$, which is due to its experimentally clean pattern often recognized as a "golden" channel to measure the CP violation at B-factories. Similarly as the $J/\psi K^0_S$, the $\eta_c K^0_S$ represents a CP-odd eigenstate and the B decay with this final state has a comparable branching fraction to that of $B \to J/\psi K^0_S$. Therefore, it provides another promising physics mode for further study of time-dependent CP violation in the system of neutral B mesons. On the other hand, unlike the J/ψ charmonium state ($J^{PC} = 1^{--}$), the η_c represents a scalar particle ($J^{PC} = 0^{-+}$) and thus, can only decay purely hadronically. For comparison, the basic properties of all charmonia are summarized in Table 1.1.

$c\bar{c}$ **meson**	J^{PC}	**Mass** [MeV]	**Width** [MeV]
$\eta_c(1S)$	0^{-+}	2980.3 ± 1.2	28.6 ± 2.2
$J/\psi(1S)$	1^{--}	3096.916 ± 0.011	0.0929 ± 0.0028
$\chi_{c0}(1P)$	0^{++}	3414.75 ± 0.31	10.5 ± 0.8
$\chi_{c1}(1P)$	1^{++}	3510.66 ± 0.07	0.88 ± 0.05
$h_c(1P)$	1^{+-}	3525.42 ± 0.29	< 1
$\chi_{c2}(1P)$	2^{++}	3556.20 ± 0.09	1.95 ± 0.13
$\eta_c(2S)$	0^{-+}	3637 ± 4	17 ± 7
$\psi(2S)$	1^{--}	3683.093 ± 0.034	0.286 ± 0.016

Tab. 1.1: The basic properties of $c\bar{c}$ mesons [16].

In the B-factories, B mesons are produced from the bottomonium resonance, $\Upsilon(4S)$, which represents the lowest possible $b\bar{b}$ bound state that decays into B mesons. The $\Upsilon(4S)$ decays to a $B\bar{B}$ pair of which one (B^0_{rec}) may be reconstructed as a $B^0 \to \eta_c K^0_S$ while the other ($\bar{B}^0{}_{tag}$) may reveal its flavour. The proper time interval between B^0_{rec} and $\bar{B}^0{}_{tag}$ which decay at time, t_{rec} and t_{tag}, respectively, is defined as $\Delta t \equiv t_{rec} - t_{tag}$. For coherent $B\bar{B}$ production in the $\Upsilon(4S)$ decay, the time-dependent decay rate $\mathcal{P}(\Delta t, q)$ when B^0_{tag} posseses flavour, q (B^0: $q = +1$, $\bar{B}^0$: $q = -1$), can be expressed by:

$$\mathcal{P}(\Delta t, q) = \frac{e^{-|\Delta t|/\tau_{B^0}}}{4\tau_{B^0}} \Big\{ (1 - q.\Delta w) + q(1-2w) \times \Big[\mathcal{S}_{CP} \sin(\Delta m_d \Delta t) + \mathcal{A}_{CP} \cos(\Delta m_d \Delta t) \Big] \Big\} \tag{1.1}$$

where

$$\mathcal{S}_{CP} = +\frac{2\,\mathcal{I}m\,\lambda_{CP}}{1+|\lambda_{CP}|^2},$$
$$\mathcal{A}_{CP} = -\frac{1-|\lambda_{CP}|^2}{1+|\lambda_{CP}|^2},$$

$\tau_{\mathrm{B^0}}$ is the B^0 lifetime, Δm_{d} is the difference between the B meson mass eigenstates determined from the $B^0 - \bar{B}^0$ oscillations, $\lambda_{CP} = (\tilde{q}/p)(\bar{A}_{\mathrm{f}}/A_{\mathrm{f}})$, $\tilde{q}$ and p are complex numbers that relate the B meson flavour eigenstates to their mass eigenstates and A_{f} ($\bar{A}_{\mathrm{f}}$) is the amplitude of the $B^0 \to f$ ($\bar{B}^0 \to f$) decay [16]. The last two parameters, average wrong-tag probability w and the mistag difference Δw, describe the effect of incorrect tagging and the difference between the wrong-tag probabilities for B^0 and $\bar{B}^0$ mesons, respectively. Moreover, the relation assumes that the total decay rate difference between the two mass eigenstates, $\Delta\Gamma_{\mathrm{d}}$, is negligible, and for simplicity, no effects of natural Belle detector resolution have been assumed in that relation.

In the Eq. (1.1) a non-zero cosine term, expressed as a parameter $\mathcal{A}_{\mathcal{CP}}$, measures the interference between decay amplitudes with different weak and strong phases (direct CP violation $|\bar{A}_{\mathrm{f}}/A_{\mathrm{f}}| \neq 1$) or $B_0 - \bar{B}_0$ mixing induced CP violation ($|\tilde{q}/p| \neq 1$). The sine term, S_{CP}, measures the interference between the direct decay and decay after $B^0 - \bar{B}^0$ oscillations. As mentioned above, with a very small theoretical uncertainty, the SM predicts $\lambda_{CP} = \xi e^{-2i\phi_1}$, $\mathcal{S}_{\mathcal{CP}} = -\xi \sin 2\phi_1$ and $\mathcal{A}_{\mathcal{CP}} \sim 0$ for the $b \to c\bar{c}s$ transitions, where $\xi = -1(+1)$ for CP-odd (CP-even) final states.

	$N(B\bar{B}$-pairs)	$\mathcal{S}_{\mathcal{CP}}$	$\mathcal{A}_{\mathcal{CP}}$
Belle	151×10^6	$1.26^{+0.27}_{-0.39} \pm 0.06_{\mathrm{syst}}$	–
BaBar	465×10^6	$0.925^{+0.160}_{-0.160} \pm 0.057_{\mathrm{syst}}$	$0.080^{+0.124}_{-0.124} \pm 0.029_{\mathrm{syst}}$

Tab. 1.2: The previous measurements of CP parameters in $B \to \eta_{\mathrm{c}} K^0_{\mathrm{S}}$.

The Belle and BaBar experiments have already performed measurements of CP parameters in the studied $B \to \eta_{\mathrm{c}} K^0_{\mathrm{S}}$. For comparison, their results are summarized in Table 1.2. This analysis is an update to the previous Belle analysis with $85 \times 10^6 B\bar{B}$ pairs [17] and includes the complete data set of Belle experiment which consists of $772 \times 10^6 B\bar{B}$ pairs. The BaBar results have been obtained using $465 \times 10^6 B\bar{B}$ pairs and represent the first observation of CP violation in this mode [12]. The current value of $\sin 2\phi_1$ world

average is $\mathcal{S}_{CP} = 0.679 \pm 0.020$ $(0.018_{\text{stat-only}})$[18], and includes measurements in following B decay modes: $J/\psi K^0_S$, $J/\psi K^0_L$, $\psi(2S)K^0_S$, $\chi_{c1}K^0_S$, $\eta_c K^0_S$, $J/\psi K^{*0}(K^{*0} \to K^0_S\pi^0)$, $J/\psi K^0_S$ ($J/\psi \to$ hadrons) and $\chi_{c0}K^0_S$. See Table 1.3.

Mode (ξ)	**BaBar**	**Belle**
$J/\psi K^0_S$ (-1)	$0.657 \pm 0.036 \pm 0.012$	$0.670 \pm 0.029 \pm 0.013$
$J/\psi K^0_L$ (+1)	$0.694 \pm 0.061 \pm 0.031$	$0.642 \pm 0.047 \pm 0.021$
$\psi(2S)K^0_S$ (-1)	$0.897 \pm 0.100 \pm 0.036$	$0.738 \pm 0.079 \pm 0.036$
$\chi_{c1}K^0_S$ (-1)	$0.614 \pm 0.160 \pm 0.040$	$0.640 \pm 0.117 \pm 0.040$
$\eta_c K^0_S$ (-1)	$0.925 \pm 0.160 \pm 0.057$	–
$J/\psi K^{*0}$ $(1-2\|A_\perp\|^2)$	$0.601 \pm 0.239 \pm 0.087$	–
$\chi_{c0}K^0_S$ (+1)	$0.69 \pm 0.52 \pm 0.04(0.07)$	–
$J/\psi K^0_S$, hadronic (+1)	$1.56 \pm 0.42 \pm 0.21$	–
All charmonium	0.679 ± 0.020 $(0.018_{\text{stat-only}})$	

Tab. 1.3: The previous measurements of $\sin 2\phi_1$ at BaBar[12, 19, 20] and Belle experiments [13], $\xi = -1(+1)$ represents CP-odd (CP-even) final states.

In the first Chapter of this part of the thesis the focus is given on a brief overview of CP violation within the Standard model and a historical background of how such a unique effect has been explored. A detailed description of Belle experimental apparatus and an asymmetric e^+e^- collider, KEKB, which both were built to acquire the unique $B\bar{B}$ data sample, is given in Chapter 2. Chapter **??** is devoted to a theoretical overview. All applied selection criteria together with used observed variables and procedures suppressing various sources of particle background are described in event reconstruction Chapter, Chapter 3. In Chapter 4, we build a data model and explain a fitting procedure. Chapter 5 verifies the consistency of the model and validates the whole analysis procedure. Fitting results are presented in Chapter 6 and Chapter 7. A control sample measurement used to calibrate a final CP violation measurement is presented in Chapter 6, the final measurement in Chapter 7. There are several appendices added. Appendix A is dedicated to the description of flavour tagging procedure at Belle experiment, Appendix B details description of time resolution function. This function describes the detector response. In Appendix C we summarize for clarity all fit parameters. Final conclusions and outlook are summarized in the last chapter of the first part of the thesis, called conclusions and outlook.

2 Experimental Apparatus

The branching ratio and time-dependent measurement of CP violation parameters in $B \to \eta_c K^0_S$ ($B^\pm \to \eta_c K^\pm$) is based on the final data sample containing $772 \times 10^6 B\bar{B}$ pairs collected with the Belle detector [21] at the KEKB asymmetric-energy e^+e^- (3.5 on 8.0 GeV) collider machine [22]. The Belle experiment and the KEKB accelerator are located at the High Energy Accelerator Research Organization (KEK) in Tsukuba, Japan, and represent one of the leading scientific projects in quantitative studies of rare B-meson decays and CP violation in the b-sector in the world. Operating with a peak luminosity that has exceeded $2.1 \times 10^{34}\,\mathrm{cm}^{-2}\mathrm{s}^{-1}$, the KEKB collider produces the $\Upsilon(4S)$ resonance ($E_{\mathrm{CMS}} = 10.58\,\mathrm{GeV}$) with a Lorentz boost of $\beta\gamma \approx 0.425$ nearly along the z-axis, opposite to the positron beam direction. The $\Upsilon(4S)$ resonance is a $b\bar{b}$ triplet state with orbital momentum equal to 1. Its mass lies only 20 MeV above the threshold for $B\bar{B}$ production, and therefore, the $\Upsilon(4S)$ mostly decays into $B^0\bar{B}^0$ or B^+B^- pairs; non-$B\bar{B}$ decays are less than 4 % at 95 % confidence level [23]. In order to perform high preci-

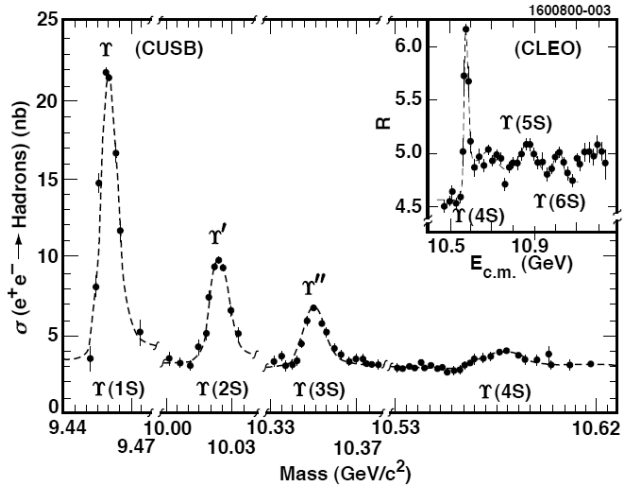

Fig. 2.1: CUSB data illustrating the $\Upsilon(1S)$, $\Upsilon(2S)$, $\Upsilon(3S)$, and $\Upsilon(4S)$ states with an insert of CLEO data illustrating the $\Upsilon(5S)$ and $\Upsilon(6S)$ states [24].

sion CP violation measurements a high event statistics is a must. This has been successfully achieved with a high luminosity delivered by the collider system. Moreover, the KEKB currently holds the world record in the peak luminosity, $2.1 \times 10^{34}\,\mathrm{cm}^{-2}\mathrm{s}^{-1}$.

2.1 The KEKB Accelerator

The KEKB accelerator system consists of several components: a particle source, several pre-accelerators, a linear accelerator (LINAC) and two main storage rings; one for electrons (High Energy Ring - HER) and one for positrons (Low Energy Ring - LER). Electrons and positrons are accelerated to their respective energies, 8 GeV and 3.5 GeV, in the LINAC system, and injected to HER and LER. The length of both rings is about 3 km and roughly 5000 particle bunches circulate in each ring with a bunch spacing of 59 cm. In KEKB the designed beam currents are 1.1 A and 2.6 A for HER and LER, respectively, and the beam size at the interaction point is 90 μm in the horizontal and 1.9 mm in the vertical direction. A schematic picture of the accelerator system is shown in Fig. 2.2.

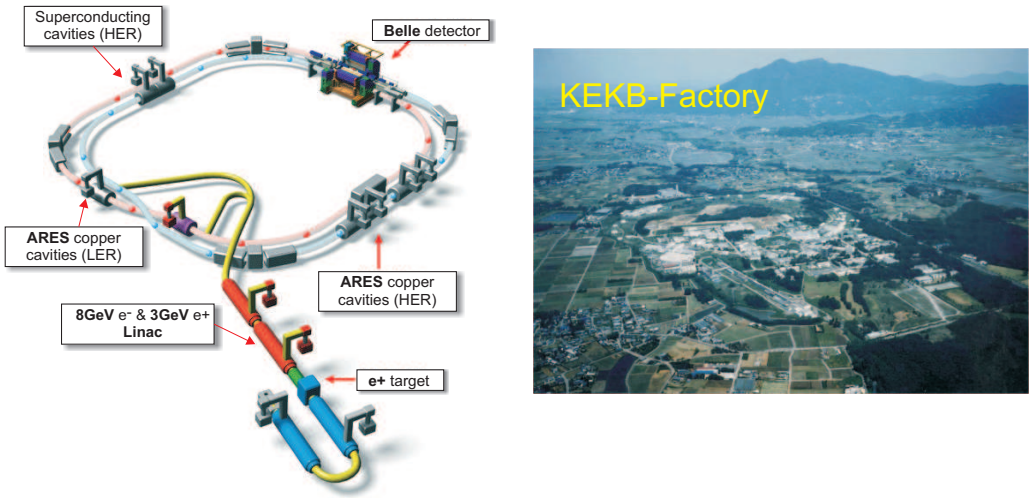

Fig. 2.2: The KEKB accelerator machine and its location within KEK in Tsukuba (Japan).

Colliding particles are brought to the interaction region at a crossing angle of ±11 mrad. The main reason for such a configuration is to efficiently separate incoming and outgoing beams, and avoid parasitic collisions. To compensate for possible drop in luminosity due to the finite crossing angle,

crab cavities were installed; they tilt the particle bunches before their collision in a way, that the luminosity of a head-on collision is restored back.

2.2 The Belle Detector

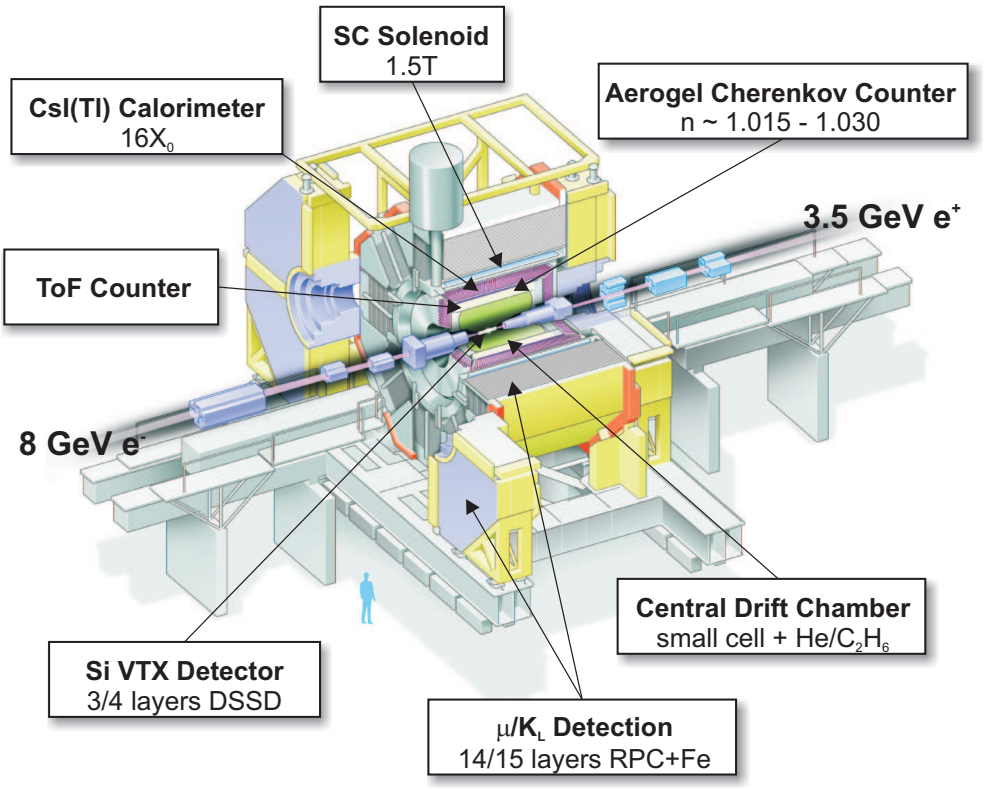

Fig. 2.3: The Belle detection system with all sub-detector components.

The Belle detector is a large-solid-angle magnetic spectrometer that consists of a silicon vertex detector (SVD), a 50-layer central drift chamber (CDC), an array of aerogel threshold Cherenkov counters (ACC), a barrel-like arranged time-of-flight scintillation counters (TOF), and an electromagnetic calorimeter (ECL) comprised of CsI (Tl) crystals located inside a superconducting solenoid coil that provides a 1.5 T magnetic field. An iron flux-return located outside of the coil is instrumented to detect K_L^0 mesons and to identify muons (KLM). The detector covers the θ region extending from 17° to 150°. Two inner detector configurations were used. A 2.0 cm beam pipe and a 3-layer silicon vertex detector (SVD1) were used for the first data sample of $152 \times 10^6 B\bar{B}$ pairs, while a 1.5 cm beam pipe, a 4-layer silicon detector

(SVD2) and a small-cell inner drift chamber were used to record the remaining $620 \times 10^6 B\bar{B}$ pairs. We use a GEANT3-based [25] Monte Carlo (MC) simulation to model the response of Belle detector and to determine its detection efficiency in the studied physics modes.

2.2.1 Belle Data Set

The list of all data subsets acquired with Belle detector and available for data analysis is shown in Tab. 2.1. The numbers of $B\bar{B}$ pairs corresponding to each subset (so-called experiment) and used further in branching ratio calculations are listed in the same Table.

2.2.2 Beam Pipe (BP)

The precise determination of B decay vertices represents a key factor in the time-dependent CP violation measurement at Belle experiment. Basically, a multiple scattering in the BP and the first layer of silicon vertex detector (SVD), together with the distance of the first SVD layer to the interaction point, are the main limiting factors in precise determination of z-vertex position. In addition, the vertex resolution worsens (roughly inversely) with increasing distance of the first SVD layer with respect to the interaction point [21]. Having taken into account these two constraints during the design phase, it was of high necessity to minimize material in both the beam pipe and SVD, and simultaneously position the first SVD layer as close as possible to the interaction point.

The beam pipe was designed as a double-wall beryllium cylinder with an inner radius of 2 cm, and with an active cooling provided by helium gas flowing between the walls. The beryllium and helium gas were intentionally chosen due to their low atomic numbers and relatively low impact on deflection of particle tracks. In addition, to reduce the low energy X-ray background (synchrotron gammas with energy < 5 keV), the BP was coated with 20 µm thick golden layer. During the upgrade of SVD detector in 2003 (SVD1 $\rightarrow$ SVD2) the beam pipe was redesigned and its inner radius was decreased to 15 mm. The main motivation for such a step was to get the first SVD layer closer to the interaction point.

2.2.3 Silicon Vertex Detector (SVD)

The silicon vertex detector [26], an innermost part of the Belle tracking system, played a crucial role in the measurement of B^0, $\bar{B}^0$ z-vertex position and their respective difference. The difference in z, denoted further as Δz,

Experiment number	$N(B\bar{B}\text{-pairs})$ $[\times 10^6]$
7	$6.4587 + 0.1615 - 0.0976$
9	$4.7597 + 0.0286 - 0.0473$
11	$8.8509 + 0.0517 - 0.0518$
13	$11.6998 + 0.2393 - 0.2392$
15	$13.5679 + 0.0963 - 0.1055$
17	$12.4588 + 0.3301 - 0.3301$
19	$27.1705 + 0.1676 - 0.1676$
21	$4.3371 + 0.0540 - 0.0676$
23	$6.4755 + 0.0675 - 0.0989$
25	$28.0008 + 0.3329 - 0.1605$
27	$28.1814 + 0.2110 - 0.1516$
SVD1	$\mathbf{151.961 \pm 1.241}$
31	$19.6587 + 0.3045 - 0.3031$
33	$19.3022 + 0.3000 - 0.2987$
35	$18.5262 + 0.2861 - 0.2855$
37	$67.1819 + 1.0326 - 1.0319$
39	$47.0818 + 0.7265 - 0.7246$
41	$64.0134 + 0.9863 - 0.9857$
43	$61.5614 + 0.9493 - 0.9474$
45	$14.3538 + 0.2218 - 0.2215$
47	$41.2186 + 0.6406 - 0.6393$
49	$29.7271 + 0.4648 - 0.4634$
51	$41.8919 + 0.6605 - 0.6590$
55	$80.2472 + 1.2462 - 1.2439$
61	$37.4460 + 0.5624 - 0.5617$
63	$35.6231 + 0.5297 - 0.5291$
65	$41.7867 + 0.6317 - 0.6309$
SVD1 & SVD2	$\mathbf{771.581 \pm 10.566}$

Tab. 2.1: The list of Belle data subsets [27].

and derived quantity Δt, $\Delta t = \Delta z/\beta\gamma$, represent the key observables for the measurement of time dependent CP asymmetries and CP violation effects. At Belle experiment $\sim 100\,\mu\text{m}$ Δz resolution has been achieved. Such a value is precise enough for the time-dependent measurements, since the decay length of B mesons reaches roughly $200\,\mu\text{m}$ in the laboratory system due to relatively high e^+e^- boost.

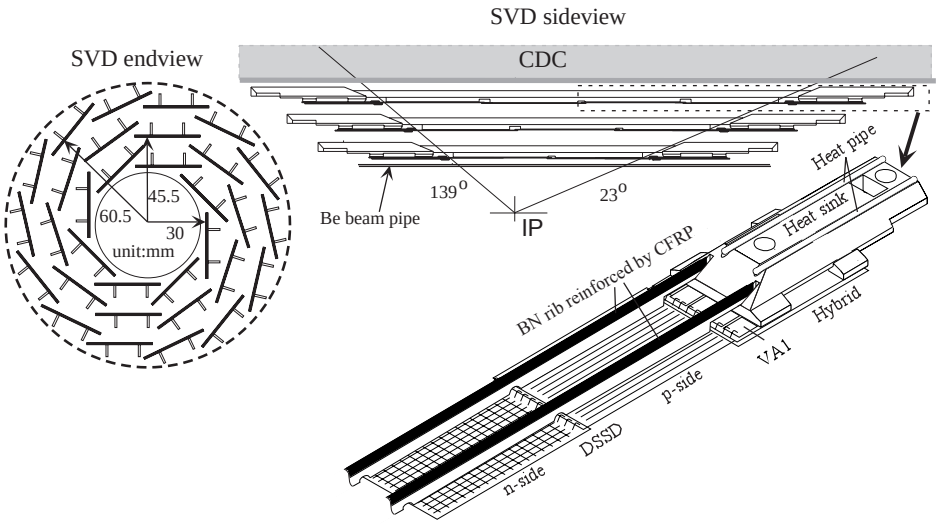

Fig. 2.4: Geometry configuration of Silicon Vertex Detector (SVD1) [21]. The upper left picture illustrates SVD geometry. SVD acceptance and a mechanical setup of SVD ladder are shown at the upper and lower right picture, respectively.

The first version of SVD, illustrated in Figure 2.4 and denoted as SVD1, consisted of three concentric layers positioned at 30, 45.5 and 60.5 mm, and covered the polar angle from 23° to 139°. The geometry layout was designed in a so-called wind-mill structure, with each layer made-up of several ladders, and each layer consisted of a few double sided silicon strip detectors (DSSD), $300\,\mu\text{m}$ thick. The number of DSSD strips was 1280 on both sides (r-ϕ and z). In order to reduce the high number of necessary read-out channels, the scheme with floating strips was applied, and only 640 pads were in reality read out. The DSSD read-out electronics was based on the VA1 integrated circuit.

In 2003, SVD1 was replaced with its second version, denoted as SVD2. The new version of silicon vertex detector came with several improvements, among which the following are the most important for the overall vertexing performance. First, four layers, instead of three, were installed, and the first layer was positioned much closer to the interaction point; the radii were 20,

43.5, 70 and 88 mm. Second, the acceptance region significantly improved. The new SVD2 coverage of polar angle was from 17° to 150°. As a necessary installation step, the central drift chamber, the next detector component used for Belle tracking, had to be redesigned to accept the larger volume of SVD2.

The basic detection principles of the reverse biased SVD can be explained as follows. Once a charged particle passes through a DSSD, e-h pairs (with an average production energy of 3.5 eV) are generated along the particle path, and the charge then is collected through an applied electric field by sensitive electrodes. The holes drift to the p^+-doped side of the DSSD, electrons exactly opposite, to the n^+- doped side. If an electrode is not directly read-out, the charge will induce a signal on neighbouring strips due to non-zero capacitive coupling. Finally, the charge distributions obtained on the orthogonally segmented strips allow one to determine a two dimensional hit positions and hence, to reconstruct the particle track. Every charged particle traversing detector installed in a constant magnetic field follows a helicoidal trajectory, and its track can be mathematically described by 5 independent parameters. The most important ones used to describe the tracking performance are impact parameters in z, dz, and r-ϕ, dr. They are defined as a distance to the point of closest approach with respect to the interaction point in z and r-ϕ, respectively. Figure 2.5 shows the impact parameter resolutions estimated by Belle SVD group with cosmic ray muons.

2.2.4 Central Drift Chamber (CDC)

The central drift chamber is a large volume gas filled detector, installed in a uniform magnetic field. It primarily serves as a long lever arm for the central Belle tracking system and has to fulfill several physics driven requirements: efficient reconstruction of particle tracks, precise determination of their momenta and the measurement important for the particle identification - energy losses of charged particles by ionization, dE/dx.

The majority of B meson decay particles produced at KEKB collisions have momenta lower than 1 GeV/c and hence, the minimization of multiple scattering is necessary for successful Belle tracking performance. The optimal way, how to suppress the impact of multiple scattering and simultaneously retain a good dE/dx resolution, is to choose a low Z gas filling in the drift chamber. For the CDC 50 % helium - 50 % ethane mixture was chosen.

The configuration of CDC is schematically shown in Figure 2.6. The central drift chamber covers a polar angle region of $17° \leq \theta \leq 150°$, consists of 50 detection layers: 32 axial layers, 18 small-stereo-angle layers and 3 cathode layers, and has 8400 drift cells. A drift cell is represented by a sense

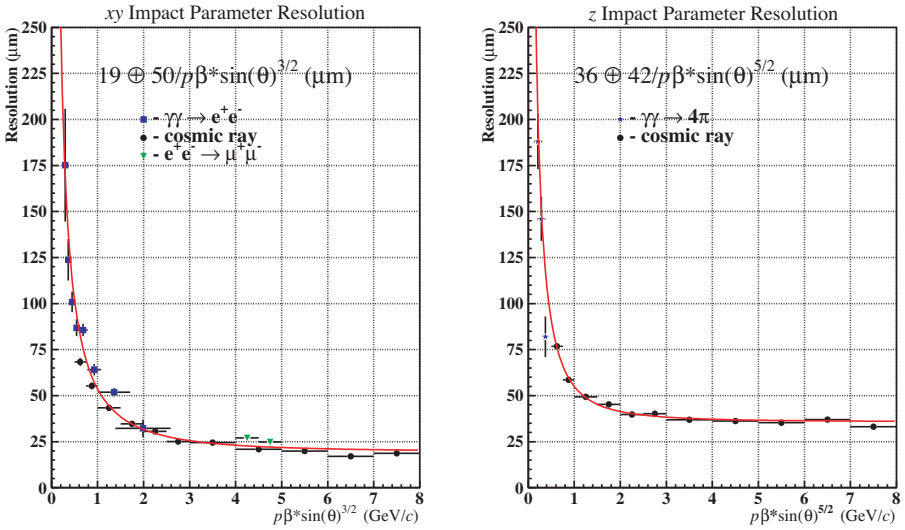

Fig. 2.5: Impact parameter resolution determined from cosmic data in r-ϕ plane (left) and z direction (right) for SVD1 detector [26]. Both plots are drawn as a function of particle pseudo-momentum $p\beta\sin(\theta)^{3/2}$ (right) and $p\beta\sin(\theta)^{5/2}$ (left), where p represents the track momentum and θ the track dip angle.

wire surrounded by 8 extra wires, which form the drift field. After a charged particle traverses the drift chamber and its drift cells, it ionizes atoms of the gas along its path. The ionized electrons are accelerated in the internal drift field and move towards the sense wire, gaining more and more energy and thus ionizing additional gas atoms. This in the end forms an electron avalanche and generates a huge electronic pulse, a 2D hit, at the sense wire. Hits collected by axial wires provide an r-ϕ information, hits on cathode layers and stereo wires, rotated by several tenths of mrad with respect to the axial wires, provide a z information. The CDC can measure hits with approximately 130 μm resolution in r-ϕ plane.

The amplitude of the signal read-out by CDC electronics corresponds to the charge collected by sense wires, and is used to determine particle $\mathrm{d}E/\mathrm{d}x$. The quantity of mean energy losses by ionization is a function of the velocity of incident particles. So for a certain momentum, different particle species have different energy losses, because their masses differ. The $\mathrm{d}E/\mathrm{d}x$ can be efficiently used to distinguish electrons, kaons, pions and protons. The central drift chamber was involved in the particle identification for tracks with $p < 0.8\,\mathrm{GeV}/c$ and $p > 2.0\,\mathrm{GeV}/c$; a scatter plot of the measured $\langle \mathrm{d}E/\mathrm{d}x \rangle$ versus particle momentum is shown in Figure 2.7.

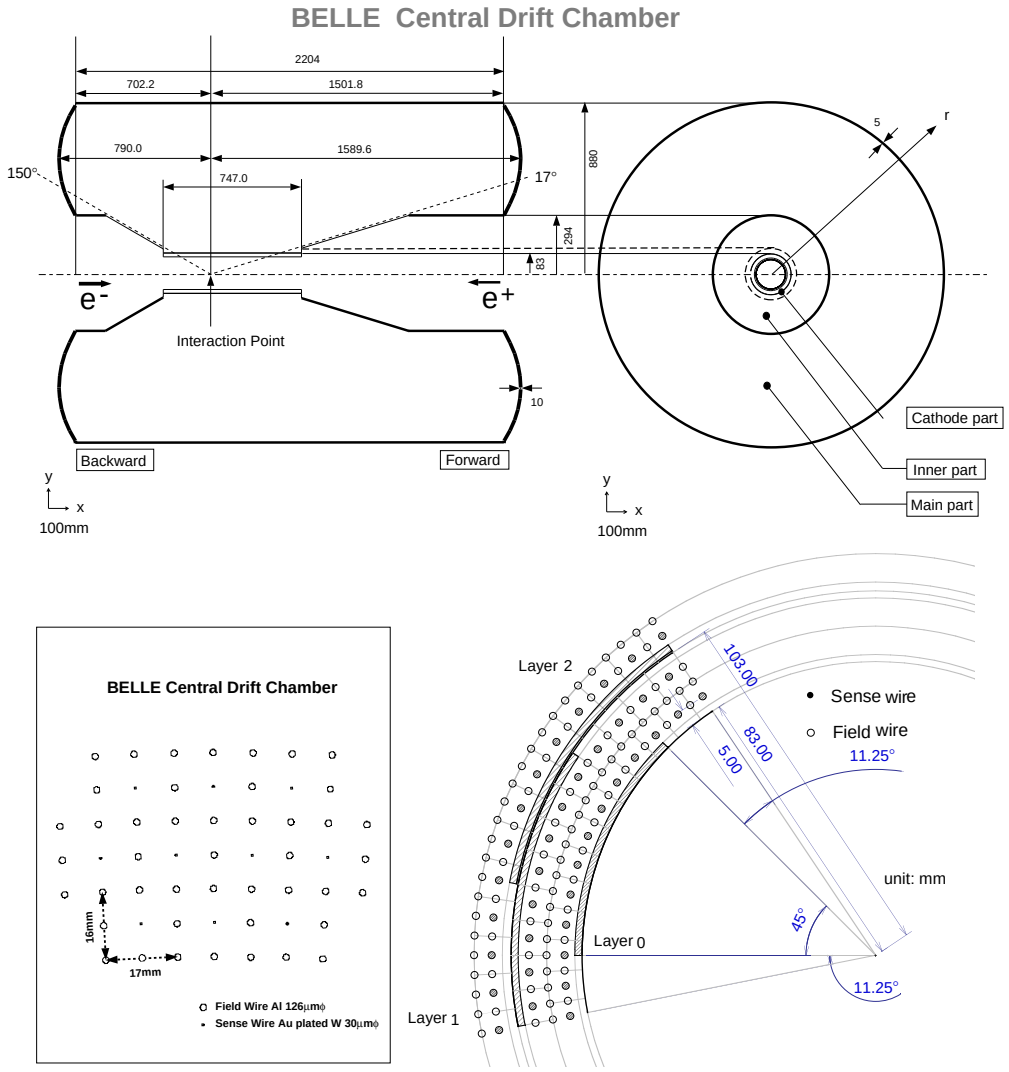

Fig. 2.6: Mechanical design of the Central Drift Chamber: schematic overview (upper), cell structure (lower left), and cell structure and the cathode sector (lower right) [21].

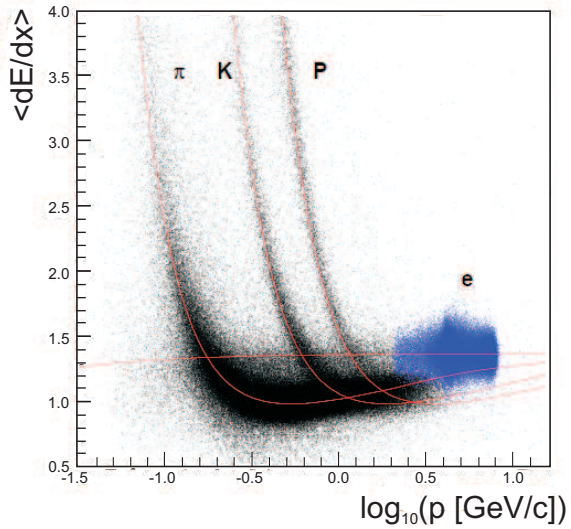

Fig. 2.7: A scatter plot of measured $\langle \mathrm{d}E/\mathrm{d}x \rangle$ versus particle momentum [21]. The expected mean losses for different particle species are illustrated with a red curve.

The reconstruction of charged tracks starts in the CDC with a track segment finder selecting hits which belong to the same track candidates. The track parameters are found from a χ^2 fit using a Kalman filtering technique. Once the CDC tracks are determined, they are extrapolated into the SVD to improve the fitted values of track parameters. For this purpose, the SVD hits are added to the CDC hits and newly created track candidates are refitted using the same technique as for the CDC only tracking. Finally, the improved values of track parameters are extracted and an update on charged particles information is performed.

2.2.5 Aerogel Cherenkov Counter (ACC)

An important component of the Belle particle identification system (PID) is represented by an Array of threshold silica aerogel Cherenkov Counters (ACC). ACC efficiently extends the PID momentum coverage beyond the common reach of $\mathrm{d}E/\mathrm{d}x$ measurements and time-of-flight measurements by CDC and TOF, respectively. Regarding the ACC sensitivity range, it was primarily designed to cover the PID of high momenta kaons and pions (above $\sim 1\,\mathrm{GeV}$), and to provide a good separation between them up to $3.5\,\mathrm{GeV}$ momenta [28].

A charged particle moving with a velocity higher than a speed of light (c), $v > c/n$, will emit a Cherenkov radiation inside an ACC medium with

a refractive index n. For the given n the threshold momentum for Cherenkov emission, p, is proportional to a particle mass, m, and inversely proportional to the refractive index: $p > mc/\sqrt{(n^2-1}$. Therefore, the efficient way to mutually separate $\pi^{\pm}/K^{\pm}$ in high momenta region is to choose a suitable refractive index. Since the B decay particles are produced with non-zero boost, the values of refractive index have to follow the forward-backward asymmetry of e^+e^- interactions. That can be efficiently achieved by positioning of ACC modules in sets in the Belle barrel region, with various refractive indices from 1.010 - 1.028. The ACC crystals in the forward end-cap region are made up of silica aerogel with $n = 1.030$. The higher index is chosen to incorporate the particle identification of low momenta particles into the PID system. The ACC crystals are the only PID detector providing particle identification in the very forward end-cap region.

A cross section of Belle detector with an emphasized ACC is shown in Figure 2.8. ACC consists of 960 counter modules positioned in sets by 60 in ϕ direction for the barrel part and 228 modules arranged in 5 concentric layers for the forward end-cap part. The total polar angle covered by ACC is $17° \leq \theta \leq 127°$. Emitted Cherenkov photons are measured by fine-mesh photo-multipliers, which are able to work in 1.5 T magnetic field.

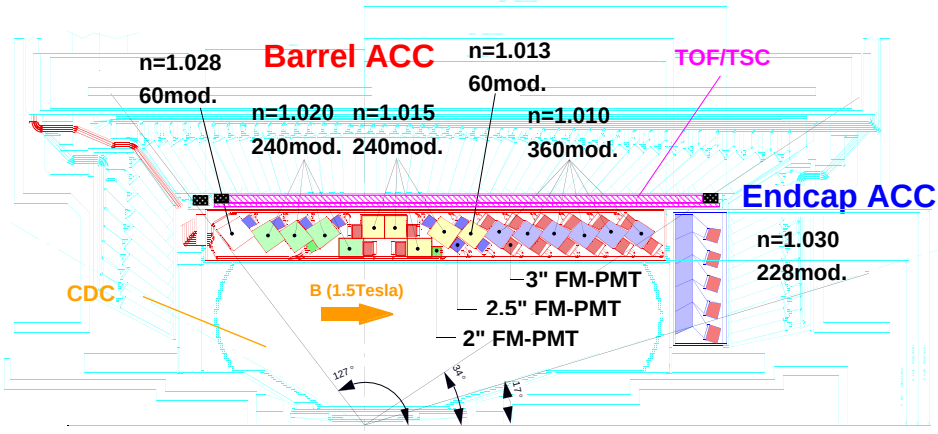

Fig. 2.8: A side view of the Belle detector with the emphasized barrel and endcap regions filled with ACC modules.

2.2.6 Time of Flight Counter (TOF)

The last technique used to identify particle species at Belle experiment consists in the measurement of flight time difference. Two particles having the same momentum, p, but different rest masses, m_1 and m_2, and traversing detector of the same thickness, L, pass a detection system with a following time difference (in relativistic limit $E \gg mc^2$):

$$\Delta t = \frac{L}{c}\left(\sqrt{1+\frac{m_1^2c^2}{p^2}} - \sqrt{1+\frac{m_2^2c^2}{p^2}}\right) \approx \frac{Lc}{2p^2}\left(m_1^2 - m_2^2\right) \qquad (2.1)$$

As clearly visible from the relation, the PID system based on the time of flight technique has to provide a very good time resolution. For kaons and pions with the same momentum of $1.2\,\mathrm{GeV}/c$ and flight length of 1.2 m, the flight time difference would be 300 ps. Hence, in order to efficiently separate pions from kaons up to about $1.2\,\mathrm{GeV}/c$ momenta (90% of all particles produced in $\Upsilon(4S)$ decays [21]), the detection system has to provide time resolution of ~ 100 ps.

The TOF measures the time difference between a collision at the interaction point and the time when a particle hits the TOF layer. The time resolution was designed to be 100 ps. In order to provide such a high resolution, fast plastic scintillators together with a read-out having fine-mesh-dynode photomultiplier tubes were chosen. In total, 64 TOF modules were positioned at a radius of 1.2 m and together, they formed a cylindrical structure covering polar angle from 33° to 121°. Each module was composed of two TOF counters and a Trigger Scintillation Unit (TSC). The TSC is a thin plastic scintillator and it's main purpose was to provide an input for the Belle data acquisition (DAQ) and triggering system. The detection path in TOF can be described as follows; light signals collected from the TOF scintillators are converted into photo-electrons and amplified by photomultipliers (PMTs). The read-out electronics outputs the PMT signals to a charge-to-time converter and then to a multihit time-to-digital converter for charge measurements.

The separation power of TOF for kaons, pions and protons is depicted in Figure 2.9. It shows a mass distribution for particle momenta below $1.2\,\mathrm{GeV}/c$.

2.2.7 Electromagnetic Calorimeter (ECL)

The main purpose of Belle electromagnetic calorimeter is to detect photons coming from B decays with high efficiency and good resolution in energy. Si-

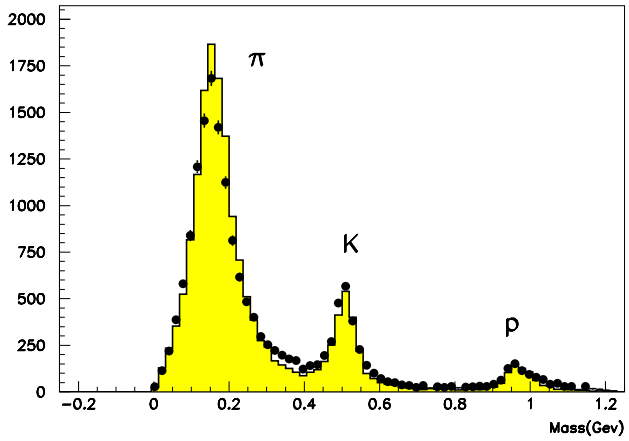

Fig. 2.9: TOF measured mass distribution for particle momenta lower than 1.2 GeV/c [21]. Expectations from MC simulations are shown as histograms, the measured data are depicted as black points.

multaneously, it is designed to provide an important information for the particle identification system, in terms of separation of electrons and positrons from other particle species. The electron identification relies primarily on a comparison of the charged particle momentum reconstructed by the CDC and the energy deposited at the ECL clusters. Electrons deposit most of their energy in the ECL, while muons or charged hadrons just a small fraction.

At high energies, electrons and positrons preferably lose their energy by Brehmsstrahlung, while photons by electron-positron conversion. These processes follow, one each other, repeating over and over again and producing an electromagnetic shower of deposited energy in the absorbing material of ECL. The energy deposited by primary particle per unit length exponentially decreases in the absorber, with a characteristic decay length X_0. As the shower cascade evolves, more and more particles carrying lower fraction of the original energy are generated. Once the energy achieves a critical energy, electrons (positrons) start losing preferably their energy by ionization, and hence, gammas pair production stops to have any effect on further shower development; the shower achieves its maximum and stops over a relatively low distance. The measurement of energy with electromagnetic calorimeter is based on these principles and thus, the energy released by cascade particles (mainly by ionization and excitation) can be taken as being proportional to the deposited energy of primary particle.

The ECL consists of 8736 thallium-doped (Tl) CsI crystal counters, where each crystal is tower shaped and has a height of 30 cm. From a physics point of view, this height corresponds to 16.2 X_0. The CsI crystals form

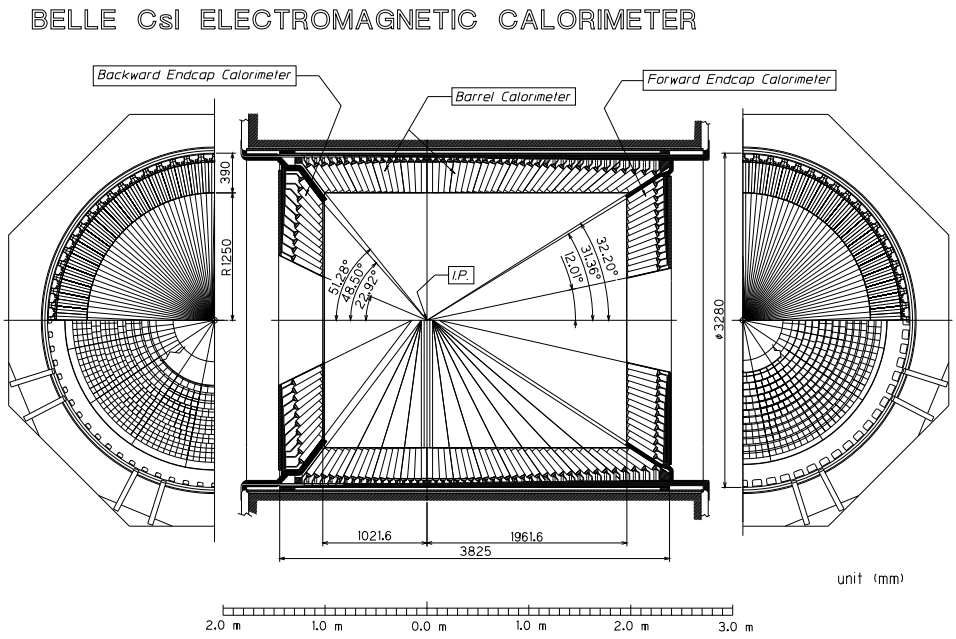

Fig. 2.10: Overall geometry layout of the Electromagnetic calorimetry [21].

a barrel section, 3.0 m in length and positioned at inner radius of 1.25 m, and annular end-caps positioned at $z = +2.0\,\mathrm{m}$ and $z = -1.0\,\mathrm{m}$ with respect to the interaction point. For details see a schematic Figure 2.10. Each crystal points towards the interaction point, but is slightly tilted in θ and ϕ in order to avoid photons escaping through the gaps between individual crystals. Regarding a polar angle, the ECL extends from 17° to 150°. Signals from the ECL crystals are read out with silicon photodiodes. Photons are reconstructed if they do not match extrapolated tracks of charged particles and have a lateral shape consistent with an electromagnetic shower.

The ECL has a good performance over a wide range of photon energies $20\,\mathrm{MeV} < E_\gamma < 5.4\,\mathrm{GeV}$, the nominal energy resolution is measured to be as follows:

$$\frac{\sigma_E}{E} = \left(1.34 \oplus \frac{0.066}{E} \oplus \frac{0.81}{E^{1/4}}\right)\% \tag{2.2}$$

Two photon invariant mass distributions in π^0 region and η region are shown in Figure 2.11, the evaluated resolutions, σ, are also shown.

2.2.8 Superconducting Solenoid (SC)

A crucial ingredient for a proper operation of the Belle tracking system is a superconducting solenoid. Its coil provides a magnetic field of 1.5 T in

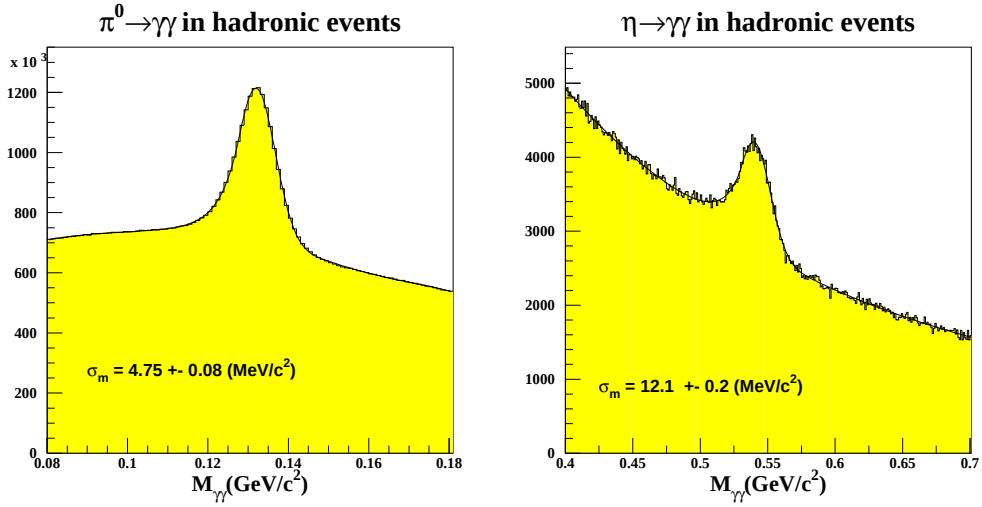

Fig. 2.11: Invariant mass distribution for typical hadronic events with two gammas in the final state: $\pi^0 \to \gamma\gamma$ (left) and $\eta \to \gamma\gamma$ (right) [21]. Each photon is required to have energy greater than 30 MeV in the barrel region.

a cylindrical volume of 3.4 m in diameter and 4.4 m in length and consists of a single layer of niobium-titanium-copper alloy, embedded in a high purity (99.99%) aluminum stabiliser. In order to return a magnetic flux back to the tracker an iron structure of the Belle detector (iron yoke) is used. This structure is also designed to effectively support the overall detection system and work as an absorber of KLM.

2.2.9 K_L and Muon System (KLM)

The KLM detection system was installed outside of the solenoidal magnetic field and its main purpose is to detect and distinguish K_L^0's from muons, with high efficiency and over a broad range of particle momenta, $p > 600$ MeV. The pattern left by muons in the detection system significantly differs from the one left by K_L^0's. In contrast to K_L^0's, the muons path matches the extrapolated track from the inner detector, and in addition, muons do not interact strongly and hence, travel further in the KLM system with much smaller direction deflections. In contrast, K_L^0 particles interact strongly in the iron or ECL and produce a shower of ionizing particles. The location of such a hadronic cascade determines K_L^0 direction, but due to fluctuations in the size of the shower, the energy of K_L^0 particles can not be sufficiently measured.

The KLM consists of several alternating layers of glass electrode resis-

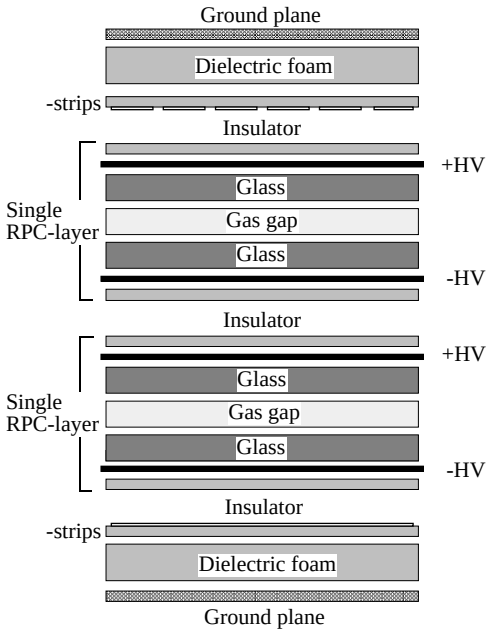

Fig. 2.12: Cross section of the KLM superlayer [21].

tive plate chambers (RPCs) and 4.7 cm-thick iron plates. In total, there are 15 detector layers with 14 iron layers positioned in the octagonal barrel region, and 14 detector layers in each of forward and backward end-cap region. Figure 2.12 shows a cross section of the KLM super-layer. Each RPC is composed of two high resistive electrodes separated by a gap, filled with a special gas mixture: 30% argon, 8% butane, and 62% freon. Once an ionizing particle traverses the gap, it initiates a streamer that results in a local discharge of the plates. The strength of such discharge is limited by the value of RPC resistivity and the quenching characteristics of the gas. In the end, the discharge induces a signal on external strips, which record the discharge location and time of its origin. The overall coverage of RPCs in terms of polar angle was $20^\circ < \theta < 155^\circ$.

2.2.10 Trigger and Data Acquisition

The Belle trigger system is used to select signal events and reject background events as efficiently as possible. Moreover, it works hand in hand with the Belle data acquisition system, responsible for the data read out from all sub-detector components. The trigger system reduces data event

rate in three subsequent steps: online data triggering with hardware Level-1 trigger and software Level-3 trigger; a Level 4 trigger based on event reconstruction and classification is performed offline. The Level-1 trigger can be schematically described as following: the CDC and SVD logics provide charged track signals, the TOF trigger system an event timing information, the ECL gives trigger signals for both neutral and charged particles, based on their deposited energy and ECL hits cluster counting, and finally, the KLM provides an additional information on muons. All these trigger signals are worked out by a Global Decision trigger Logic (GDL), which makes the final global decision. In January 2001, another step in the triggering design was introduced, a trigger Level-3, which uses fast track fitting algorithms to suppress background tracks not coming from the interaction point. The last level, Level-4, represents a pre-step for any data analysis.

3 Event Reconstruction

In contrast to $B^0 \to J/\psi K^0_S$, the η_c meson can be reconstructed from hadronic decays only rather than from a pure leptonic final state with relatively low combinatorial background. In total, there are three promising hadronic modes, which can be analysed to reconstruct η_c candidates; one with relatively low branching ratio, but with almost no combinatorial background, $\eta_c \to p\bar{p}$, and two 3-body decays: $\eta_c \to K^0_S K^\pm \pi^\mp$ and $\eta_c \to K^+K^-\pi^0$. The branching fractions together with the estimated average detection efficiencies, obtained from signal MC simulation studies, are summarized in Table 3.1.

Decay mode	$\mathcal{B}$	$\bar{\epsilon}$
$B^0 \to \eta_c K^0_S$, $\eta_c \to p\bar{p}$	$(5.9 \pm 1.1) \times 10^{-7}$	23 %
$B^0 \to \eta_c K^0_S$, $\eta_c \to K^0_S K^\pm \pi^\mp$	$(9.7 \pm 2.2) \times 10^{-6}$	6 %
$B^0 \to \eta_c K^0_S$, $\eta_c \to K^+K^-\pi^0$	$(5.0 \pm 1.1) \times 10^{-6}$	8 %

Tab. 3.1: PDG branching fractions and average detection efficiencies for the η_c decay modes [16].

In this chapter, the event reconstruction of the first hadronic mode, $\eta_c \to p\bar{p}$, which has been used to analyse CP violation in $B^0 \to \eta_c K^0_S$, will be explained.

3.1 Event Selection for $\eta_c \to p\bar{p}$

Starting with the final state particles: p, $\bar{p}$, π^+, π^-, in $B^0 \to \eta_c K^0_S$ (denoted further as a neutral mode), or p, $\bar{p}$, $K^\pm$, in $B^\pm \to \eta_c K^\pm$ (control sample, denoted further as a charged mode), we have gradually reconstructed the η_c resonance from $p\,\bar{p}$, K^0_S from $\pi^+\pi^-$, and then the B^0 or $B^\pm$ meson from $\eta_c\, K^0_S$ or $\eta_c\, K^\pm$, respectively. This has been done by combining given 4-momenta of all particle candidates and then, by applying a set of different selection

criteria. For this purpose signal MC, with 250 thousand events for each, SVD1 and SVD2 experiment, has been generated. Here, one B candidate decays generically and the other via the studied physics channel.

3.1.1 Hadronic Events

In e^+e^- collision at $\Upsilon(4S)$ resonance, non-hadronic processes, including τ-pair production, QED (Bhabha, two-photon) and beam-gas interaction, occur with similar or even larger cross sections than $B\bar{B}$ production. To remove these events, so-called *HadronB(J)* skimming procedure has been applied on data [29].

3.1.2 Charged Tracks

A helix in a magnetic field along z-axis is fully determined by five parameters: $\mathrm{d}r$, ϕ_0, κ, $\mathrm{d}z$ and $\tan\lambda$. The impact parameters $\mathrm{d}r$ and $\mathrm{d}z$ are radial and z positions, respectively, of the point of closest approach of the helix to a specified reference point, usually vertex. Here, an interaction point (IP) is used. The reconstructed charged tracks satisfy loose selection criteria on impact parameters, $|\mathrm{d}r| < 0.5\,\mathrm{cm}$ and $|\mathrm{d}z| < 3\,\mathrm{cm}$. These requirements have suppressed background tracks that do not originate from the IP.

An additional requirement on number of SVD hits has been imposed [30], so that a good quality vertex of the reconstructed B candidates can be determined. Only charged tracks with at least 2 hits in z-direction and 1 hit in $r\phi$-direction are considered.

3.1.3 Particle Identification

With information obtained from CDC ($\mathrm{d}E/\mathrm{d}x$), ACC and TOF, particle identification (PID) is determined using different likelihood ratios, $\mathcal{L}_{i/j} = \mathcal{L}_i/(\mathcal{L}_i + \mathcal{L}_j)$, where $\mathcal{L}_i$ ($\mathcal{L}_j$) represents the likelihood that a particle is of i (j) type. For kaons, a requirement of $\mathcal{L}_{\mathrm{K}/\pi} > 0.6$ has been applied [31], which is 86.3% (85.2%) efficient for kaons, in SVD1 (SVD2) experiment, with a 9.8% (10.5%) misidentification rate for pions. Furthermore, veto cuts have been applied on kaons consistent with electron hypothesis (electron-like kaons), $p(e) < 0.95$.

Protons and antiprotons are required to have likelihood ratios, $\mathcal{L}_{\mathrm{p}/\mathrm{K}}$ or $\mathcal{L}_{\mathrm{p}/\pi} > 0.4$, and similarly to kaons, candidates which are electron-like according to the information from CsI(Tl) are vetoed, $p(e) < 0.95$. These loose cuts significantly reduce $b\bar{b}$ generic background due to natural suppression of π-like or e-like proton and antiproton candidates, namely by 35% and 40%

in the charged mode and neutral mode, respectively, and retain 99.5% of all signal. For these studies, 10 streams of generic $b\bar{b}$ MC data samples have been used (10 × official Belle data sample).

3.1.4 K^0_S Reconstruction

All K^0_S candidates are reconstructed from pairs of oppositely charged tracks that satisfy the pion hypothesis and lie within the following mass window of $482\,\mathrm{MeV}/c^2 < m(\pi^+\pi^-) < 514\,\mathrm{MeV}/c^2$, which corresponds to $\pm 16\,\mathrm{MeV}$ ($\pm 4\sigma$, as defined in [32]). In order to optimize the selection of K^0_S candidates, *goodKs* cut has been applied [32].

3.1.5 η_c and B Reconstruction

The η_c resonance is reconstructed from the proton and antiproton candidates within the mass window of $2.84\,\mathrm{GeV}/c^2 < m(p\bar{p}) < 3.03\,\mathrm{GeV}/c^2$. Such an asymmetric mass window has been chosen, in order to limit the interference with the J/ψ particle (see the J/ψ properties in Table 1.1). Based on 10 streams of generic $b\bar{b}$ MC studies, the right limit of the interval has been optimized in the way that the number of contributing J/ψ events into the η_c distribution remains, in maximum, at the level of statistical error of the number of η_c events only, see Fig. 3.1.

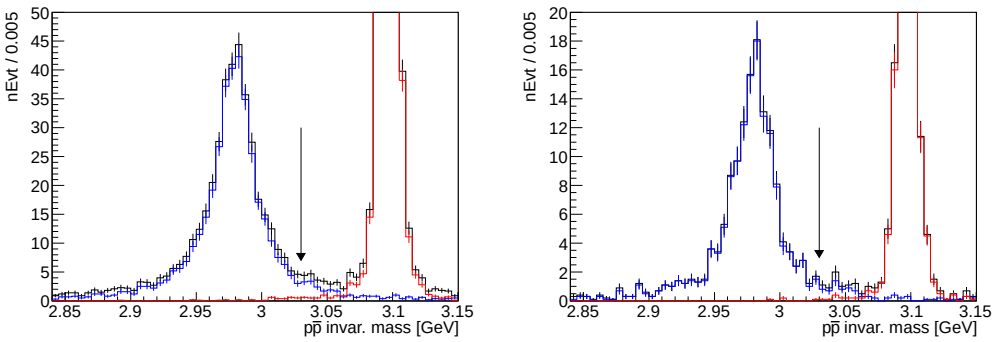

Fig. 3.1: Reconstructed $p\bar{p}$ invariant mass with two $c\bar{c}$ states: η_c (blue) and J/ψ (red). The left picture shows results for the charged mode, the right for the neutral mode. The optimal right boundary of η_c mass window is emphasized by an arrow.

As the η_c decays promptly after the B decay, a vertex defined by p and $\bar{p}$ tracks also defines the decay vertex of the B meson. In the neutral mode,

the K^0_S track is determined with a large error at the IP, due to its displaced vertex, and can't be thus used in B vertexing. In the charged mode, the same condition has to be applied, as the mode is used, in the end, to calibrate the neutral mode (to correct for the differences between MC and data). Therefore, no additional $K^\pm$ track information has been used in $B^\pm$ vertexing either.

Based on all combinations of η_c and K^0_S ($K^\pm$), a list of B^0 ($B^\pm$) candidates has been formed. Reconstructed B candidates are described with two nearly orthogonal kinematic variables: the beam-constrained mass, $M_{bc} \equiv \sqrt{(E^{CMS}_{beam})^2 - (p^{CMS}_B)^2}$, and the energy difference $\Delta E \equiv E^{CMS}_B - E^{CMS}_{beam}$, where E^{CMS}_{beam} represents the beam energy, $(E^{CMS}_{e^+} + E^{CMS}_{e^-})/2$, and E^{CMS}_B (p^{CMS}_B) the energy (momentum) of the reconstructed B meson, all evaluated in the center-of-mass system (CMS). On average, 1.006 B^0 (1.01 $B^\pm$) are reconstructed per event as shown in Fig. 3.2 and naturally, only one candidate is chosen and used then in further analysis.

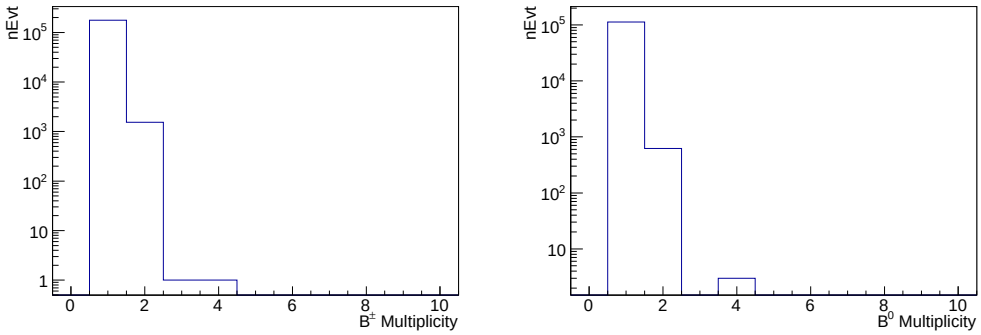

Fig. 3.2: Multiplicity of reconstructed $B^\pm \to \eta_c K^\pm$ (left) and $B^0 \to \eta_c K^0_S$ (right), $\eta_c \to p\bar{p}$.

For this particular physics channel, the multiplicity looks rather low and the best B candidate selection might be random-like. Nevertheless, other selection methods based on M_{bc} or η_c invariant mass should be considered too. For the $p\bar{p}$ channel with a very low multiplicity the random based selection procedure brings comparable results as the other two methods. On the other hand, for the $K^0_S K^\pm \pi^\mp$ and $K^\pm K^\mp \pi^0$ channels, which are meant to be used in the final combined CP fitter too, only M_{bc} or η_c invariant mass based methods bring efficient results. So, in the end, only these two selection methods have been studied, both using 6 streams of generic (b, u, d, c, s) MC data samples. Obtained results are summarized in Table 3.2 and shown in Figure 3.3. (Concerning the plots, all selection criteria, including the criteria described later in this chapter, such as continuum suppression cuts or peaking

Selection	Mode	$\varepsilon_{\mathrm{SVD1}}$ [%]	$\varepsilon_{\mathrm{SVD2}}$ [%]	f_{SVD1} [%]	f_{SVD2} [%]
M_{η_c}-based	charged	31.62	36.28	0.12	0.09
M_{bc}-based	charged	**33.33**	**38.12**	0.05	0.03
M_{η_c}-based	neutral	19.02	24.13	0.07	0.10
M_{bc}-based	neutral	**20.03**	**25.36**	0.03	0.06

Tab. 3.2: Detection efficiencies, $\varepsilon = N_{\mathrm{rec}}/N_{\mathrm{gen}}$, and fractions of misidentified B mesons in all reconstructed, $f_{\mathrm{misID}} = N_{\mathrm{misID}}/N_{\mathrm{rec}}$. Both are shown for different best candidate selection methods and decay modes.

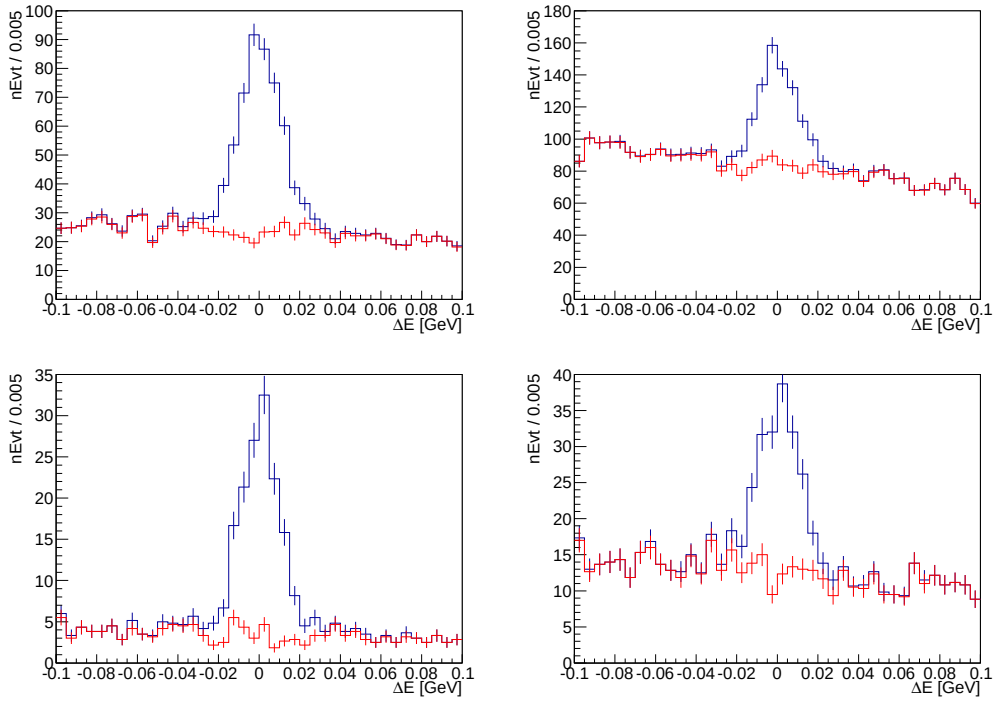

Fig. 3.3: ΔE distribution for two different best candidate selection procedures, one based on M_{bc} (left), the other based on η_c invariant mass (right). Plots for the charged mode are compared at the top, for the neutral mode at the bottom.

background vetoes, have been applied.)

The previous Belle analysis [17], in all decay channels: $p\bar{p}$, $K^0_S K^{\pm}\pi^{\mp}$ and $K^{\pm}K^{\mp}\pi^0$, as well as BaBar analysis [12], in $K^0_S K^{\pm}\pi^{\mp}$ channel, applied the η_c invariant mass based best candidate selection. Since the η_c determines the B vertex, we think, that such a selection might bias the final results and therefore, the M_{bc} based procedure has been applied. Moreover, using the M_{bc}, one can significantly reduce the M_{bc} window from a fit range, $5.20\,\mathrm{GeV}/c^2 < M_{bc} < 5.29\,\mathrm{GeV}/c^2$, in case of η_c mass based selection, to a signal window, $5.271\,\mathrm{GeV}/c^2 < M_{bc} < 5.290\,\mathrm{GeV}/c^2$, and thus significantly improve signal to background ratio. Simultaneously, the η_c window can be then extended from $2.92\,\mathrm{GeV}/c^2 < M_{\eta_c} < 3.03\,\mathrm{GeV}/c^2$, to already optimized $2.84\,\mathrm{GeV}/c^2 < M_{\eta_c} < 3.03\,\mathrm{GeV}/c^2$, and thus increase the detection efficiency. On the other hand, the fitting procedure might be more complicated as the number of correctly reconstructed signal events in ΔE distribution does not necessarily equal to the number of η_c signal events. (Due to fact that η_c represents a decay product of B meson.) The final ΔE window has been set in the following range: $-0.1\,\mathrm{GeV} < \Delta E < +0.1\,\mathrm{GeV}$.

3.1.6 Continuum Suppression

The dominant background for this measurement comes from the continuum processes, i.e. $e^+e^- \to q\bar{q}$ (where $q = u, d, s, c$). In the $\Upsilon(4S)$ CMS frame, the $B\bar{B}$ pairs are produced with very small energy release ($\sim 20\,\mathrm{MeV}$) and thus, tend to have a nearly spherical event topology. In contrast, the light quarks are generated with the jet-like event structure. As the continuum and $B\bar{B}$ events have such different event "shapes", either different individual topological variables or Fisher's linear discrimination function combining the discrimination power of all these topological variables together (further denoted as Fisher discriminant) [33], $\mathcal{F}_{B\bar{B}/q\bar{q}}$, can be used to suppress the continuum background. Since the η_c resonance has a big decay width of 28.6 MeV (Tab. 1.1) and high contribution of continuum is thus expected, compared to other $b \to c\bar{c}s$ processes, the latter approach with Fisher discriminant, separately used for SVD1 and SVD2 experiments, has been used.

In total, 10 event topology variables have been combined in the Fisher discriminant, $\mathcal{F}_{B\bar{B}/q\bar{q}} = \sum_{i=1}^{N=10} \alpha_i x_i$, where α_i represent weight coefficients which maximize the separation of signal events from continuum background, and x_i are the individual topological variables. The training procedure has been done using the signal Monte Carlo and 2 streams of generic (u, d, s, c) MC data. Due to a very limited statistics in Belle $\Upsilon(4S)$ off-resonance data sample, only the MC data could be practically used as a $q\bar{q}$ training sample, with M_{bc} window set in the full region from 5.20 to $5.29\,\mathrm{GeV}/c^2$ to increase

the statistics. The discriminating variables, combined in the $\mathcal{F}_{B\bar{B}/q\bar{q}}$, are listed here:

- The cosine of thrust angle, $\cos\vartheta_{\rm thr}$, which is defined as a scalar product of "signal" thrust vector, calculated from the momenta of particles coming from the reconstructed B candidate (signal B), and "other" thrust vector, calculated from the momenta of remaining particles. The $\cos\vartheta_{\rm thr}$ is flat for $B\bar{B}$ events and peaks at ±1 for the continuum.

- Reduced Fox-Wolfram moment, R_2, [34], defined as the ratio of H_2 to H_0. Here, H_l, $l = 0, 1, \ldots$ represent the Fox Wolfram moments defined as following:

$$H_l = \sum_{i,j} \frac{|p_i||p_j|}{E^2} P_l(\cos\theta_{ij}), \text{ e.g. } P_2(\cos\theta_{ij}) = \frac{1}{2}(3(\cos\theta_{ij})^2 - 1), \quad (3.1)$$

  where indices i and j run over all final state particles, E is the total visible energy of the event, θ_{ij} is the opening angle between particle i and j and P_l is the l-th Legendre polynomial. For $B\bar{B}$ events (spherical limit): $R_2 \to 0$; for jet-like events (back-to-back limit): $R_2 \to 1$.

- 8 modified Fox-Wolfram moments, $4\,H_l^{\rm so}$ and $4\,H_l^{\rm oo}$, $l = 0, 1, 2, 3$, [35]. They have the same form as defined in Equation (3.1), only the indices i and j run over specific particles, coming either from the reconstructed B (signal - denoted by the superscript s) or from the other B (denoted by the superscript o). Only $H_l^{\rm so}$ and $H_l^{\rm oo}$ have been utilized, the $H_l^{\rm ss}$ are highly correlated with the measured variables: $M_{\rm bc}$, M_{η_c} and ΔE.

As some of the variables combined in the $\mathcal{F}_{B\bar{B}/q\bar{q}}$: typically R_2, $H_1^{\rm so}$ and $H_3^{\rm so}$, might be correlated with the individual observables used in the fitter: ΔE and M_{η_c}, necessary calculations of possibly dangerous correlations ρ have been done, correlations checked and summarized in Tab. 3.3 (charged mode), 3.4 (neutral mode). The observed values are negligible, at most at 2.1 % level for ΔE and 0.8 % level for M_{η_c}. The non-negligible correlations, with $M_{\rm bc}$, will not influence the final results as the $M_{\rm bc}$ has already been used for the best candidate selection and thus, will not be used in the fitter.

Together with the $\mathcal{F}_{B\bar{B}/q\bar{q}}$, we have also used the cosine of the B flight direction with respect to the z-axis, $\cos\theta_B$, in order to improve the total separation of signal from the continuum background. As the $\Upsilon(4S)$ is a spin 1 particle and the B mesons are pseudoscalars, i.e. spin 0 particles, the conservation of angular momentum requires $B\bar{B}$ pair to be in a p-wave state. Therefore, the signal has a $(1 - \cos^2\theta_B)$ distribution in contrast to the flat distribution of continuum.

ρ [%]	R_2	H_0^{so}	H_1^{so}	H_2^{so}	H_3^{so}
ΔE (SVD1)	$+\mathbf{1.5}$	-0.04	-0.8	$+0.004$	-0.8
M_{η_c} (SVD1)	$+0.4$	-0.4	-0.3	-0.2	$+0.03$
ΔE (SVD2)	-0.4	$+0.5$	$+0.4$	$+0.4$	$+0.4$
M_{η_c} (SVD2)	-0.4	-0.01	$+\mathbf{0.5}$	-0.4	$+0.2$
		H_0^{oo}	H_1^{oo}	H_2^{oo}	H_3^{oo}
		-1.4	$+0.39$	$+0.8$	$+0.4$
		$+0.4$	$+0.3$	-0.3	$+0.04$
		-1.3	$+0.2$	-0.3	$+0.05$
		$+0.05$	-0.007	0.04	$+0.06$

Tab. 3.3: Charged mode: correlations between R_2, modified Fox-Wolfram moments, $H_l^{\mathrm{so,\,oo}}$, and observables, ΔE and M_{η_c}, separately calculated for SVD1 and SVD2 experiments.

ρ [%]	R_2	H_0^{so}	H_1^{so}	H_2^{so}	H_3^{so}
ΔE (SVD1)	$+1.3$	$+0.4$	-1.0	$+0.2$	-0.6
M_{η_c} (SVD1)	$+0.06$	-0.5	$+0.2$	-0.2	-0.3
ΔE (SVD2)	$+0.3$	-0.4	$+0.3$	$+0.04$	$+0.6$
M_{η_c} (SVD2)	-0.7	$+0.2$	-0.1	-0.4	-0.2
		H_0^{oo}	H_1^{oo}	H_2^{oo}	H_3^{oo}
		$-\mathbf{2.1}$	$+0.3$	-0.8	$+1.6$
		-0.3	-0.1	$+0.3$	$+0.2$
		-1.6	$+1.1$	-0.4	-0.5
		-0.5	$+0.7$	-0.2	$-\mathbf{0.8}$

Tab. 3.4: Neutral mode: correlations between R_2, modified Fox-Wolfram moments, $H_l^{\mathrm{so,\,oo}}$, and observables, ΔE and M_{η_c}, separately calculated for SVD1 and SVD2 experiments.

Finally, signal and background distributions, both for the Fisher discriminant and $\cos\theta_B$, have been fitted, using the unbinned maximum likelihood method. For the $\mathcal{F}_{B\bar{B}/q\bar{q}}$ signal PDF (Probability Density Function) a sum of two bifurcated gaussians with a central mean value has been used:

$$\mathcal{P}_{sig}(\mathcal{F}_{B\bar{B}/q\bar{q}}) = f.G(\mu, \sigma_L, \sigma_R) + (1-f).G(\mu, k_{\sigma_L}.\sigma_L, k_{\sigma_R}.\sigma_R) \tag{3.2}$$

For the $\mathcal{F}_{B\bar{B}/q\bar{q}}$ background PDF only a single bifurcated gaussian has been used:

$$\mathcal{P}_{bkg}(\mathcal{F}_{B\bar{B}/q\bar{q}}) = G(\mu, \sigma_L, \sigma_R) \tag{3.3}$$

For the $\cos\theta_B$, the signal PDF has been defined as:

$$\mathcal{P}_{sig}(\cos\theta_B) = \mathcal{N}(1 - a.\cos^2\theta_B), \tag{3.4}$$

whereas the $\cos\theta_B$ background PDF follows as:

$$\mathcal{P}_{bkg}(\cos\theta_B) = \mathcal{N}(1 + a.\cos\theta_B) \tag{3.5}$$

The Fisher PDFs, separately depicted for the charged mode and neutral mode, and, for the SVD1 and SVD2 experiments, are shown in Fig. 3.4.

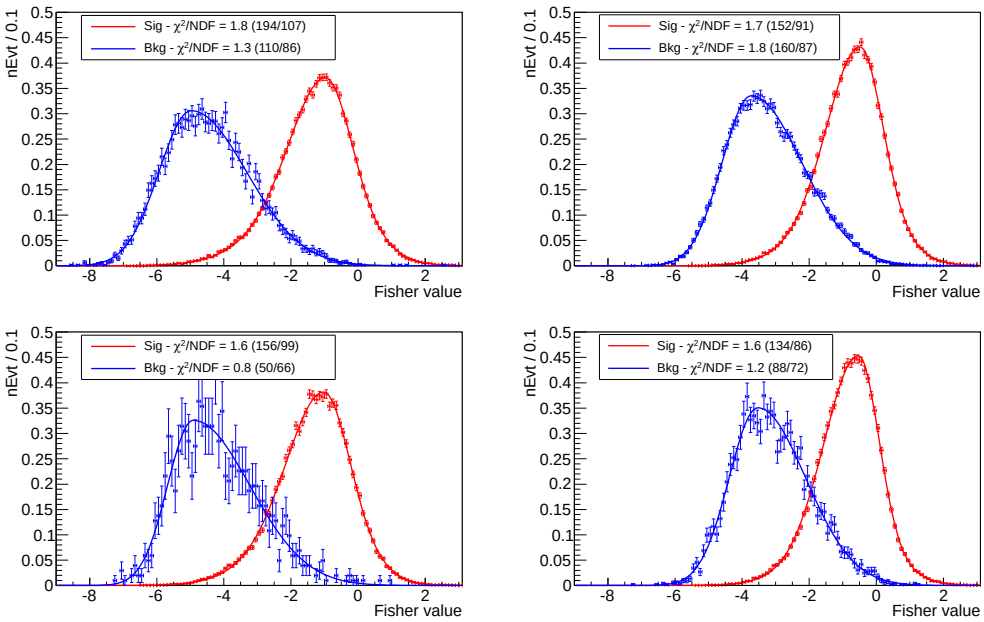

Fig. 3.4: Distributions of $\mathcal{F}_{B\bar{B}/q\bar{q}}$ for the charged mode (top) and neutral mode (bottom), SVD1 (left) and SVD2 (right) experiments. The signal PDF is shown in red color, the background PDF in blue color.

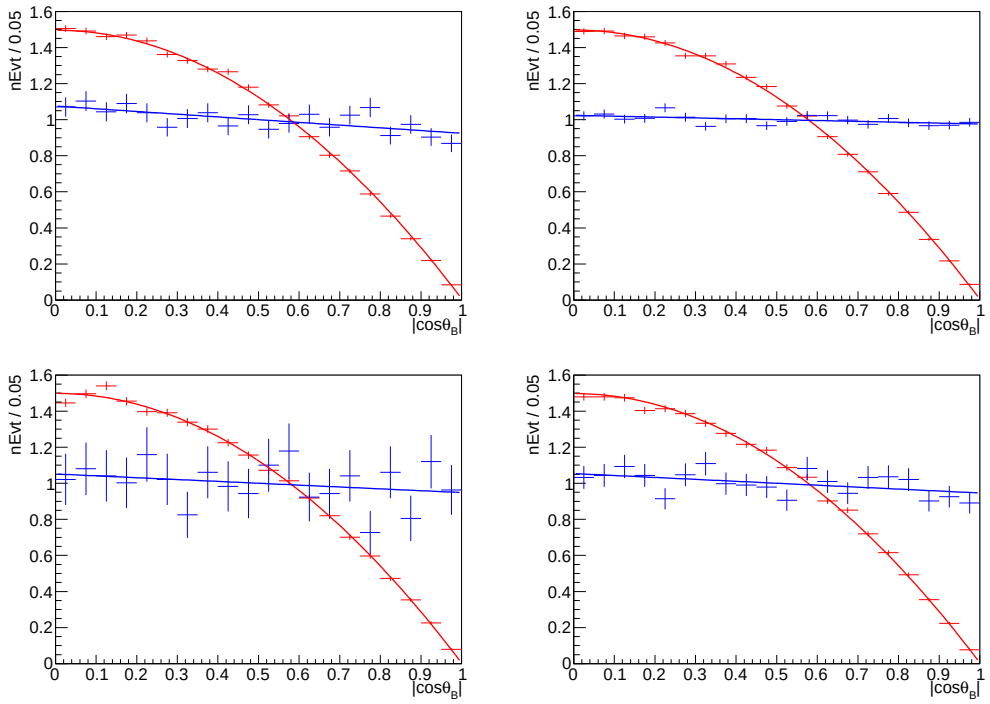

Fig. 3.5: Distributions of $\cos\theta_{\rm B}$ for the charged mode (top) and neutral mode (bottom), SVD1 (left) and SVD2 (right) experiments. The signal PDF is shown in red color, the background PDF in blue color.

The distributions of the cosine of the B flight direction are shown in the same configurations as Fisher distributions in Fig. 3.5.

Since the Fisher discriminant and $\cos\theta_{\rm B}$ represent mutually uncorrelated variables, the signal (background) likelihoods, formed from individual PDFs, can be multiplied together to form a total signal (background) likelihood $\mathcal{L}_{\rm sig}$ ($\mathcal{L}_{\rm bkg}$). A likelihood ratio, constructed from such likelihoods as following:

$$\mathcal{LR} = \frac{\mathcal{L}_{\rm sig}}{\mathcal{L}_{\rm sig} + \mathcal{L}_{\rm bkg}} \tag{3.6}$$

can be then used (see Fig. 3.6) to suppress the continuum background while keeping the number of signal events at highest possible level.

In general, there exist several methods to optimize a selection cut on the $\mathcal{LR}$. (Further denoted as a continuum suppression cut, $\mathcal{CS}_{\rm cut}$.) First, one can maximize a so-called figure of merit (F.O.M.):

$$\text{F.O.M.} = \frac{N_{\rm sig}}{N_{\rm sig} + N_{\rm bkg}} \tag{3.7}$$

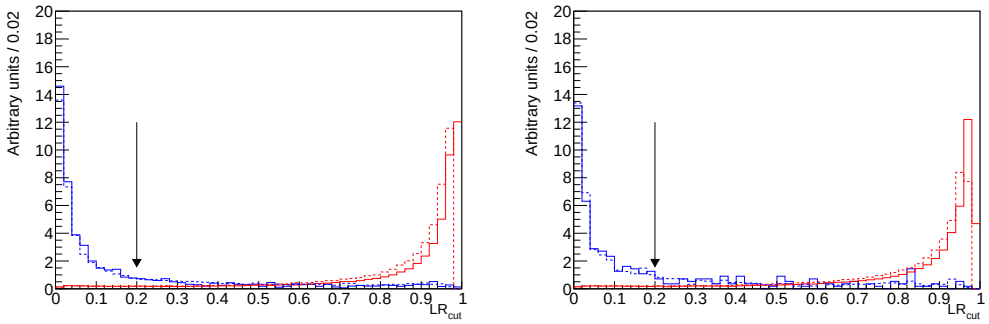

Fig. 3.6: Likelihood ratio for the charged mode (left) and the neutral mode (right). The red line describes signal events, the blue line continuum background. The results for SVD1 experiment are shown with a solid line, for SVD2 experiment with a dashed line. The optimized value of $\mathcal{CS}_{\text{cut}}$ has been stressed by an arrow.

which, practically, means a minimization of a statistical error with respect to the measured number of signal events. Second, one can keep the $\mathcal{CS}_{\text{cut}}$ as low as possible, such as the number of signal events remains almost untouched, but the background is still significantly suppressed. The first approach is usually preferred when branching fraction is the main aim of the analysis, the second when CP violating parameters are of the main concern. For the measurement of CP violating parameters the F.O.M. approach doesn't necessarily bring more precise results, as the error of the parameters is still mainly dominated by statistical fluctuations and therefore, high signal efficiency is desirable. Moreover, the second approach minimally influences the number of signal events and thus, no extra systematic error is generated due to the cut. Third, as a new method, the difference between signal and background efficiencies has been maximized and used. Such an approach defines the $\mathcal{CS}_{\text{cut}}$ as a point until which one cuts out more background than signal events while increasing the value of the cut.

From the prospective of the second approach, the $\mathcal{CS}_{\text{cut}}$ has been found to be optimal at 0.2 (Fig. 3.6), from the prospective of the third approach at 0.5 (Fig. 3.7). The final optimization based on the real data (control sample) has shown that the branching ratio is more or less independent on the value of the cut, and thus, the lowest possible value has been chosen as the most optimal. The $\mathcal{CS}_{\text{cut}}$ has been set to 0.2, which naturally selects: 96.1 % (96.1 %) of the signal events for SVD1 (SVD2) and rejects 77.1 % (71.4 %) of the continuum background in the charged mode. In the neutral mode, the numbers are slightly worse: 96.2 % (96.0 %) of the signal events for SVD1 (SVD2) has been retained, while 74.6 % (68.4 %) of the continuum

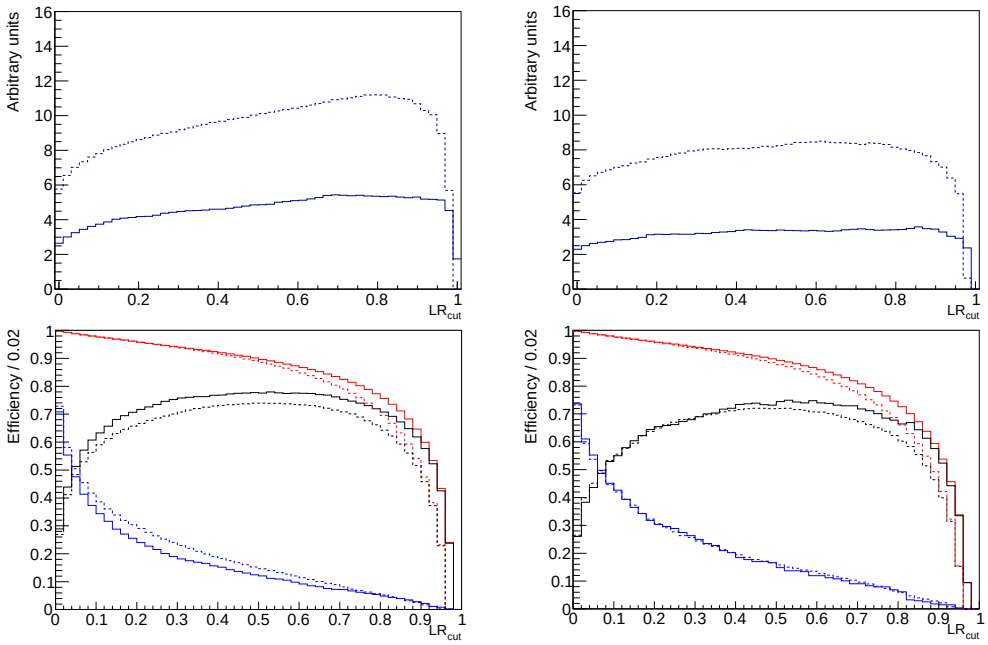

Fig. 3.7: F.O.M. (top) and efficiencies (difference of efficiencies) (bottom) for the charged mode (left) and the neutral mode (right). The solid line shows results for SVD1 experiment, dashed line for SVD2 experiment. The red line describes efficiencies of signal events, blue line efficiencies of background events and black line the difference of signal and background efficiencies, all expressed with respect to the applied $\mathcal{LR}$ ($\mathcal{CS}_{\text{cut}}$).

background has been rejected.

3.1.7 Peaking Background Suppression

The second non-negligible background comes from the generic charm decays of the B meson. This background has been found to peak in the signal region of the measured mode. In order to eliminate such sources of the peaking background, different veto cuts are usually applied. In the neutral mode, there exists only one non-negligible decay with the same final states as the measured mode, $B^0 \to \overline{\Lambda}_c^- p, \overline{\Lambda}_c^- \to \bar{p}K_S^0$. It has been efficiently suppressed using a following veto: 2271 MeV$< m(\bar{p}K_S^0) <$ 2301 MeV, while loosing 1.6 % of all signal, see Figure 3.8. In the charged mode, there has not been found any significant source of the peaking background.

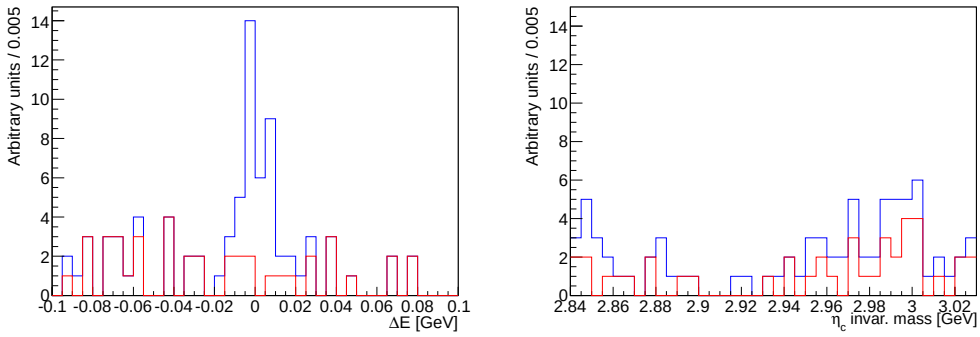

Fig. 3.8: ΔE (left) and η_c invariant mass distribution obtained from the generic $b\bar{b}$ MC study, before (blue) and after (red) application of $m(\bar{p}K_S^0)$ veto.

3.1.8 Time Measurement, Vertexing and B Tagging

Since the $B^0_{\rm rec}$ and $\bar{B}^0_{\rm tag}$ mesons are approximately at rest in the $\Upsilon(4S)$ CMS, the difference in decay time between the two B mesons, Δt, can be determined from the displacement in z direction between the final state decay vertices as:

$$\Delta t \approx \frac{z_{\rm rec} - z_{\rm tag}}{\beta\gamma c} \equiv \frac{\Delta z}{c(\beta\gamma)_\Upsilon}, \tag{3.8}$$

where the Lorentz boost, $(\beta\gamma)_\Upsilon$, is approximately 0.425, produced nearly along the z-axis.

The vertex of reconstructed B candidates has been determined from the charged daughters of η_c resonance, p and $\bar{p}$, and in addition, using (via

the mathematical method of Lagrange multipliers) the known information of e^+e^- IP profile in x and y direction (IP constraint fit). Moreover, the measured IP profile had to be, on top of that, smeared in the x-y plane, to account for the finite flight length of the B meson in transverze direction. An IP constraint, which is used in the kinematic fit exactly this way, is called a beam pipe constraint. It is due to a fact that the IP profile is represented by an infinite tube in z direction. This approach significantly helps improve the final Δt resolution while reducing the Δt bias compared to a full IP profile constraint [36]. Moreover, because of the IP profile, it is possible to reconstruct a decay vertex using even a single track measurement. Concerning the kaon track in the charged mode, it has not been used in the kinematic fit as the mode is intended to calibrate the neutral mode and thus, the same fitting conditions have to be applied. In order to obtain the Δt distribution, the tag side vertex has been reconstructed WTagTabfrom the tracks not assigned to $B^0_{\rm rec}$, using the TagV algorithm, [37, 38]. Finally, all events had to pass the time window, $|\Delta t| < 70\,{\rm ps}$, and the fit had to converge with the vertex goodness-of-fit, $h^{\rm rec,tag} \equiv (\chi^{2\,\rm rec,tag}_{\rm total} - \chi^{2\,\rm rec,tag}_{\rm IP})/{\rm ndf}^{\,\rm rec,tag} < 50$ for events with multi-track vertices, and with $\sigma_{\rm z}^{\rm rec,tag} < 200\,\mu{\rm m}$ and $\sigma_{\rm z}^{\rm rec,tag} < 500\,\mu{\rm m}$ for events with multi-track and single-track vertices, respectively.

The flavour tag of other B, denoted as $B_{\rm tag}$, has been determined using the tagging routine, Hamlet, described in detail in [39], for brief summary see Appendix A. The tagging information is represented by two parameters: $B_{\rm tag}$ flavour (charge), q, and a parameter, r. This parameter is an event-by-event, MC determined flavour-tagging dilution factor that ranges from $r = 0$ for B mesons with no flavour discrimination to $r = 1$ for unambiguous flavour assignment and is divided into 7 independent r-bins, indexed by l and defined in Table 3.5.

r-bin index	**r-bin region**
0	0.000 - 0.100
1	0.100 - 0.250
2	0.250 - 0.500
3	0.500 - 0.625
4	0.625 - 0.750
5	0.750 - 0.875
6	0.875 - 1.000

Tab. 3.5: Belle definition of individual r-bins, indexed by l.

The mistag probability, w, connected with the dilution factor r by a following relation:

$$r = 1 - 2w, \tag{3.9}$$

and the difference between the wrong tag probabilities, Δw, defined as:

$$\Delta w = w_{\mathrm{B}^0} - w_{\bar{\mathrm{B}}^0}, \tag{3.10}$$

where the w index denotes the flavour of the tag side, have been, for clarity, summarized in the Table 3.6. These parameters are essential for the precise measurement of CP violation parameters (1.1) and have been extracted from the MC and flavour specific data studies [13, 40].

All events which have not successfully passed the tagging or vertexing procedure have been discarded from the analysis.

l	**MC** w_l	**MC** Δw_l	**Data** w	**Data** Δw_l
SVD1				
0	0.5000	$+0.0000$	$0.5000^{+0.0000}_{-0.0000}$	$+0.0000^{+0.0000}_{-0.0000}$
1	0.4208	$+0.0583$	$0.4189^{+0.0072}_{-0.0060}$	$+0.0570^{+0.0089}_{-0.0092}$
2	0.3003	$+0.0057$	$0.3299^{+0.0071}_{-0.0064}$	$+0.0126^{+0.0092}_{-0.0091}$
3	0.2193	-0.0393	$0.2339^{+0.0074}_{-0.0077}$	$-0.0148^{+0.0104}_{-0.0100}$
4	0.1546	$+0.0047$	$0.1706^{+0.0069}_{-0.0064}$	$-0.0006^{+0.0090}_{-0.0089}$
5	0.0916	$+0.0119$	$0.0998^{+0.0068}_{-0.0088}$	$+0.0089^{+0.0093}_{-0.0093}$
6	0.0229	-0.0059	$0.0229^{+0.0043}_{-0.0046}$	$+0.0047^{+0.0057}_{-0.0058}$
SVD2				
0	0.5000	$+0.0000$	$0.5000^{+0.0000}_{-0.0000}$	$+0.0000^{+0.0000}_{-0.0000}$
1	0.4122	$+0.0041$	$0.4188^{+0.0042}_{-0.0036}$	$-0.0088^{+0.0040}_{-0.0039}$
2	0.3078	$+0.0103$	$0.3193^{+0.0032}_{-0.0028}$	$+0.0104^{+0.0035}_{-0.0037}$
3	0.2128	-0.0048	$0.2229^{+0.0037}_{-0.0035}$	$-0.0109^{+0.0041}_{-0.0042}$
4	0.1499	$+0.0015$	$0.1632^{+0.0033}_{-0.0042}$	$-0.0186^{+0.0042}_{-0.0046}$
5	0.0913	$+0.0144$	$0.1041^{+0.0032}_{-0.0037}$	$+0.0017^{+0.0040}_{-0.0039}$
6	0.0219	$+0.0019$	$0.0251^{+0.0022}_{-0.0031}$	$-0.0036^{+0.0024}_{-0.0024}$

Tab. 3.6: Summary of w-tag probabilities and mistag differences, Δw, used in this analysis for Monte Carlo and experimental data [13, 40]. Different values are used for SVD1 and SVD2 experiments.

3.1.9 Detection Efficiency

After applying all the selection criteria, detection efficiencies have been determined from the signal Monte Carlo studies using the following relation:

$$\varepsilon = N_{\rm rec}/N_{\rm gen}, \tag{3.11}$$

where $N_{\rm rec}$ represents the number of correctly reconstructed events and $N_{\rm gen}$ the total number of generated events in signal MC sample. The detection efficiencies have been found to be:

$$\text{SVD1}: \quad \varepsilon(B^{\pm} \to \eta_{\rm c} K^{\pm} \times \eta_{\rm c} \to p\bar{p}) = 0.3333 \pm 0.0012 \tag{3.12}$$
$$\text{SVD2}: \quad \varepsilon(B^{\pm} \to \eta_{\rm c} K^{\pm} \times \eta_{\rm c} \to p\bar{p}) = 0.3812 \pm 0.0012 \tag{3.13}$$

for the charged mode, and:

$$\text{SVD1}: \quad \varepsilon(B^{0} \to \eta_{\rm c} K^{0}_{\rm S} \times \eta_{\rm c} \to p\bar{p}) = 0.2003 \pm 0.0009 \tag{3.14}$$
$$\text{SVD2}: \quad \varepsilon(B^{0} \to \eta_{\rm c} K^{0}_{\rm S} \times \eta_{\rm c} \to p\bar{p}) = 0.2536 \pm 0.0010 \tag{3.15}$$

for the neutral mode. In addition, efficiency correction factors, η ($\tilde{\varepsilon} = \eta.\varepsilon$), have been determined:

$$\text{SVD1}: \quad \eta(B^{\pm} \to \eta_{\rm c} K^{\pm} \times \eta_{\rm c} \to p\bar{p}) = 1.0162 \pm 0.0075 \tag{3.16}$$
$$\text{SVD2}: \quad \eta(B^{\pm} \to \eta_{\rm c} K^{\pm} \times \eta_{\rm c} \to p\bar{p}) = 1.0126 \pm 0.0067 \tag{3.17}$$

for the charged mode, and:

$$\text{SVD1}: \quad \eta(B^{0} \to \eta_{\rm c} K^{0}_{\rm S} \times \eta_{\rm c} \to p\bar{p}) = 0.9891 \pm 0.0056 \pm 0.0060_{\rm syst} \tag{3.18}$$
$$\text{SVD2}: \quad \eta(B^{0} \to \eta_{\rm c} K^{0}_{\rm S} \times \eta_{\rm c} \to p\bar{p}) = 0.9888 \pm 0.0054 \pm 0.0060_{\rm syst} \tag{3.19}$$

for the neutral mode. These correction factors naturally account for the differences between Monte Carlo and experimental data and have been provided as lookup tables for various kinematic regions by independent Belle studies. The main source of the differences arises from the kaon PID [31] for the charged mode and K_S reconstruction [41] for the neutral mode.

3.1.10 Summary

For lucidity, we have summarized all observables together with the fit regions and signal/side-band region in Table 3.7. The selection criteria and veto cuts can be found in Table 3.8.

$M_{\rm bc}$ signal region	$5.271\,{\rm GeV}/c^2 < M_{\rm bc} < 5.290\,{\rm GeV}/c^2$
$M_{\rm bc}$ side-band region	$5.200\,{\rm GeV}/c^2 < M_{\rm bc} < 5.265\,{\rm GeV}/c^2$
ΔE fit region	$-0.1\,{\rm GeV} < \Delta E < +0.1\,{\rm GeV}$
η_c fit region	$2.84\,{\rm GeV}/c^2 < M_{\eta_c} < 3.03\,{\rm GeV}/c^2$
Δt fit region	$\lvert\Delta t\rvert < 70\,{\rm ps}$

Tab. 3.7: Fit regions and signal/side-band region used in the analysis.

Kaons and protons selection criteria	
Impact parameters	$\lvert {\rm d}r\rvert < 0.5\,{\rm cm}$ & $\lvert {\rm d}z\rvert < 3.0\,{\rm cm}$
Kaons PID	$\mathcal{L}_{\rm K/\pi} > 0.6$ & $p(e) < 0.95$
Protons (antiprotons) PID	$\mathcal{L}_{\rm p/K} > 0.4$ & $\mathcal{L}_{\rm p/\pi} > 0.4$ & $p(e) < 0.95$
$K^0_{\rm S}$ mass window	$482\,{\rm MeV}/c^2 < m(\pi^+\pi^-) < 514\,{\rm MeV}/c^2$
Best B candidate selection	
based on $M_{\rm bc}$	
Continuum suppression cuts	
Likelihood ratio	$\mathcal{CS}_{\rm cut} = 0.2$
Veto cuts	
$\overline{\Lambda}_{\rm c}$ veto	$2271\,{\rm MeV} < m(\bar{p}K^0_{\rm S}) < 2301\,{\rm MeV}$
Vertexing and flavour tagging cuts	
#(SVD hits)/charged track	> 1 in $r\phi$-plane & > 2 in z-direction
Single-track vertices	$\delta z < 0.5\,{\rm mm}$
Multi-track vertices	$\delta z < 0.2\,{\rm mm}$ & $\xi^{\rm rec,tag}/{\rm ndf}^{\rm rec,tag} < 50$

Tab. 3.8: Summary of all selection criteria and veto cuts used in this anaysis.

4 Data Model

The branching fractions, $\mathcal{B}$, and CP violating parameters, $\mathcal{S}_{CP}$ and $\mathcal{A}_{CP}$, have been extracted from a 4-dimensional extended unbinned maximum likelihood fit to ΔE, η_c invariant mass, Δt and q. The first three observables have been represented by continuous variables, the charge by a discrete variable, $q = \pm 1$. The fit has been simultaneously performed in each r-bin, $l = 0-6$, and for each SVD configuration: SVD1 and SVD2, further denoted by $s = 1$ and 2, respectively. As the detector response differs for these two detector configurations, the data model has been naturally characterized by two various sets of fit parameters. The only common parameters remained: B lifetime, CP violating parameters, $\mathcal{S}_{CP}$ and $\mathcal{A}_{CP}$, and effective B lifetime describing non-CP violating B background. As a fitting package C++ software based on MINUIT2 [42] has been written and used.

Compared to previous Belle analysis [17], such an approach seems to be significantly more complex. Nevertheless, the main motivation has been, first, to measure the $\mathcal{B}$ more precisely by utilizing all the observed variables in a simultaneous fit. And second, more importantly, to decrease the systematic errors in the measurement of $\mathcal{S}_{CP}$ and $\mathcal{A}_{CP}$ parameters. In the previous analysis, the $\mathcal{B}$, a fraction of signal events, $f = N_{\rm sig}/(N_{\rm sig} + N_{\rm bkg})$, and the signal and background distributions of $M_{\rm bc}$ and ΔE were determined first, in a 2D unbinned ML fit, $\mathcal{P}(\Delta E, M_{\rm bc})$, and afterwards, the CP violating parameters were extracted from a 2-dimensional unbinned ML fit to $(\Delta t \times q)$ with the event-by-event signal probability given as:

$$f_{\rm sig} = \frac{f\mathcal{P}_{\rm sig}(\Delta E, M_{\rm bc})}{f\mathcal{P}_{\rm sig}(\Delta E, M_{\rm bc}) + (1-f)\mathcal{P}_{\rm bkg}(\Delta E, M_{\rm bc})}, \tag{4.1}$$

Due to higher number of fixed parameters from the 2D fit, such a strategy, further denoted as 2D×2D fit, automatically generated extra systematic errors to the final results, which we intend to avoid here.

In this chapter, the data model for the charged and neutral mode of $\eta_{\rm c} \to p\bar{p}$ will be shown. The backward comparison of the new approach with the old one will be demonstrated in Chapter 6.

4.1 Signal Model

The signal shape has been determined from correctly reconstructed signal MC events using the selection criteria described in 3.1. As expected, the study of correlations, ρ, between individual variables has shown that ΔE is highly correlated with η_c invariant mass. ρ has been found to be 20.1 % and 16.5 %, for the charged mode, and 20.6 % and 17.3 %, for the neutral mode, both for SVD1 and SVD2, respectively. Scatter plots of ΔE versus η_c mass are shown for illustration in Fig. 4.1.

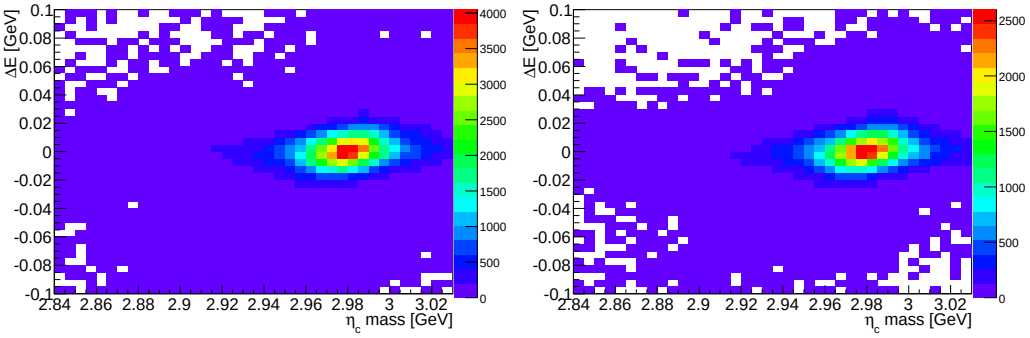

Fig. 4.1: Correlation of ΔE versus η_c invariant mass (scatter plots) for the charged mode (left) and the neutral mode (right).

Further, as the B meson has been reconstructed from the η_c resonance, the number of correctly reconstructed events doesn't have to be necessarily equal. Generally, one expects three different fractions of events: first, $f_{\mathrm{sig}\times\mathrm{sig}}$, with both correctly reconstructed B meson and η_c resonance, second, $f_{\mathrm{sig}\times\mathrm{bkg}}$, with correctly reconstructed B meson but misreconstructed η_c and finally, f_{bkg}, with misreconstructed B independently on the fact whether the η_c has or not been correctly reconstructed. The MC study has shown that the fraction, $f_{\mathrm{sig}\times\mathrm{bkg}}$, can be considered negligible for the studied $\eta_c \to p\bar{p}$ decay. On the other hand, the fraction has been found to be non-zero for η_c decays with the particle of the same type coming from the B meson and the resonance, e.g. $\eta_c \to K^0_S K^{\pm}\pi^{\mp}$ decay. Here, the prompt kaon coming right from the B meson might get swapped with the kaon coming from the η_c and thus, generate still correctly reconstructed B, but misreconstructed η_c resonance.

The PDF for ΔE has been taken as a sum of three Gaussians, naturally incorporating correction for the difference between MC and data via separate calibration factors (offsets). The calibration offset that modifies the mean, $\mu^{\mathrm{CF}}_{\mathrm{main}}$, is fixed to zero, the factor that modifies the sigma, $\sigma^{\mathrm{CF}}_{\mathrm{main}}$, is fixed to

one, for signal model. They are determined from a control sample (charged mode) as detailed in Chapter 6. Due to fit stability, the mean and sigma of tail Gaussians, $\mu^{1,2}_{\text{tail}}$ and $\sigma^{1,2}_{\text{tail}}$, are always expressed with respect to the main mean and sigma, respectively. The PDF follows as:

$$\begin{aligned}\mathcal{P}_{\text{sig}}(\Delta E|m_{\eta_c}) &= f_1.G(\Delta E;\tilde{\mu}_{\text{main}} = \mu_{\text{main}} + \mu^{\text{corr}}_{\text{main}} + \mu^{\text{CF}}_{\text{main}}, \tilde{\sigma}_{\text{main}} = \sigma^{\text{CF}}_{\text{main}}\sigma_{\text{main}}) \\ &+ f_2.G(\Delta E;\tilde{\mu}_{\text{main}} + \mu^{1}_{\text{tail}}, \tilde{\sigma}_{\text{main}}\sigma^{1}_{\text{tail}}) \\ &+ (1 - f_1 - f_2).G(\Delta E;\tilde{\mu}_{\text{main}} + \mu^{2}_{\text{tail}}, \tilde{\sigma}_{\text{main}}\sigma^{2}_{\text{tail}})\end{aligned} \tag{4.2}$$

The correlation between ΔE and η_c mass, m_{η_c}, has been modelled via a linear dependence of the main mean, $\mu^{\text{corr}}_{\text{main}}$, on the m_{η_c}:

$$\mu^{\text{corr}}_{\text{main}} = k_{\text{corr}}(m_{\eta_c} - (M_{\eta_c} + \mu^{\text{Voigt}})), \tag{4.3}$$

where k_{corr} represents the linear dependence, $M_{\eta c}$ the generator value of η_c mass and μ^{Voigt} has been obtained from the η_c mass fit; see Eq. (4.4).

The PDF for m_{η_c} has been expressed as a convolution of Breit-Wigner function, BW, and a central double Gaussian, or in other words, as a sum of two Voigt functions:

$$\begin{aligned}\mathcal{P}_{\text{sig}}(m_{\eta_c}) &= f.\big(BW(m_{\eta_c};M_{\eta_c},\Gamma_{\eta_c}) \otimes G(m_{\eta_c};\mu^{\text{Voigt}}, \tilde{\sigma}^{\text{Voigt}}_{\text{main}} = \sigma^{\text{CF Voigt}}_{\text{main}}\sigma^{\text{Voigt}}_{\text{main}})\big) \\ &+ (1 - f).\big(BW(m_{\eta_c};M_{\eta_c},\Gamma_{\eta_c}) \otimes G(m_{\eta_c};\mu^{\text{Voigt}}, \tilde{\sigma}^{\text{Voigt}}_{\text{main}}\sigma^{\text{Voigt}}_{\text{tail}})\big),\end{aligned} \tag{4.4}$$

where M_{η_c} and Γ_{η_c} are the generator values of η_c mass and width, respectively.

As for the calibration factors (offsets), the difference between MC and data is for Breit-Wigner function automatically taken into account by using different values of M_{η_c} and Γ_{η_c}; generator values for MC, PDG values for data. For illustration, the values have been summarized in Table 4.1. Concerning

	Generator value	**PDG value** [16]
M_{η_c} [GeV]	2.9798	2.9803
Γ_{η_c} [GeV]	0.0265	0.0286

Tab. 4.1: η_c mass and width used in MC (second column) and data fit (third column).

detector effects, the main sigma of resolution function has been corrected using an additional correction factor, $\sigma^{\text{CF Voigt}}_{\text{main}}$, set to one here. As the mean

value already represents a shift with respect to the corresponding M_{η_c}, either generator or PDG value, it is expected to be the same for MC and data. No extra offset has been implemented here.

For overall numerical stability the ROOT implementation of Voigt function has been used [43].

Based on Equation (1.1), the 2D PDF of $(\Delta t \times q)$ is given by:

$$\begin{aligned}\mathcal{P}^l_{\rm sig}(\Delta t, q) \; &= (1-f_{\rm ol})\frac{e^{-|\Delta t|/\tau_{\rm B}}}{4\tau_{\rm B}}\Big\{(1-q.\Delta w_l) + \\ &\quad q(1-2w_l)\times\Big[\mathcal{S}_{CP}\sin(\Delta m_{\rm d}\Delta t) + \mathcal{A}_{CP}\cos(\Delta m_{\rm d}\Delta t)\Big]\Big\}\otimes \\ &\quad \mathcal{R}_{B\bar{B}}(\Delta t) \quad + \quad f_{\rm ol}\frac{1}{2}G(0,\sigma_{\rm ol}),\end{aligned} \tag{4.5}$$

where the meaning of parameters accounting for incorrect flavour tagging, w_l and Δw_l, is in detail described in Section 3.1.8. Their values, directly used in the fit, are summarized in Table 3.6.

The PDF is convolved with a Δt resolution function for B particles, $\mathcal{R}_{B\bar{B}}(\Delta t)$, which consists of three different components: detector resolution mainly due to tracking uncertainty for reconstructed $B_{\rm rec}$ and $B_{\rm tag}$; smearing on $B_{\rm tag}$ vertices due to non-primary tracks and finally; smearing due to the kinematic approximation. In addition, to account for a small number of events that add extra large Δt to the distribution a fraction of outliers, $f_{\rm ol}$, has been introduced. The brief overview of time resolution function together with the summary of parameters used in the analysis are given in Appendix B, more details can be found in [37].

In order to extract the signal shape for both charged and neutral mode, the total signal PDF becomes:

$$\mathcal{P}^l_{\rm sig}(\Delta E, \eta_{\rm c}, \Delta t, q) = \mathcal{P}_{\rm sig}(\Delta E|m_{\eta_{\rm c}})\mathcal{P}_{\rm sig}(m_{\eta_{\rm c}})\mathcal{P}^l_{\rm sig}(\Delta t, q), \tag{4.6}$$

whose shape has been determined with the following extended log-likelihood:

$$\log\mathcal{L}_j = -\sum_{s=1}^{2}\sum_{l=0}^{6}N^s_j f^{l,s}_j \eta^{l,s}_j + \sum_{s=1}^{2}\sum_{i=1}^{\tilde{N}^s_j}\log\left(\sum_{l=0}^{6}N^s_j f^{l,s}_j \eta^{l,s}_j \mathcal{P}^l_j(\Delta E^i, \eta^i_{\rm c}, \Delta t^i, q^i)\right) \tag{4.7}$$

where the sum runs over i events, l flavour bins and s detector configurations. The index j simply represents which log-likelihood component is meant. In this case, j is equal to sig as it represents the signal component here. The parameter N^s is the signal yield, with separate value for SVD1 and SVD2, $f^{l,s}$

the fraction of events in r-bin l and SVD configuration s, and $\eta^{l,s}$ is a correction factor to the r-bin fraction accounting for the difference between MC and data. This correction has been determined from the control sample as detailed in Chapter 6. The value is set to one for signal model.

Since the quality-of-fit test is not automatically generated in ML method (compared, for example, to least-squares method), an ad hoc χ^2/ndf has been artificially constructed for each fit. The final 4D-dimensional distribution has been binned, with a bin size equal to rough estimate of detector resolution ($\sim 5\,\mathrm{MeV}$ for ΔE and η_c mass, $\sim 0.5\,\mathrm{ps}$ for Δt) and then, the goodness-of-fit test, χ^2, has been calculated as follows:

$$\chi^2 = \sum_{i=0}^{N_{\mathrm{bins}}} \frac{(N_i^{\mathrm{Data}} - N_i^{\mathrm{PDF}})^2}{N_i^{\mathrm{Data}}} \tag{4.8}$$

Here, N^{Data} is the number of events in a given bin i. N^{PDF} represents the central bin value returned for the same bin from the fitted PDF. The number of degrees of freedom, ndf, is calculated as the total number of bins minus the number of fitted parameters.

In addition to quality-of-fit test a pull distribution has been constructed and plotted. It clearly shows possible inconsistency of the fit compared to experimental data, all expressed in terms of standard deviation. The pull distribution (pull value in bin i) has been defined as:

$$\mathrm{pull}_i = \frac{N_i^{\mathrm{Data}} - N_i^{\mathrm{PDF}}}{\sqrt{N_i^{\mathrm{Data}}}}, \tag{4.9}$$

where the individual variables have the same meaning as in χ^2 definition.

For the charged mode, the fit results of correctly reconstructed signal Monte Carlo, together with pull distributions, are shown in Figures 4.2 and 4.3 for SVD1 and SVD2 configuration, respectively. The results of the neutral mode are depicted in Figures 4.4 and 4.5. The fitted values of $\mathcal{S}_{CP}$, $\mathcal{A}_{CP}$ and B lifetime, τ_B, have been summarized in corresponding Tables 4.2, 4.3, 4.4 and 4.5, and compared to input values used in the generator to cross-check if any reconstruction bias is present. All values have been found to be consistent within $\pm 3\sigma$, no obvious bias has been observed. Obtained fit parameters are summarized in Appendix C.

4.2 Background Model

In most analyses the background shape has to be separately modelled for continuum and $B\bar{B}$ component. Here, the observed $B\bar{B}$ peaking background

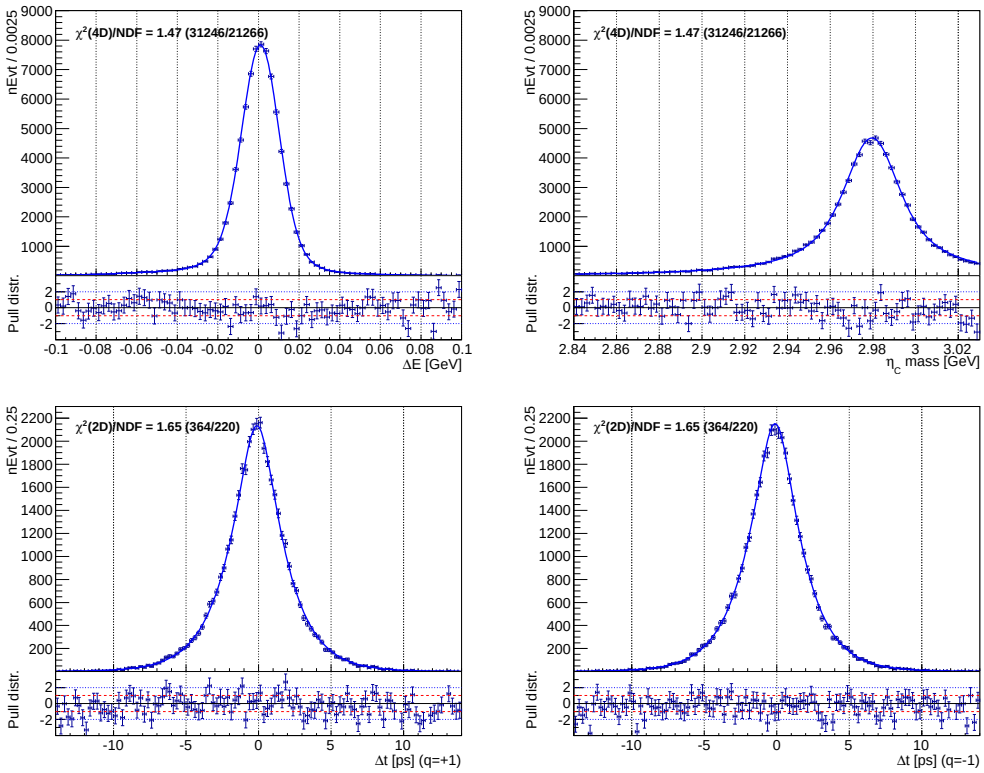

Fig. 4.2: Fit projections of correctly reconstructed B mesons obtained from the signal MC studies for **SVD1** experiment in the **charged** mode, $B^{\pm} \to \eta_c K^{\pm}$, $\eta_c \to p\bar{p}$. The individual projections are: ΔE (top left), η_c invariant mass (top right), Δt for B tagged with $q = +1$ (down left) and Δt for B tagged with $q = -1$ (down right).

	Gen. value	**Reconstr. value**	**Bias** $[\sigma]$
τ [ps]	1.6545	1.649 ± 0.007	-0.8σ
$\mathcal{S}_{\mathcal{CP}}$	0.0	0.013 ± 0.010	$+1.3\sigma$
$\mathcal{A}_{\mathcal{CP}}$	0.0	-0.011 ± 0.007	-1.6σ

Tab. 4.2: Fit results, lifetime and CP violation parameters, and their cross-check with the generated values for the **charged** mode (**SVD1** experiment). The last column shows the discrepancy between the input (generated) value and the output (reconstructed) value, expressed in terms of one standard deviation.

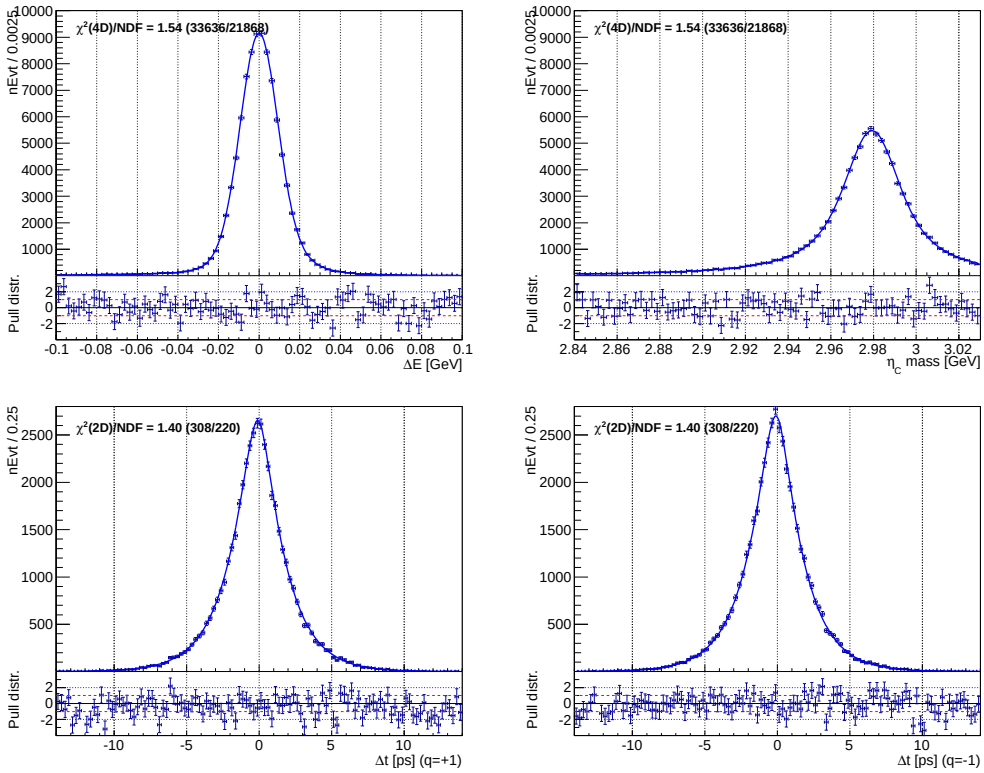

Fig. 4.3: Fit projections of correctly reconstructed B mesons obtained from the signal MC studies for **SVD2** experiment in the **charged** mode, $B^{\pm} \to \eta_c K^{\pm}$, $\eta_c \to p\bar{p}$. The individual projections are: ΔE (top left), η_c invariant mass (top right), Δt for B tagged with $q = +1$ (down left) and Δt for B tagged with $q = -1$ (down right).

	Gen. value	**Reconstr. value**	**Bias** $[\sigma]$
τ [ps]	1.6545	1.658 ± 0.006	$+0.6\sigma$
$\mathcal{S}_{\mathcal{CP}}$	0.0	0.0004 ± 0.0090	$+0.04\sigma$
$\mathcal{A}_{\mathcal{CP}}$	0.0	-0.006 ± 0.006	-1.0σ

Tab. 4.3: Fit results, lifetime and CP violation parameters, and their cross-check with the generated values for the **charged** mode (**SVD2** experiment). The last column shows the discrepancy between the input (generated) value and the output (reconstructed) value, expressed in terms of one standard deviation.

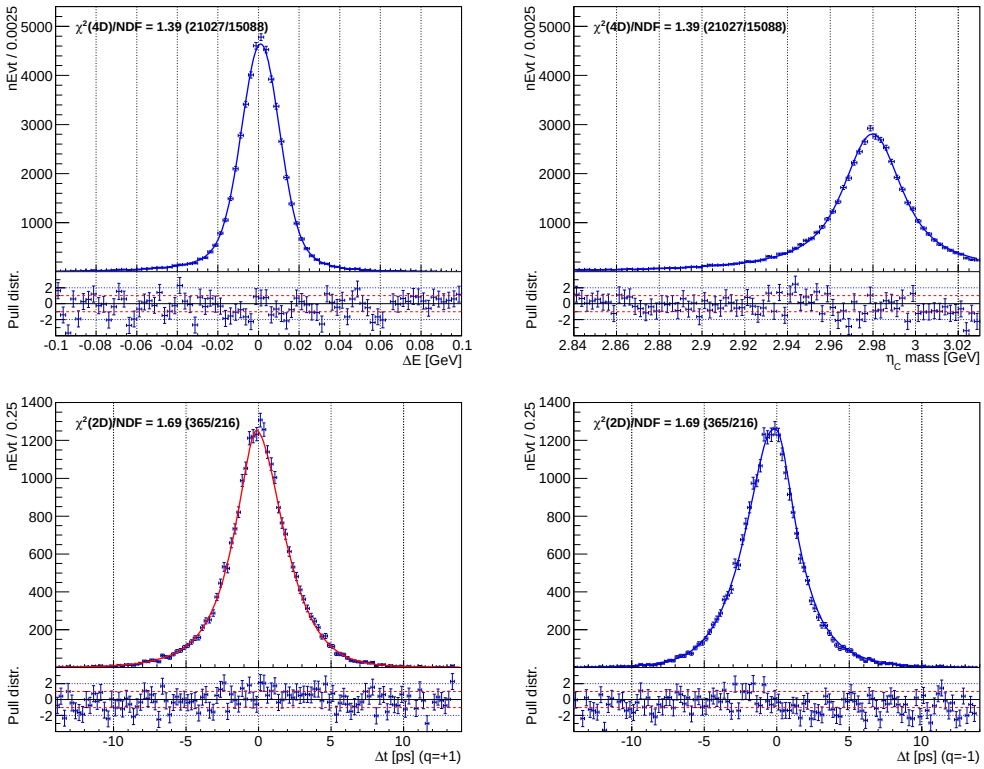

Fig. 4.4: Fit projections of correctly reconstructed B mesons obtained from the signal MC studies for **SVD1** experiment in the **neutral** mode, $B^0 \to \eta_c K_S$, $\eta_c \to p\bar{p}$. The individual projections are: ΔE (top left), η_c invariant mass (top right), Δt for B tagged with $q = +1$ (down left) and Δt for B tagged with $q = -1$ (down right).

	Gen. value	**Reconstr. value**	**Bias** $[\sigma]$
τ [ps]	1.5344	1.529 ± 0.009	-0.6σ
$\mathcal{S}_{\mathcal{CP}}$	0.6889	0.679 ± 0.020	-0.5σ
$\mathcal{A}_{\mathcal{CP}}$	0.0	-0.033 ± 0.013	-2.5σ

Tab. 4.4: Fit results, lifetime and CP violation parameters, and their cross-check with the generated values for the **neutral** mode (**SVD1** experiment). The last column shows the discrepancy between the input (generated) value and the output (reconstructed) value, expressed in terms of one standard deviation.

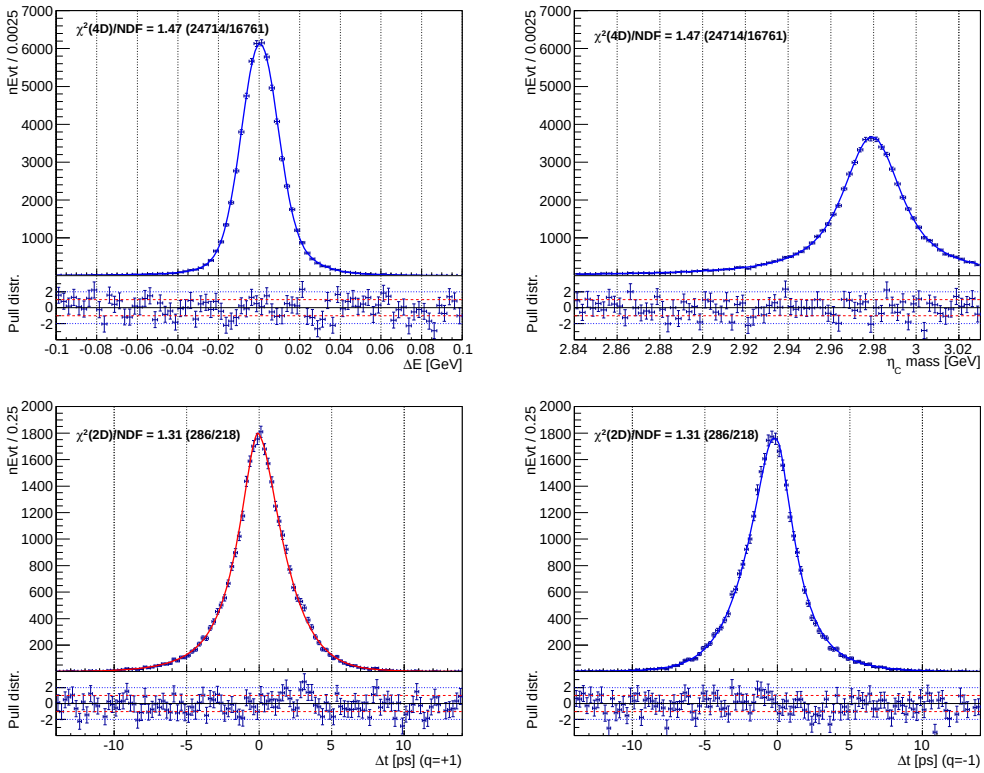

Fig. 4.5: Fit projections of correctly reconstructed B mesons obtained from the signal MC studies for **SVD2** experiment in the **neutral** mode, $B^0 \to \eta_c K_S$, $\eta_c \to p\bar{p}$. The individual projections are: ΔE (top left), η_c invariant mass (top right), Δt for B tagged with $q = +1$ (down left) and Δt for B tagged with $q = -1$ (down right).

	Gen. value	**Reconstr. value**	**Bias** $[\sigma]$
τ [ps]	1.5344	1.534 ± 0.007	-0.06σ
$\mathcal{S}_{\mathcal{CP}}$	0.6889	0.667 ± 0.015	-1.5σ
$\mathcal{A}_{\mathcal{CP}}$	0.0	0.005 ± 0.011	$+0.5\sigma$

Tab. 4.5: Fit results, lifetime and CP violation parameters, and their cross-check with the generated values for the **neutral** mode (**SVD2** experiment). The last column shows the discrepancy between the input (generated) value and the output (reconstructed) value, expressed in terms of one standard deviation.

in ΔE distribution has been fully suppressed by applied veto cut, as shown in Fig. 3.8, and according to the generic MC studies, the background PDF exhibits only a linear dependence in ΔE and η_c invariant mass in both components, continuum and $B\bar{B}$. The same shape has been observed and cross-checked with the side-band data. Thus, the ΔE and η_c background distributions have been modelled with the sum of Chebyshev polynomials up to the 1st order:

$$\mathcal{P}_{\rm bkg}(\Delta E) = \mathcal{N}\big(1 + c_1 C_1(\Delta E)\big) \quad (4.10)$$

$$\mathcal{P}_{\rm bkg}(m_{\eta_c}) = \mathcal{N}\big(1 + c_1 C_1(m_{\eta_c})\big) \quad (4.11)$$

On the other hand, the Δt distribution exhibits different behavior for $B\bar{B}$ background (non-CP violating B background) compared to continuum. The $B\bar{B}$ background has been studied using η_c-inclusive MC sample and the contribution of expected Δt peaking background has been estimated to be $\sim 2\,\%$ for the neutral mode and $\sim 9\,\%$ for the charged mode. As for the neutral mode, such a level of Δt peaking background is found to be much lower than the expected statistical error of the yield and thus, the contribution can be safely neglected. In contrast, for the charged mode, such a peaking background represents a significant contribution and its shape has been described by a following PDF:

$$\mathcal{P}^{B\bar{B}}_{\rm bkg}(\Delta t, q) = \frac{e^{-|\Delta t|}/\tau_{\rm eff}}{2\tau_{\rm eff}} \otimes \mathcal{R}_{B\bar{B}}(\Delta t), \quad (4.12)$$

Similarly as for the signal (4.5), the exponential PDF is convolved with the Δt resolution function for B particles, $\mathcal{R}_{B\bar{B}}(\Delta t)$. Since reconstructed $B\bar{B}$ events may borrow a particle from the tag side, the average Δt lifetime tends to be smaller, which is taken into account with a so-called effective lifetime. The fit results of 10 streams of generic MC data have been depicted in Figure 4.6 and Figure 4.7, the obtained effective lifetime has been found: $\tau^{\rm eff}_{B^\pm} = (1.468 \pm 0.095)\,{\rm ps}$.

The continuum source of Δt background has been parametrized with a distribution consisting of two components, "prompt" and "lifetime" component. The former models the Δt shape for charmless contribution, where all tracks more or less originate from the same vertex point. (The reason is that any intermediate resonance state with charmless content decays instantaneously.) The latter stands for charm contribution, which contains mesons with non-negligible decay time. The prompt component has been described by Dirac delta function, the lifetime component by exponential behavior with an effective lifetime, $\tau_{\rm bkg}$:

$$\mathcal{P}^{q\bar{q}}_{\rm bkg}(\Delta t, q) = \left\{ f_\delta \delta(\Delta t - \mu_\delta) + (1 - f_\delta) \frac{e^{-|\Delta t|}/\tau_{\rm bkg}}{2\tau_{\rm bkg}} \right\} \otimes \mathcal{R}_{q\bar{q}}(\Delta t), \quad (4.13)$$

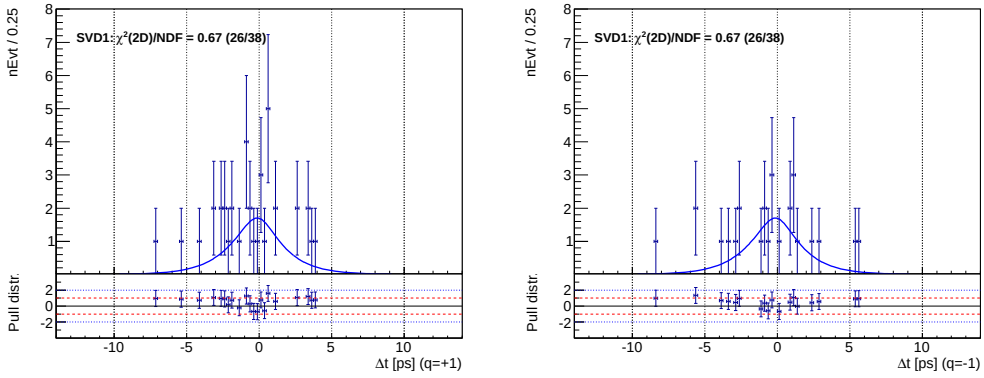

Fig. 4.6: Fit projections to Δt of non-CP violating B background, for B tagged with $q = +1$ (left) and $q = -1$ (right), obtained from the generic MC sample for **SVD1** experiment in the **charged** mode.

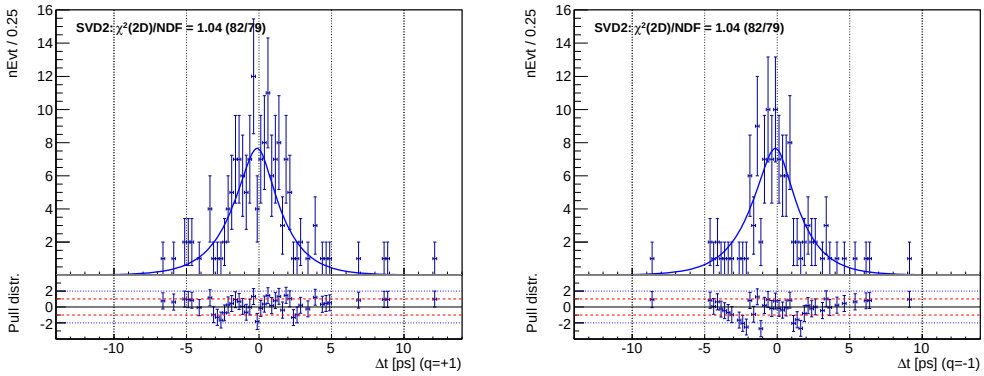

Fig. 4.7: Fit projections to Δt of non-CP violating B background, for B tagged with $q = +1$ (left) and $q = -1$ (right), obtained from the generic MC sample for **SVD2** experiment in the **charged** mode.

where f_δ stands for a fraction and μ_δ for the mean of prompt component. Moreover, to account for the effects of detector resolution, the PDF has been convolved with a background resolution function, represented by the sum of two Gaussians:

$$\mathcal{R}_{q\bar{q}}(\Delta t) = (1 - f_{\rm bkg}^{\rm tail})G(\Delta t; \mu_{\rm bkg}, s_{\rm bkg}^{\rm main}\sigma_{\rm vtx}) + f_{\rm bkg}^{\rm tail}G(\Delta t; \mu_{\rm bkg}, s_{\rm bkg}^{\rm tail}s_{\rm bkg}^{\rm main}\sigma_{\rm vtx}), \tag{4.14}$$

where $\sigma_{\rm vtx}$ is the event-by-event error, $\sqrt{\sigma_{\rm rec}^2 + \sigma_{\rm tag}^2}/\beta\gamma c$, with $\sigma_{\rm rec}$ and $\sigma_{\rm tag}$ being the vertex errors of CP reconstructed and tagged B, respectively. Fraction of tails is represented by $f_{\rm bkg}^{\rm tail}$ and two Gaussian widths: $s_{\rm bkg}^{\rm main}\sigma_{\rm vtx}$ and $s_{\rm bkg}^{\rm tail}s_{\rm bkg}^{\rm main}\sigma_{\rm vtx}$. In order to achieve higher precision in fitting, usually two sets of Gaussian parameters: $\mu_{\rm bkg}$, $s_{\rm bkg}^{\rm main}$ and $s_{\rm bkg}^{\rm tail}$, and corresponding fraction of tails, $f_{\rm bkg}^{\rm tail}$, are used; one for single-track vertices (with only one charged track used for vertex reconstruction, either for $B_{\rm rec}$ or $B_{\rm tag}$), the other for multi-track vertices (with more than just one charged track used in vertex reconstruction).

Similarly as for the signal component (4.5), each Δt background PDF also takes into account the effect of outliers (1/2 stands for the normalization over the B charge, q):

$$\tilde{\mathcal{P}}_{\rm bkg}^{q\bar{q}/B\bar{B}}(\Delta t, q) = \frac{1}{2}(1-f_{\rm ol})\mathcal{P}_{\rm bkg}^{q\bar{q}/B\bar{B}}(\Delta t, q)\otimes\mathcal{R}_{q\bar{q}/B\bar{B}}(\Delta t)+\frac{1}{2}f_{\rm ol}G(0,\sigma_{\rm ol}) \tag{4.15}$$

The respective contribution of each component, continuum and $B\bar{B}$, is represented by a fraction, $f_{\rm bkg}^{\Delta t}$, obtained from the final fit to data:

$$\tilde{\mathcal{P}}_{\rm bkg}(\Delta t, q) = f_{\rm bkg}^{\Delta t}\tilde{\mathcal{P}}_{\rm bkg}^{q\bar{q}}(\Delta t, q) + (1 - f_{\rm bkg}^{\Delta t})\tilde{\mathcal{P}}_{\rm bkg}^{B\bar{B}}(\Delta t, q) \tag{4.16}$$

Finally, the total background PDF has been given as a product of the three components:

$$\mathcal{P}_{\rm bkg}(\Delta E, \eta_{\rm c}, \Delta t, q) = \mathcal{P}_{\rm bkg}(\Delta E)\mathcal{P}_{\rm bkg}(m_{\eta_{\rm c}})\tilde{\mathcal{P}}_{\rm bkg}(\Delta t, q). \tag{4.17}$$

and the log-likelihood follows as:

$$\log\mathcal{L}_j = -\sum_{s=1}^{2}\sum_{l=0}^{6}N_j^s f_j^{l,s} + \sum_{s=1}^{2}\sum_{i=1}^{\tilde{N}_j^s}\log\left(\sum_{l=0}^{6}N_j^s f_j^{l,s}\mathcal{P}_j^l(\Delta E^i, \eta_{\rm c}^i, \Delta t^i, q^i)\right), \tag{4.18}$$

with the same meaning of individual parameters as in Equation (4.7), except for the fact that j equals to bkg and no correction factors for the difference between MC and data are needed here.

Concerning the continuum fit results, since the $(\Delta t \times q)$ background peaks below the signal, the shape of $\tilde{\mathcal{P}}^{q\bar{q}}_{\rm bkg}(\Delta t, q)$ has been found from the side-band data. Moreover, as the continuum contribution in $(\Delta E \times \eta_{\rm c})$ to the background dominates in the neutral mode, together with the $\tilde{\mathcal{P}}^{q\bar{q}}_{\rm bkg}(\Delta t, q)$ the shape of $\mathcal{P}_{\rm bkg}(\Delta E, \eta_{\rm c})$ could be determined from the side-band data too. In the charged mode for both SVD1 and SVD2 experiments and in the neutral mode for SVD2 only, two various sets of Gaussian parameters and tail fraction: $\mu_{\rm bkg}$, $s^{\rm main}_{\rm bkg}$, $s^{\rm tail}_{\rm bkg}$ and $f^{\rm tail}_{\rm bkg}$ have been used in $\mathcal{R}_{q\bar{q}}(\Delta t)$. In contrast, for SVD1 experiment in the neutral mode, only one set of such parameters could be practically used due to very limited size of side-band data sample. The background shapes are for illustration shown in Figures 4.8 and 4.9 for the charged mode and SVD1 and SVD2 experiments, respectively. For the same in the neutral mode, see Figures 4.10 and 4.11. The values of individual $(\Delta t \times q)$ fit parameters are listed in corresponding Tables 4.6,4.7, 4.8 and 4.9. All obtained parameters are summarized in Appendix C.

In addition, the size of control data sample (charged mode) has been found to be high enough to extract the background shape parameters of ΔE and $\eta_{\rm c}$ mass directly from the final fit together with the signal, background yields and CP violating parameters, while keeping the $\tilde{\mathcal{P}}^{q\bar{q}/B\bar{B}}_{\rm bkg}(\Delta t, q)$ parameters fixed. In the neutral mode, such an approach has not been adopted due to fit instability. Therefore, the whole background shape remains fixed from the side-band data and only signal, background yields and CP violating parameters will be extracted there. Moreover, the background contribution from the non-CP violating B background has been found negligible as mentioned earlier and thus, fixing background parameters just from the side-band data in the neutral mode is considered as a consistent approach.

4.3 Total PDF and Expected Yields

The total log-likelihood for 264 candidates (126 with $q = +1$, 138 with $q = -1$) in the neutral mode and 1523 candidates (754 with $q = +1$, 769 with $q = -1$) in the charged mode has been calculated as the sum of $\log(\mathcal{L}_{\rm sig})$, Eq. (4.7), and $\log(\mathcal{L}_{\rm bkg})$, Eq. (4.18).

In the neutral mode, only the yields (signal, background, both in SVD1 and SVD2) and $\mathcal{A}_{CP}$, $\mathcal{S}_{CP}$ parameters have been considered as free, the rest has been fixed from signal MC studies (signal component), side-band data (continuum background component) and control sample (correction factors and offsets). The physics parameters $\tau_{\rm B}$, $M_{\eta_{\rm c}}$ and $\Gamma_{\eta_{\rm c}}$ have been fixed from the PDG, see Table 4.1.

In the charged mode, much higher statistics is available. Therefore, not

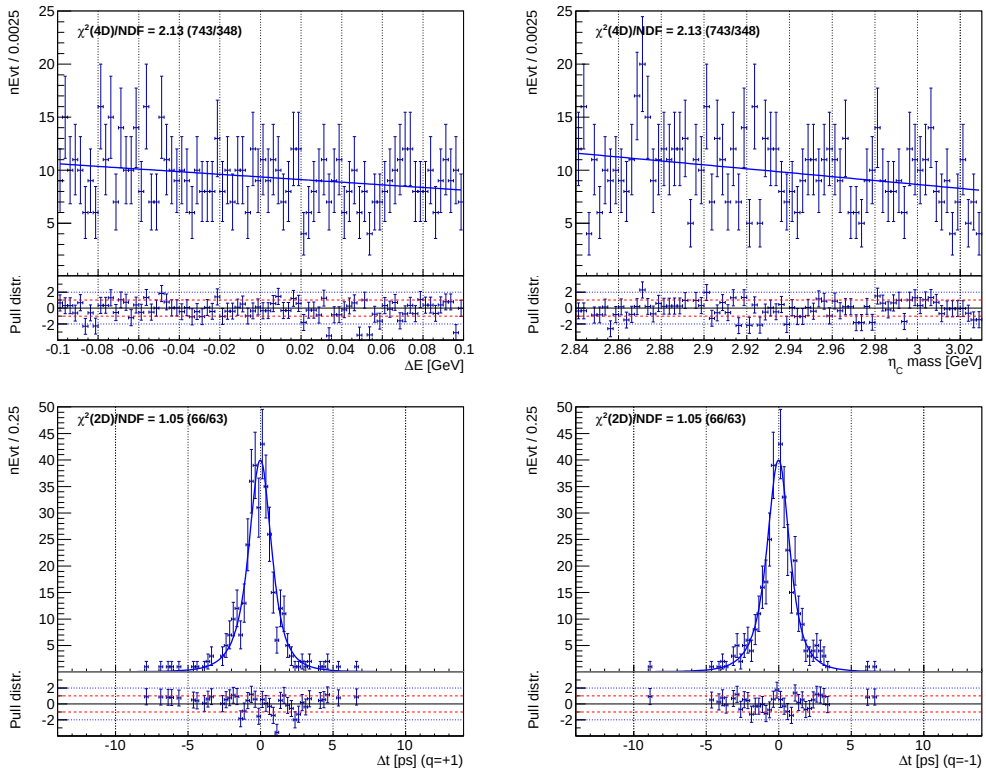

Fig. 4.8: Fit projections of background shape obtained from the side-band data for **SVD1** experiment in $B^{\pm} \to \eta_c K^{\pm}$, $\eta_c \to p\bar{p}$. The individual projections are: ΔE (top left), η_c invariant mass (top right), Δt for B tagged with $q = +1$ (down left) and Δt for B tagged with $q = -1$ (down right).

Parameter	**Fit Result**
τ_{bkg} [ps]	$+0.903 \pm 0.176$
f_{δ}	$+0.635 \pm 0.129$
μ_{δ}	$+0.010 \pm 0.064$
$f^{\text{tail}}_{\text{bkg sngl}}$	$+0.012 \pm 0.007$
$\mu_{\text{bkg sngl}}$	-0.162 ± 0.161
$s^{\text{main}}_{\text{bkg sngl}}$	$+1.20 \pm 0.10$
$s^{\text{tail}}_{\text{bkg sngl}}$	$+12.51 \pm 4.02$
$f^{\text{tail}}_{\text{bkg mult}}$	$+0.562 \pm 0.337$
$\mu_{\text{bkg mult}}$	-0.494 ± 0.424
$s^{\text{main}}_{\text{bkg mult}}$	$+0.689 \pm 0.324$
$s^{\text{tail}}_{\text{bkg mult}}$	$+2.23 \pm 0.78$

Tab. 4.6: $B^{\pm} \to \eta_c K^{\pm}$, $\eta_c \to p\bar{p}$ fit results obtained from the side-band data in **SVD1** experiment.

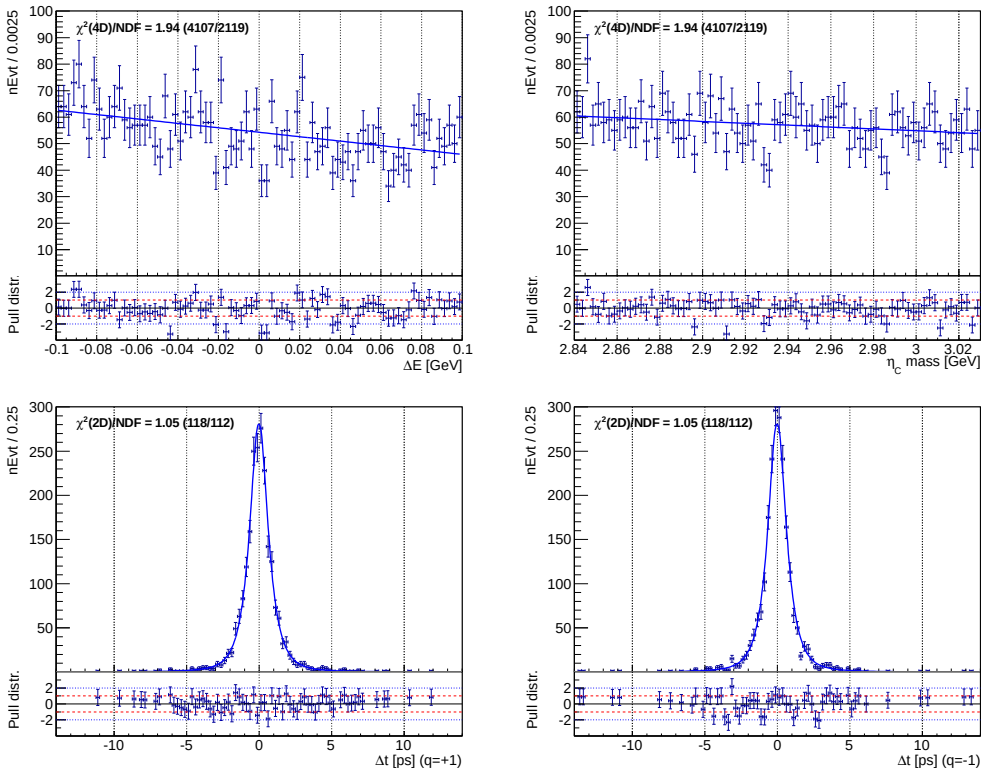

Fig. 4.9: Fit projections of background shape obtained from the side-band data for **SVD2** experiment in $B^{\pm} \to \eta_c K^{\pm}$, $\eta_c \to p\bar{p}$. The individual projections are: ΔE (top left), η_c invariant mass (top right), Δt for B tagged with $q = +1$ (down left) and Δt for B tagged with $q = -1$ (down right).

Parameter	**Fit Result**
τ_{bkg} [ps]	$+0.546 \pm 0.067$
f_{δ}	$+0.390 \pm 0.087$
μ_{δ}	-0.013 ± 0.036
$f^{\text{tail}}_{\text{bkg sngl}}$	$+0.070 \pm 0.018$
$\mu_{\text{bkg sngl}}$	-0.013 ± 0.035
$s^{\text{main}}_{\text{bkg sngl}}$	$+1.22 \pm 0.05$
$s^{\text{tail}}_{\text{bkg sngl}}$	$+5.64 \pm 0.66$
$f^{\text{tail}}_{\text{bkg mult}}$	$+0.182 \pm 0.086$
$\mu_{\text{bkg mult}}$	-0.044 ± 0.095
$s^{\text{main}}_{\text{bkg mult}}$	$+1.08 \pm 0.10$
$s^{\text{tail}}_{\text{bkg mult}}$	$+2.62 \pm 0.43$

Tab. 4.7: $B^{\pm} \to \eta_c K^{\pm}$, $\eta_c \to p\bar{p}$ fit results obtained from the side-band data in **SVD2** experiment.

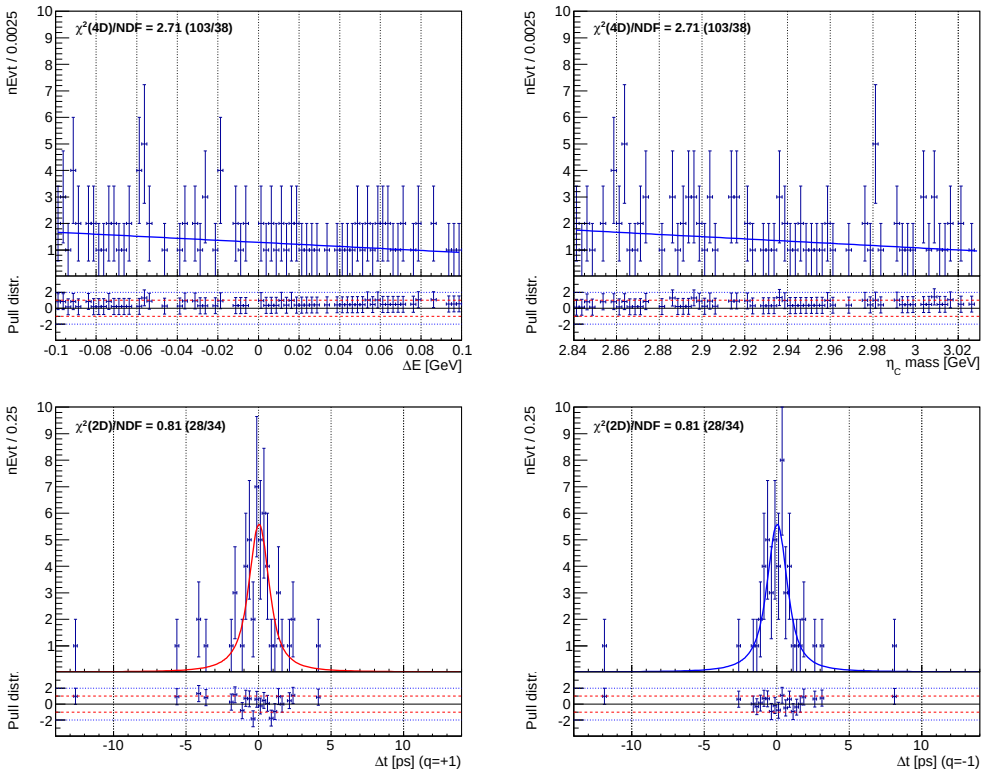

Fig. 4.10: Fit projections of background shape obtained from the side-band data for **SVD1** experiment in $B^0 \to \eta_c K^0_S$, $\eta_c \to p\bar{p}$. The individual projections are: ΔE (top left), η_c invariant mass (top right), Δt for B tagged with $q = +1$ (down left) and Δt for B tagged with $q = -1$ (down right).

Parameter	**Fit Result**
τ_{bkg} [ps]	$+1.03 \pm 0.67$
f_δ	$+0.721 \pm 0.230$
μ_δ	$+0.047 \pm 0.131$
$f^{\text{tail}}_{\text{bkg}}$	$+0.079 \pm 0.057$
μ_{bkg}	-0.099 ± 0.543
$s^{\text{main}}_{\text{bkg}}$	$+0.913 \pm 0.145$
$s^{\text{tail}}_{\text{bkg}}$	$+8.67 \pm 4.14$

Tab. 4.8: $B^0 \to \eta_c K^0_S$, $\eta_c \to p\bar{p}$ fit results obtained from the side-band data in **SVD1** experiment.

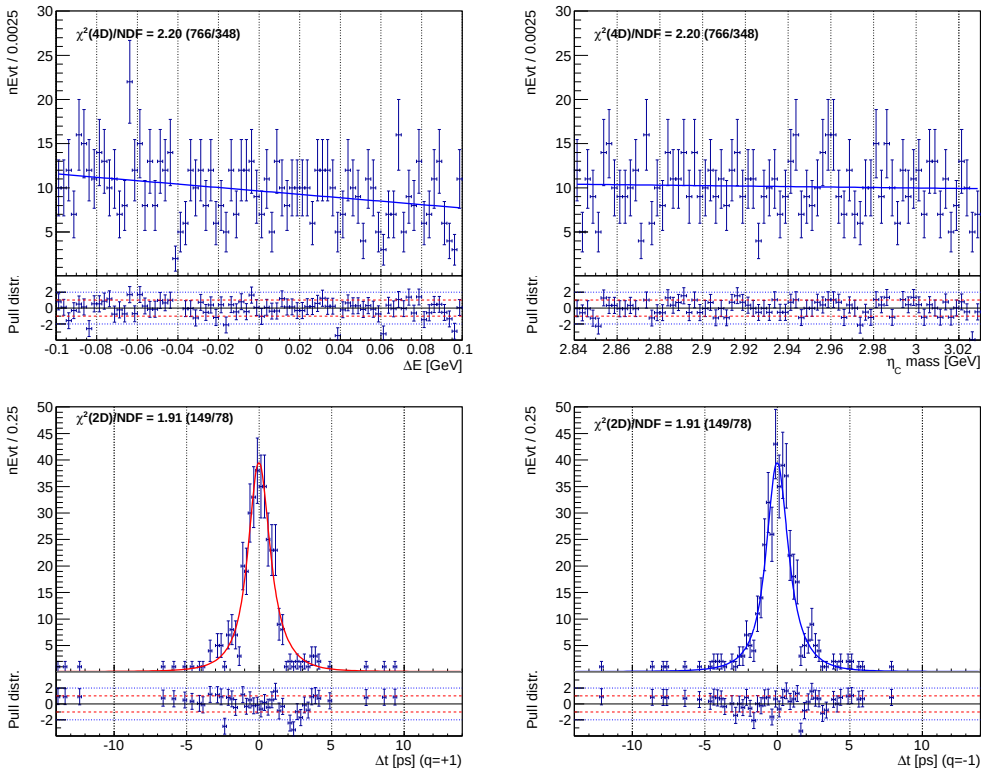

Fig. 4.11: Fit projections of background shape obtained from the side-band data for **SVD2** experiment in the **neutral** mode, $B^0 \to \eta_c K^0_S$, $\eta_c \to p\bar{p}$. The individual projections are: ΔE (top left), η_c invariant mass (top right), Δt for B tagged with $q = +1$ (down left) and Δt for B tagged with $q = -1$ (down right).

Parameter	**Fit Result**
τ_{bkg} [ps]	$+1.02 \pm 0.18$
f_δ	$+0.605 \pm 0.122$
μ_δ	-0.030 ± 0.060
$f^{\text{tail}}_{\text{bkg sngl}}$	$+0.016 \pm 0.008$
$\mu_{\text{bkg sngl}}$	$+0.253 \pm 0.180$
$s^{\text{main}}_{\text{bkg sngl}}$	$+1.35 \pm 0.11$
$s^{\text{tail}}_{\text{bkg sngl}}$	$+15.65 \pm 4.74$
$f^{\text{tail}}_{\text{bkg mult}}$	$+0.137 \pm 0.039$
$\mu_{\text{bkg mult}}$	-0.419 ± 0.428
$s^{\text{main}}_{\text{bkg mult}}$	$+1.25 \pm 0.12$
$s^{\text{tail}}_{\text{bkg mult}}$	$+9.33 \pm 2.31$

Tab. 4.9: $B^0 \to \eta_c K^0_S$, $\eta_c \to p\bar{p}$ fit results obtained from the side-band data in **SVD2** experiment.

only yields and CP violating parameters, but also the background shape of ΔE, η_c mass, correction factors (offsets) and fraction of Δt peaking background in continuum versus non-CP violating B background have been determined directly from data. The signal component has been fixed from signal MC studies, continuum peaking background in Δt together with background r-bin fractions from side-band data and non-CP violating B background from generic MC sample. Similarly as in the neutral mode, the lifetime has been fixed to the most up-to-date PDG values [18]. In general, when measuring CP violating parameters, the lifetime can't be determined so precisely. The values used and fixed in both charged and neutral mode fitter are given here:

$$\tau_{B^\pm} = 1.641\,\text{ps} \tag{4.19}$$
$$\tau_{B^0} = 1.519\,\text{ps} \tag{4.20}$$

Expected signal and background yields have been estimated based on the following relations:

$$N_{\text{sig}} = N_{\text{B}\bar{\text{B}}} \times \mathcal{B}_{\text{PDG}} \times \varepsilon \tag{4.21}$$
$$N_{\text{bkg}} = N_{\text{tot}} - N_{\text{sig}}, \tag{4.22}$$

where $N_{\text{B}\bar{\text{B}}}$ represents the total number of Belle $B\bar{B}$ events, summarized in Table 2.1, ε the detection efficiencies, see Section 3.1.9, and $\mathcal{B}_{\text{PDG}}$ the branching ratios: (5.785×10^{-7}) for $B^0 \to \eta_c K^0_S$, $\eta_c \to p\bar{p}$, and (11.83×10^{-7}) for $B^\pm \to \eta_c K^\pm$, $\eta_c \to p\bar{p}$ [16]. Estimated yields have been summarized in Table 4.10 for the charged mode and 4.11 for the neutral mode.

Charged mode	**Yield**
$N_{\text{sig}}^{\text{SVD1}}$	(59.92 ± 7.74)
$N_{\text{bkg}}^{\text{SVD1}}$	(187.08 ± 13.68)
$N_{\text{sig}}^{\text{SVD2}}$	(279.42 ± 16.72)
$N_{\text{bkg}}^{\text{SVD2}}$	(996.58 ± 31.57)

Tab. 4.10: Expected signal and background yields for the **charged** mode.

Neutral mode	**Yield**
$N_{\text{sig}}^{\text{SVD1}}$	(17.61 ± 4.20)
$N_{\text{bkg}}^{\text{SVD1}}$	(24.39 ± 4.94)
$N_{\text{sig}}^{\text{SVD2}}$	(90.90 ± 9.53)
$N_{\text{bkg}}^{\text{SVD2}}$	(131.10 ± 11.45)

Tab. 4.11: Expected signal and background yields for the **neutral** mode.

5 Validity Study

The validity study of the overall 4D fit procedure in the neutral mode, together with a search for possible fit bias and an estimation of expected statistical error, will be for $\mathcal{S}_{CP}$, $\mathcal{A}_{CP}$ parameters and branching ratio, $\mathcal{B}$, presented and discussed in detail here.

5.1 Toy MC Simulation

In order to check the fit procedure with defined data model, we have performed an ensemble test with 10000 pseudo-experiments. Concerning the applied method, two different approaches have been used. First, the toy Monte Carlo samples have been generated according to the probability density function (PDF) defined in Eq. (4.6), for signal events, and Eq. (4.17), for background events. Once the results have been found to be consistent with the generated values, the second, more realistic, method has been used. Here, the signal events have been distributed directly from Geant3 (GSIM) signal MC while the background component just from the PDF.

As some of the input variables are not directly described by PDF in the fit and are data dependent, namely: vertex related variables ($\chi^2_{\mathrm{rec/tag}}$, ndf, $\sigma_{\mathrm{rec/tag}}$, number of tracks used in vertexing, lepton tag information), variables used for selection of the best B candidate (M_{bc}, $E^{\mathrm{CMS}}_{\mathrm{beam}}$) and variables used in the continuum suppression procedure ($\cos\theta_{\mathrm{B}}$), they must be generated according to the corresponding distributions observed in the real data; for signal events, the on-resonance data, for background events, the side-band data have been used. The expected total number of signal and background events, used in the toy MC studies, have been summarized in Tables 4.10 and 4.11.

The PDF-based toy MC results have clearly shown that expected low statistics in the neutral mode naturally leads to a wide distribution of $\mathcal{S}_{CP}$ and $\mathcal{A}_{CP}$ parameters, with one dominant tail beyond the physics boundaries $\langle -1; 1\rangle$; practically, the physics boundaries can be extended to $\sim \langle -1.4; 1.4\rangle$, due to a non-zero detector resolution. If the fitting region is not strictly limited to this interval, the asymmetric Gaussian tails are observed in the toy

MC results. Such tails start to be asymmetric right after reaching the physics boundaries and consequently, the fit model has a tendency to bias the mean value of CP violating parameters. In order to avoid such a physics related bias, the fit region has been limited to $\langle -1.4; 1.4 \rangle$ and the observed bias disappeared.

The fit results of GSIM-based toy MC studies of the neutral mode can be found in Figures 5.1 (branching ratio), 5.2 ($\mathcal{S}_{CP}$ parameter) and 5.3 ($\mathcal{A}_{CP}$ parameter).

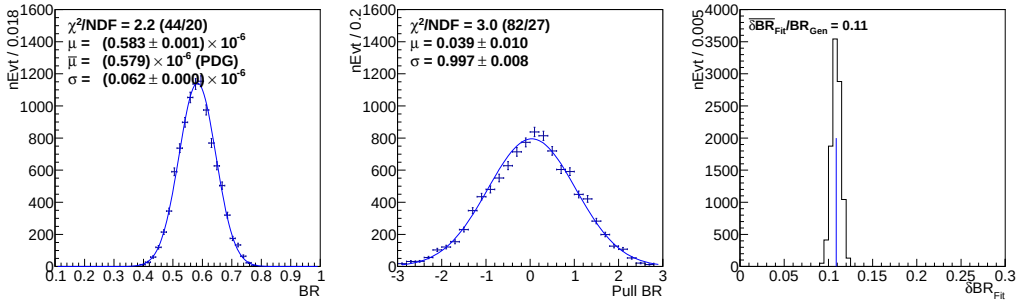

Fig. 5.1: **Neutral** mode: Toy MC distribution of branching ratio, $\mathcal{B}$, (left), $\mathcal{B}$ pull distribution (middle) and distribution of relative $\mathcal{B}$ fit uncertainties (right).

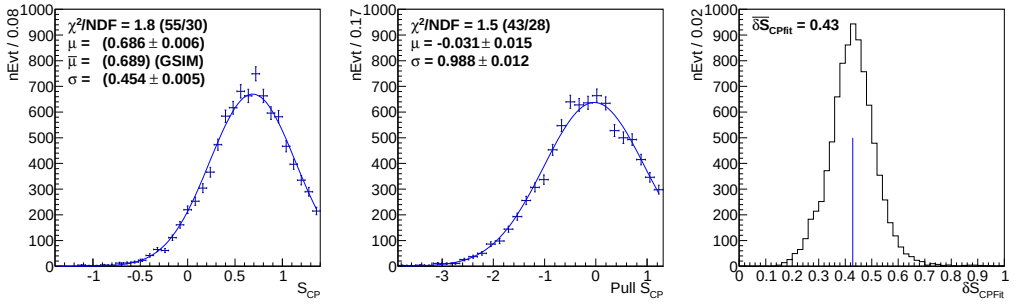

Fig. 5.2: **Neutral** mode: Toy MC distribution of $\mathcal{S}_{CP}$ parameter (left), $\mathcal{S}_{CP}$ pull distribution (middle) and distribution of $\mathcal{S}_{CP}$ fit uncertainties (right).

We have fitted each pseudo-experiment, using the defined fit model, and plotted the central value distributions of measured observables ($\mathcal{B}$, $\mathcal{S}_{CP}$ and $\mathcal{A}_{CP}$). Moreover, to check the consistency, we have plotted derived pull distributions and distributions of expected fit uncertainties. The input values for toy MC have been: $\mathcal{B} = 0.579 \times 10^{-6}$, $\mathcal{S}_{CP} = 0.689$ and $\mathcal{A}_{CP} = 0$. The obtained values of fit uncertainties together with the estimated systematic

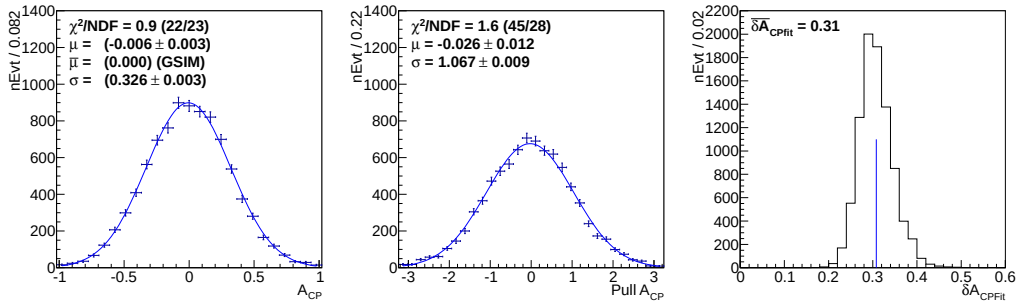

Fig. 5.3: **Neutral** mode: Toy MC distribution of $\mathcal{A}_{CP}$ parameter (left), $\mathcal{A}_{CP}$ pull distribution (middle) and distribution of $\mathcal{A}_{CP}$ fit uncertainties (right).

errors (due to a fit bias) are summarized in Table 5.1. No significant fit bias compared to statistical error has been observed, the fit model demonstrates to be consistent with the data. The fitting procedure can be considered as very stable, less than 0.5 % of all 10000 fits failed.

	σ_{stat}	$\sigma_{\text{syst}}^{\text{fit bias}}$
$\mathcal{B}^{\text{neutral}}$	11 %	+0.69 %
$\mathcal{S}_{CP}^{\text{neutral}}$	43 %	-0.44 %
$\mathcal{A}_{CP}^{\text{neutral}}$	31 %	+0.006

Tab. 5.1: **Neutral** mode: Summary of expected relative (absolute) fit uncertainties (statistical errors) and systematic errors due to the fit bias.

5.2 Linearity Test

Another test using pseudo-experiments has been performed in the neutral mode to check a linearity of the fitter and its output, $\mathcal{CP}$ violating parameters. The method used here has been exactly the same as described in the previous section, only the $\mathcal{S}_{CP}$ parameter has been varied individually from 0 to 1 in intervals of 0.1, while $\mathcal{A}_{CP}$ remained fixed to 0 and vice versa, $\mathcal{S}_{CP}$ remained fixed to 0.689 and $\mathcal{A}_{CP}$ has been varied from -0.5 to 0.5 in intervals of 0.1.

In total 10000 pseudo-experiments have been generated for each of the configurations. The final results are plotted in terms of residuals, i.e. the differences between the central value obtained from the toy MC distribution and

the generated value, and fitted with a straight line to determine a linearity and possible fit bias. A departure from a flat line with an intercept of zero indicates that a fit bias is present. The plots are shown in Figures 5.4 (residuals of CP violating parameters with respect to varying $\mathcal{S}_{CP}$) and 5.5 (residuals of CP violating parameters with respect to varying $\mathcal{A}_{CP}$). The curves indicate a negligible bias as observed in the previous section and a good linearity.

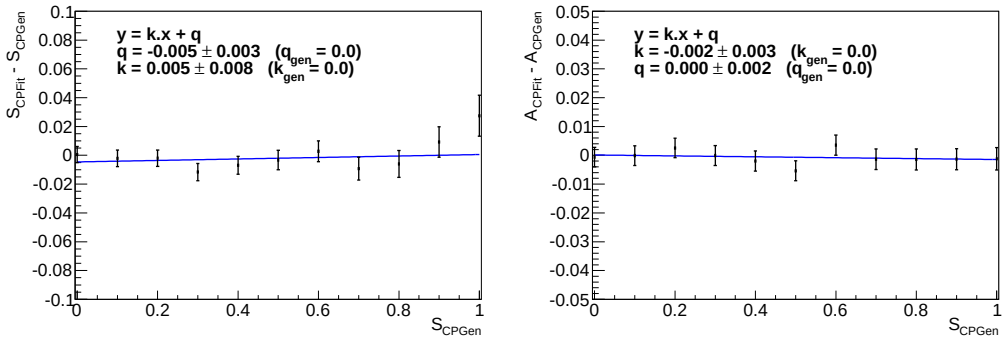

Fig. 5.4: **Neutral** mode: Linearity test for the time dependent physics parameters while varying $\mathcal{S}_{CP}$.

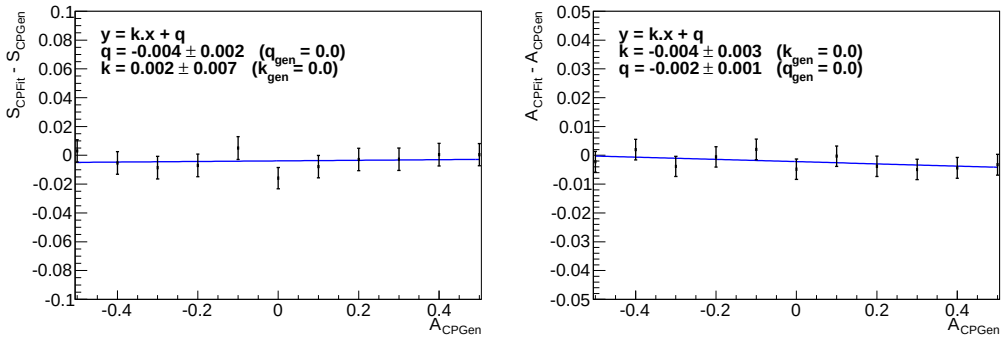

Fig. 5.5: **Neutral** mode: Linearity test for the time dependent physics parameters while varying $\mathcal{A}_{CP}$.

6 Control Sample Measurement

The physics mode, which is in its decay topology, detection efficiency and fit model description as much similar as possible to the measured mode, is typically used as a control sample. There are several aspects of its usage in the physics analysis. First, at e^+e^- accelerator machines a measured mode is usually worked out using a so-called "blind" analysis technique, where all selection criteria, together with all but fitted parameters, have to be determined before the final fit is performed. (No parameters optimization using the experimental data is allowed.) Here, the control sample serves as an ideal data sample to optimize the common selection criteria. Second, different Monte Carlo samples (signal MC, generic MC, rare MC), which are commonly used to define a data model, usually incorporate physics processes of the lowest order only and applied corrections of one order higher. Moreover, some physics processes are described just by phenomenological physics models. Therefore, the obtained MC results might differ from the physics reality. Even though the difference is considered to be rather small, it has to be corrected (calibrated) using a real data sample, i.e. a control sample. As detailed in Chapter 4, to account for the difference between MC and data, different calibration factors (offsets) have been introduced in the fitting model. Third, a comparison of control sample fit results with the values from PDG is necessary to cross-check the consistency of the fitting model and overall fit procedure. As an ideal control sample, the charged mode, $B \to \eta_c K^{\pm}$, $\eta_c \to p\bar{p}$, has been naturally chosen and analysed.

6.1 Fit Results

The fitting procedure has been performed in three different fit configurations: full 4D fit ($\Delta E \times m_{\eta_c} \times \Delta t \times q$), 2D fit ($\Delta E \times m_{\eta_c}$) and 2D×2D fit (see def. in Chapter 4). As a fitting method an unbinned ML has been applied with the likelihood defined as a sum of (4.7), for signal, and (4.18), for background, with $N_{\mathrm{SVD1}} = 245$ and $N_{\mathrm{SVD2}} = 1268$ candidates in SVD1 and SVD2 experiment, respectively. The 2D fit has been performed to test whether a 4-dimensional fit returns the same results (branching ratio) as a fitting

procedure without ($\Delta t \times q$) component. The other motivation behind is in the following: adding more dimensions in the fit model will put tighter constraints on the ML minimization procedure and consequently, will provide more precise results. The 2D×2D fit has been made to test the backward compatibility and simultaneously, to cross-check the new fit method with an older Belle analysis technique. The final fit results have been summarized in Table 6.1, 4D fit plots are depicted in Figure 6.1 and Figure 6.2, for SVD1 and SVD2 respectively, and the obtained correction (calibration) constants are given in corresponding Tables 6.2 and 6.3.

Configuration	$\mathcal{B}$ $[10^{-6}]$	$\mathcal{S}_{CP}$	$\mathcal{A}_{CP}$
4D fit	$1.63 \pm 0.10_{\text{stat}}$	$-0.011 \pm 0.160_{\text{stat}}$	$0.137 \pm 0.118_{\text{stat}}$
2D fit	$1.63 \pm 0.10_{\text{stat}}$	–	–
2D×2D	–	$-0.010 \pm 0.159_{\text{stat}}$	$0.137 \pm 0.117_{\text{stat}}$
PDG values	1.35 ± 0.23	0.0	0.0

Tab. 6.1: Summary of fit results in $B^{\pm} \to \eta_c K^{\pm}$, $\eta_c \to p\bar{p}$ and their PDG values [16].

The branching ratio has been calculated as a ratio of the measured number of signal events over the product of total number of Belle $B\bar{B}$ events and detection efficiency. The efficiency is particularly important in the relation; it corrects the obtained result for various imperfections in the detection method and applied analysis techniques:

$$\mathcal{B} = \frac{N_{\text{sig}}}{\varepsilon N_{B\bar{B}}} \tag{6.1}$$

The mean value of branching ratio has been corrected to account for the difference between MC and data using efficiency correction factors, η, defined and summarized in Sec. 3.1.9. The corrected values are:

$$\mathcal{B}_{\text{4D}} = 1.61 \pm 0.10_{\text{stat}} \tag{6.2}$$

$$\mathcal{B}_{\text{2D}} = 1.61 \pm 0.10_{\text{stat}} \tag{6.3}$$

Notice that both values, from 4D and 2D fit, are exactly the same. Thus in the end, the 2D measurement of branching ratio has been preferred to eliminate the systematic effects coming from the ($\Delta t \times q$) measurements. Similarly, the same approach will be followed in the neutral mode.

Concerning the fit of r-bin fractions and their correction factors, an important remark is in order here. Generally, when there exist more than one

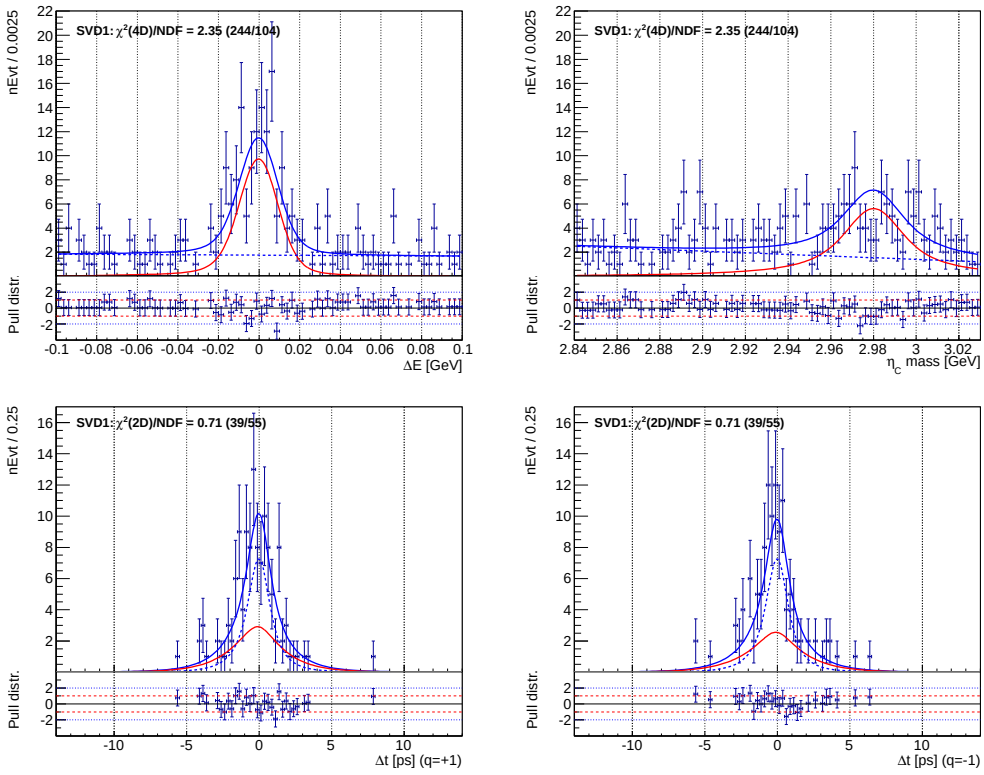

Fig. 6.1: Fit projections of control data sample for **SVD1** experiment ($B^{\pm} \to \eta_c K^{\pm}$, $\eta_c \to p\bar{p}$). The individual projections are: ΔE (top left), η_c invariant mass (top right), Δt for B tagged with $q = +1$ (down left) and Δt for B tagged with $q = -1$ (down right).

Correction Parameter	**Fit Result**
$\mu^{\mathrm{CF}}_{\mathrm{main}}(\Delta E)$	-0.0013 ± 0.0013
$\sigma^{\mathrm{CF}}_{\mathrm{main}}(\Delta E)$	$+1.02 \pm 0.13$
$\sigma^{\mathrm{CF\ Voigt}}_{\mathrm{main}}(m_{\eta_c})$	fixed to 1.0
$\tilde{\eta}^0_{\mathrm{sig}}$ (r-bin CF $l = 0$)	$+0.90 \pm 0.28$
$\tilde{\eta}^1_{\mathrm{sig}}$ (r-bin CF $l = 1$)	$+0.83 \pm 0.25$
$\tilde{\eta}^2_{\mathrm{sig}}$ (r-bin CF $l = 2$)	$+1.17 \pm 0.38$
$\tilde{\eta}^3_{\mathrm{sig}}$ (r-bin CF $l = 3$)	$+1.54 \pm 0.31$
$\tilde{\eta}^4_{\mathrm{sig}}$ (r-bin CF $l = 4$)	$+1.25 \pm 0.20$
$\tilde{\eta}^5_{\mathrm{sig}}$ (r-bin CF $l = 5$)	$+1.35 \pm 0.29$

Tab. 6.2: $B^{\pm} \to \eta_c K^{\pm}$, $\eta_c \to p\bar{p}$ correction factors (offsets) for ΔE mean and sigma, m_{η_c} sigma and signal r-bin fractions in **SVD1** experiment.

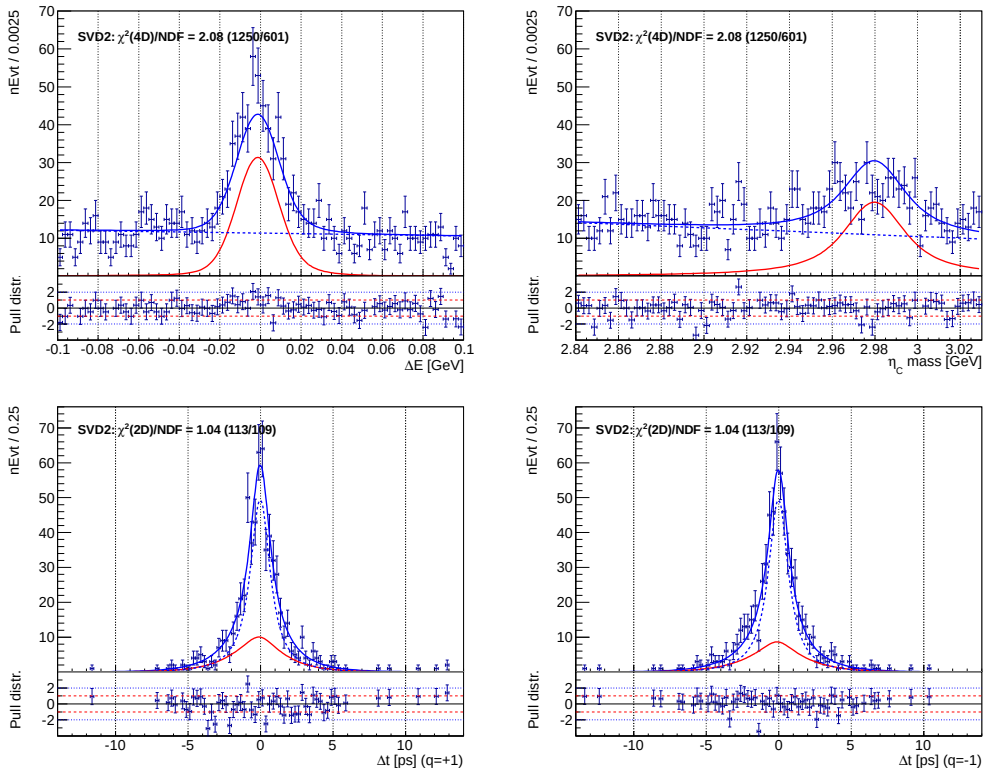

Fig. 6.2: Fit projections of control data sample for **SVD2** experiment ($B^{\pm} \to \eta_c K^{\pm}$, $\eta_c \to p\bar{p}$). The individual projections are: ΔE (top left), η_c invariant mass (top right), Δt for B tagged with $q = +1$ (down left) and Δt for B tagged with $q = -1$ (down right).

Correction Parameter	**Fit Result**
$\mu^{\mathrm{CF}}_{\mathrm{main}}(\Delta E)$	-0.0013 ± 0.0008
$\sigma^{\mathrm{CF}}_{\mathrm{main}}(\Delta E)$	$+1.10 \pm 0.08$
$\sigma^{\mathrm{CF\ Voigt}}_{\mathrm{main}}(m_{\eta_c})$	fixed to 1.0
$\tilde{\eta}^0_{\mathrm{sig}}$ (r-bin CF $l = 0$)	$+1.04 \pm 0.14$
$\tilde{\eta}^1_{\mathrm{sig}}$ (r-bin CF $l = 1$)	$+0.97 \pm 0.11$
$\tilde{\eta}^2_{\mathrm{sig}}$ (r-bin CF $l = 2$)	$+0.97 \pm 0.15$
$\tilde{\eta}^3_{\mathrm{sig}}$ (r-bin CF $l = 3$)	$+1.06 \pm 0.13$
$\tilde{\eta}^4_{\mathrm{sig}}$ (r-bin CF $l = 4$)	$+0.77 \pm 0.10$
$\tilde{\eta}^5_{\mathrm{sig}}$ (r-bin CF $l = 5$)	$+0.89 \pm 0.16$

Tab. 6.3: $B^{\pm} \to \eta_c K^{\pm}$, $\eta_c \to p\bar{p}$ correction factors (offsets) for ΔE mean and sigma, m_{η_c} sigma and signal r-bin fractions in **SVD2** experiment.

PDF fractions in the fit model, one has to limit each of them to a certain fit interval, otherwise the fitting procedure, using Minuit2 package here, might get unstable. This is especially important for data samples with low statistics. For this reason, following parameter transformation has been utilized for r-bin fractions (indexed by i):

$$\begin{aligned}
f^0 &= (1-\tilde{f}^5)(1-\tilde{f}^4)(1-\tilde{f}^3)(1-\tilde{f}^2)(1-\tilde{f}^1)(1-\tilde{f}^0)\\
f^1 &= (1-\tilde{f}^5)(1-\tilde{f}^4)(1-\tilde{f}^3)(1-\tilde{f}^2)(1-\tilde{f}^1)\tilde{f}^0\\
f^2 &= (1-\tilde{f}^5)(1-\tilde{f}^4)(1-\tilde{f}^3)(1-\tilde{f}^2)\tilde{f}^1\\
f^3 &= (1-\tilde{f}^5)(1-\tilde{f}^4)(1-\tilde{f}^3)\tilde{f}^2\\
f^4 &= (1-\tilde{f}^5)(1-\tilde{f}^4)\tilde{f}^3\\
f^5 &= (1-\tilde{f}^5)\tilde{f}^4\\
f^6 &= \tilde{f}^5,
\end{aligned}$$

where $\tilde{f}^i$ ($\tilde{\eta}^i$) represent Minuit2 input parameters, each limited to fit interval $\langle 0;1\rangle$, while their images f^i (η^i) stand for the real fractions (correction factors), the sum of which is the only Minuit2 limitation; it equals to one. For this reason, such a special transformation has been used. Each of the Minuit2 fraction parameters have been limited to the given interval $\langle 0;1\rangle$ and the r-bin fitting procedure has converged even using a low statistics data sample. The plots with obtained number of signal (background) events versus tag quality, r, (r-bin fractions) are shown in Figure 6.3.

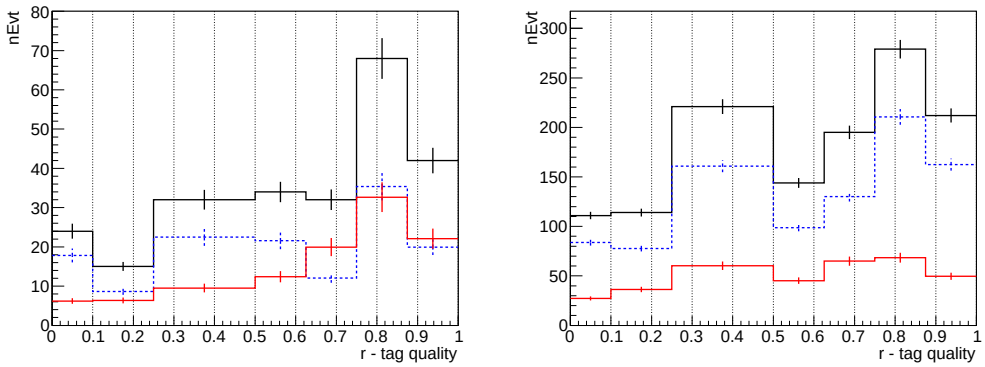

Fig. 6.3: Number of fit events versus tag quality, r, (r-bin fractions) in control data sample for SVD1 (left) and SVD2 (right) experiment. The number of signal (background) events is represented by solid red (dashed blue) curve, the sum of both contributions by solid black curve.

Finally, a raw asymmetry has been calculated and plotted together with

the background subtracted Δt distributions, see Figure 6.4. It combines

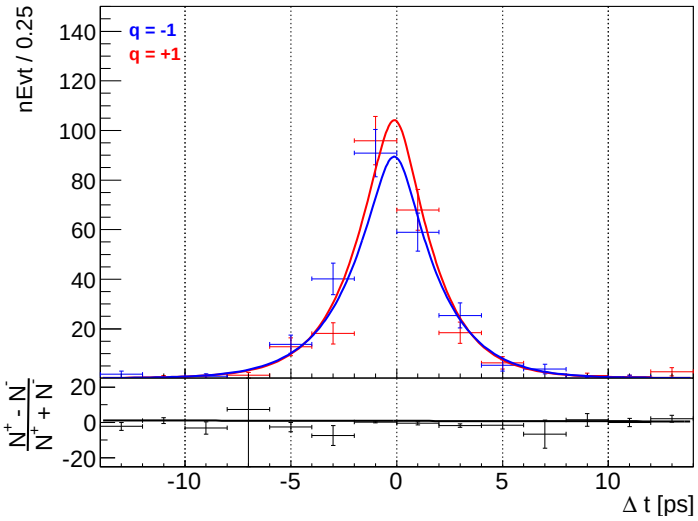

Fig. 6.4: The background subtracted Δt distributions for $q = +1$ (red curve), $q = -1$ (blue curve) and raw asymmetry (bottom black curve).

control sample results from both SVD1 and SVD2 experiments. The raw asymmetry has been defined as a normalized difference of Δt signal PDFs:

$$\frac{\mathcal{P}(\Delta t, q = +1) - \mathcal{P}(\Delta t, q = -1)}{\mathcal{P}(\Delta t, q = +1) + \mathcal{P}(\Delta t, q = -1)}, \tag{6.4}$$

where $\mathcal{P}(\Delta t, q = +1)$ ($\mathcal{P}(\Delta t, q = -1)$) represents a Δt signal PDF with B tagged with charge $q = +1$ ($q = -1$). The data points plotted in the graph are experimental data minus the number of events estimated from the background PDF.

6.2 Validity Study and Consistency Check

To test the fitting procedure in the control sample, two independent cross-checks have been done: a fit validity study using toy MC simulations and $B^{\pm}$ lifetime measurement. The first is described in Subsec. 6.2.1, the latter in Subsec. 6.2.2.

6.2.1 Toy MC Simulation

Similarly as for the neutral mode, see Chapter 5, we have performed an ensamble test with 1000 pseudo-experiments for the charged mode. This procedure is very important, because the control sample provides the calibration factors (offsets) for the neutral mode and a potential bias would automatically propagate into the measurement of CP violating parameters in the neutral mode. First, in order to check that the overall fitting procedure can be regarded as self-consistent, the PDF-based toy MC studies have been performed. The obtained results have clearly shown perfect agreement with the generated values of branching ratio and CP violating parameters. Only a negligible bias has been observed. After this cross-check, the GSIM-based toy MC ensamble test has been prepared. The obtained results have again demonstrated a reasonable agreement with the GSIM input values. A small bias in the branching ratio measurement, yet negligible compared to the statistical error, has been observed. It will be taken into account further in terms of a systematic uncertainty. For illustration, the GSIM-based toy MC results have been depicted in Fig. 6.5.

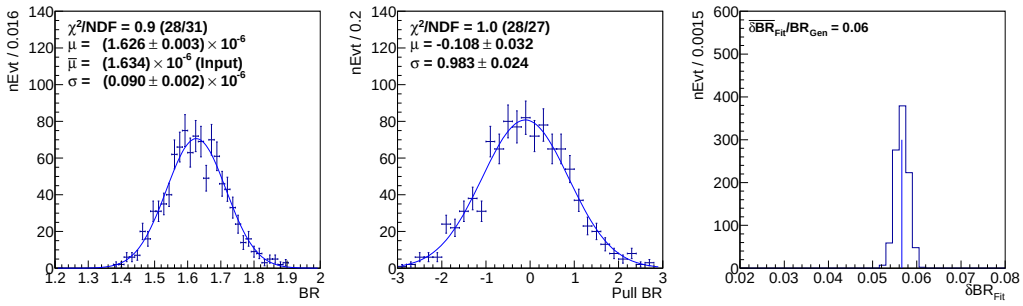

Fig. 6.5: **Charged** mode: Toy MC distribution of branching ratio, $\mathcal{B}$, (left), $\mathcal{B}$ pull distribution (middle) and distribution of relative $\mathcal{B}$ fit uncertainties (right).

6.2.2 Lifetime Measurement

A 4D fit with CP violating parameters fixed to zero and lifetime parameter released has been performed in order to measure the $B^{\pm}$ lifetime and therefore, to check the consistency of the overall fit procedure. (The other fit parameters have remained fixed/released as for the branching ratio measurement.) The obtained result, provided with a statistical uncertainty only:

$$\tau_{B^{\pm}} = (1.588 \pm 0.112_{\,\mathrm{stat}})\,\mathrm{ps} \tag{6.5}$$

is in full agreement with the world average [18], $\tau_{B^\pm} = (1.641 \pm 0.008)$ ps.

6.3 Optimization Study of $\mathcal{CS}_{\rm cut}$

Subsection 3.1.6 (in Chapter 3) is dedicated to the continuum suppression procedure as well as to the strategy how to choose an optimal value of $\mathcal{CS}_{\rm cut}$. In addition, this subsection explains in detail which suppression strategies are preferred more for branching ratio measurement (F.O.M.) and which are usually used in the measurement of CP violation parameters (a low value of $\mathcal{CS}_{\rm cut}$ typically used). In order to test whether two different cut values have to be chosen for these two measurements or rather the same value can be applied, we have run the fitter on the data model with the $\mathcal{CS}_{\rm cut}$ set to several values: from 0.15 to 0.70, with step of 0.1. The cut values have been chosen such as the tested interval fully covered the optimal region from the perspective of F.O.M., see Fig.3.7. As can be clearly seen from Table 6.4, where all fit results have been summarized, the statistical error on branching ratio has remained constant, independently on the selected cut value. Moreover, no real systematic bias has been observed, the mean values perfectly agree with each other.

$\mathcal{CS}_{\rm cut}$	$\varepsilon_{\rm SVD1}$ [%]	$\varepsilon_{\rm SVD2}$ [%]	Yield(SVD1)	Yield(SVD2)	$\mathcal{B}[\times 10^6]$
0.15	33.66	38.49	108.4 ± 13.2	321.6 ± 25.8	(1.64 ± 0.10)
0.20	**33.33**	**38.12**	$\mathbf{105.8 \pm 12.7}$	$\mathbf{359.7 \pm 25.2}$	$(\mathbf{1.63 \pm 0.10})$
0.25	33.00	37.74	102.9 ± 12.3	354.5 ± 24.6	(1.62 ± 0.10)
0.30	32.69	37.31	99.2 ± 12.0	352.2 ± 24.3	(1.63 ± 0.10)
0.40	32.04	36.45	97.4 ± 11.6	348.4 ± 23.7	(1.63 ± 0.10)
0.50	31.25	35.37	93.2 ± 11.3	349.7 ± 23.4	(1.62 ± 0.10)
0.60	30.27	33.93	91.4 ± 11.0	331.9 ± 22.6	(1.66 ± 0.10)
0.70	28.92	31.87	85.0 ± 10.7	305.2 ± 21.1	(1.62 ± 0.10)

Tab. 6.4: Control sample yield and branching ratio based on different level of continuum suppression, i.e. likelihood ratio cut, $\mathcal{CS}_{\rm cut}$.

Concluding the results of optimization study, the higher values of $\mathcal{CS}_{\rm cut}$ generally don't help to increase the measurement precision in this decay mode, as originally expected. With a higher $\mathcal{CS}_{\rm cut}$ value applied a branch-

ing ratio is measured with the same statistical significance, so no improvement has been observed. On the other hand, the measurement of CP violation parameters starts to suffer from extra systematic effects as the cut increases. Therefore, we set the continuum suppression cut to the lowest possible value, while keeping the background suppression factor significantly high, see Fig. 3.6. The $\mathcal{CS}_{\rm cut}$ has been set to 0.2.

6.4 Systematic Uncertainties

In this analysis, we expect that statistical uncertainties will dominate over systematic effects, mainly due to a low branching ratio of the decay mode. Despite this fact, the systematic errors will still significantly contribute to the precision of branching ratio measurement, $\mathcal{B}(B^{\pm} \to \eta_c K^{\pm}) \times \mathcal{B}(\eta_c \to p\bar{p})$, and therefore, have to be carefully studied. This section lists all systematic effects and where necessary, more detailed description of corresponding technique used to calculate a systematic uncertainty is given.

More or less, we have followed a standard Belle procedure to estimate the systematic effects. Major sources, coming from determination of number of $B\bar{B}$ events, tracking efficiency, $K^0_{\rm S}$ reconstruction or particle ID have been analysed independently, in various Belle studies. As a result, most of these systematic errors can be easily assessed through the obtained look-up tables by using various discriminating variables (usually kinematic variables). At the input, one provides the values of one or more discriminating variables, typically specific for the studied physics analysis. At the output, one gets an estimated systematic error and/or correction factor to the detection efficiency.

Some contributions, typically arising from application of non-standard selection criteria or when using a different analysis technique, have to be studied independently. In those cases, more detailed description of applied procedure has been provided. Let us stress that the same procedure will be used in the estimation of systematic errors for the neutral mode (where applicable).

- **Number of $B\bar{B}$ events** - contributes with a relative error of 1.37 %. This value has been derived from the absolute error on the total number of B events, $N_{B\bar{B}}$, determined in an independent Belle study [29].

- **Tracking efficiency** - contributes with a relative error of 1.05 %. Depending on a track momentum there is a certain probability that the tracking algorithm doesn't find a track. This directly propagates into the reconstruction inefficiency. The independent Belle study [44]

has shown that for high-momenta charged tracks, $p_{\mathrm{T}} > 200\,\mathrm{MeV}/c$, there applies a systematic uncertainty of 0.35 % per track. For this mode (charged mode) there are three high-momenta charged tracks, i.e. the uncertainty equals $3 \times 0.35\,\%$.

- **Kaon PID** - contributes with a relative error of 0.99 %. Based on the look-up tables, provided by independent Belle study [31], with following discriminating variables: $|p_{\mathrm{kaon}}|$ and $\cos(\theta_{\mathrm{kaon}})$, one can find the correction factors to the detection efficiency together with a systematic error on the final branching ratio measurement. The value of the uncertainty is strongly dependent on how tight a selection criterion on likelihood ratio has been used. In our case a soft cut, $\mathcal{L}_{\mathrm{K}/\pi} > 0.6$, has been applied.

- **Proton PID** - contributes with a relative error of 0.67 %. For proton PID, the cuts on likelihood ratio $\mathcal{L}_{\mathrm{p/K}}$, $\mathcal{L}_{\mathrm{p}/\pi}$, have been set to a low value, 0.4, just with the intention not to generate extra systematic effects due to PID. Generally, with such mild selection criteria, one doesn't expect that the number of obtained signal events would significantly change once the cut is decreased or completely removed. Only the level of background might increase. In reality a small systematic shift has been observed when the likelihood cuts were decreased by ~ 0.05 or removed. The similar effect appeared after removing the selection criterion used to eliminate proton-like electrons, $\equiv p(e) = 1.0$. In order to make a proper estimate of this systematic effect, we have rebuilt the whole data model (with a released cut), refitted the data and taken the absolute difference as a systematic uncertainty.

- **Continuum suppression cut** - contributes with a relative error of 0.56 %. A similar approach as for the previous systematic error, $\delta_{\mathrm{p(PID)}}$, has been applied . When varying a value of the continuum selection cut by ∓ 0.05 ($\mathcal{CS}_{\mathrm{cut}} = 0.2$), the level of signal remains roughly constant, see Fig. 3.6, but the continuum background increases/decreases. The effect of absolute change in branching ratio is counted as the systematic effect of the cut. Such a simplified estimate works well for studies where a cut value has not been set tight. This is true for values of $\mathcal{CS}_{\mathrm{cut}}$ and proton PID cut used in this analysis.

- **Model shape** - contributes with a relative error of 2.22 %. Variations in the parametric model shape due to limited statistics are accounted for by varying each parameter of the data model within their errors, $\pm 2\sigma$ for parameters determined from MC studies, $\pm\sigma$ for parameters

determined from side-band data, control sample, etc. (applicable for the neutral mode).

- **Physics parameters** - contribute with a relative error of 2.13 %. The situation is very similar to the estimate of systematic uncertainties for the model shape. The physics parameters have been fixed to the world averages [16] during the data fit, so varying their values by $\pm\sigma$ one can estimate the systematic error. The dominant uncertainty arises from the width of η_c resonance.

- **Fit bias** - contributes with a relative error of 0.52 %. In order to estimate a fit bias, we have performed toy MC ensemble tests, see Section 6.2.1 and the bias has been estimated as a difference between the input value, i.e. the measured value, and the value of $\mathcal{B}$ obtained at the output from the toy MC. The results are shown in Fig. 6.5

- **Interference between η_c and J/ψ** - contributes with a systematic uncertainty of 0.62 %. The right bound of the invariant mass window has been optimized in a way so that the contribution from J/ψ events to η_c resonance events falls below an expected η_c event statistical fluctuations. The main motivation is to avoid the interference region and therefore, not to generate extra systematic effects, which might then appear. The value of η_c selection window has been optimized using generic MC samples, for more details see Sec. 3.1.5. Despite the interference effects, quite a tight selection cut on the right side of the interval might serve as an extra source of a systematic uncertainty too. Therefore, we have loosened the cut by roughly a detector resolution, $\sigma \sim 5\,\mathrm{MeV}$, namely by 1 and 2σ, and the higher difference has been taken as an estimate of the systematic uncertainty.

- M_{bc} **signal window** - contributes with a negligible error. The measured branching ratio may not depend on the selected values of signal window limits, i.e. the M_{bc} selection criteria, once the correct values of detection efficiency have been applied in calculation of branching ratio. Since the detector resolution can be estimated, in the M_{bc} observable, as $\sigma \sim 2.5\,\mathrm{MeV}$, we have lowered the left bound by 1 and 2σ, respectively, and checked a possible bias. Only the lower bound has been investigated, the higher bound is already at the kinematic limit. The observed bias has shown to be relatively high, 4 % in maximum, yet smaller compared to the statistical error. In addition, the bias has been found dependent on the selection cut. In order to find out if this

effect arises naturally because of the enlarged data sample (with significantly increased background level) or if it represents a real systematic error, we have performed a dedicated toy MC study. In the first case the bias would appear as a result of pure statistical fluctuations, in the latter case it would mean a deeper problem in the analysis. Therefore, we have rebuilt the data model in a new configuration (with the left selection cut lowered by 1 and 2σ, respectively, versus the original value), performed two ensamble tests with 1000 pseudo-experiments each (new versus original) and tested the origin of the shift compared to the nominal model with the fitter. Let us stress that the toy MC data with original cuts represented a sub-sample of the toy MC data with the new cuts. As a result we have obtained a differential distribution ($\mathcal{B}_{\text{orig}}$ minus $\mathcal{B}_{\text{new}}$) with a mean compatible with zero and sigma equal to 6.5 %, representing the studied relative strength of statistical fluctuations of the fitter. Based on the result, we have concluded that an observed bias is due to statistical fluctuations only and not an effect of systematic error, as originally expected.

Relative sys. error	**Value [%]**
$\delta_{N_{B\bar{B}}}$	1.37
δ_{Tracking}	1.05
$\delta_{\text{Kaon PID}}$	0.99
$\delta_{\text{Proton PID}}$	0.67
$\delta_{\mathcal{CS}}$	0.56
$\delta_{\text{Model shape}}$	2.22
$\delta_{\text{PDG values}}$	2.13
$\delta_{\text{Fit bias}}$	0.52
$\delta_{\text{Interference}}$	0.62
$\delta_{M_{\text{bc}}}$	–
δ_{Total}	3.85

Tab. 6.5: Systematic uncertainties in measurement of $\mathcal{B}(B^{\pm} \to \eta_{\text{c}} K^{\pm}) \times \mathcal{B}(\eta_c \to p\bar{p})$.

Since the branching ratio has been determined from a 2D fit only (with no $(\Delta \times q)$ component included in the data model), the systematic effects regarding vertexing, tagging, etc. have not been included in the final result.

On the other hand, for the measurement of CP violating parameters (neutral mode) these effects will start to play a significant role. All systematic effects, as well as the quadratic sum (total systematic error), have been listed in Tab. 6.5. The dominant contributions to the total systematic error come from the model shape and physics parameters.

6.5 Summary

The measurement of branching ratio and CP violating parameters in the control sample has provided following results:

$$\mathcal{B} = (1.61 \pm 0.10_{\text{stat}} \pm 0.06_{\text{syst}}) \times 10^{-6} \quad (6.6)$$

$$\mathcal{S}_{CP} = -0.011 \pm 0.160_{\text{stat}} \quad (6.7)$$

$$\mathcal{A}_{CP} = +0.137 \pm 0.118_{\text{stat}}, \quad (6.8)$$

where CP parameters are listed with a statistical error only.

Comparing the branching ratio with a world average value (PDG value), $\mathcal{B}_{\text{PDG}} = (9.6 \pm 1.2) \times (1.41 \pm 0.17) \times 10^{-7} \equiv (1.35 \pm 0.23) \times 10^{-6}$, one gets a good agreement; the branching ratio is within ~ 1 sigma consistent with the PDG value. Moreover, the measured CP violating parameters are statistically consistent with zero value. Therefore, as expected from the SM theory, no direct CP violation has been observed in the control sample. Such experimental results have clearly proved a full consistency of the overall fitter and applied data model.

Due to a rather limited statistics, the result has been obtained with the same precision in terms of branching ratio from a 2D as well as 4D fitter. In conclusion, it doesn't make any good sense to use a multi-dimensional 4D fitter to achieve more precise results for $\mathcal{B}$ measurements, as originally expected. On the other hand, for the determination of CP violating parameters a different conclusion has been made. The statistical error on these parameters are for both methods almost the same, but for 2D×2D approach one needs to fix the yields (signal/background fractions, $B\bar{B}/q\bar{q}$ background fraction, ...), which naturally outputs then in terms of extra systematic errors; in contrast to 4D results. Moreover, for backward consistency, we can conclude that the results from the 4D fitter have been found fully compatible with the old approach, using 2D×2D fitter.

Finally, using the control sample, the optimal value of continuum suppression cut has been chosen and the calibration factors (offsets) have been determined. These parameters accounting for the various imperfections of MC when building a data model, need to be properly adjusted. In contrast

to the charged mode, the neutral one is not measured with such high statistics and the corrections can't be determined directly from data. Correction factors as well as other parameters have been summarized in Appendix C.

7 *CP*-Violation Measurement

This chapter presents a branching ratio and CP violation parameters measurement in $B^0 \to \eta_c K^0_S$, $\eta_c \to p\bar{p}$ decay with the full Belle dataset which contains 772×10^6 $B\bar{B}$ events. The standard Belle approach assumes that all important consistency checks and validity tests have been performed first, before the final data can be analysed. This is called a "blind" analysis technique and the key point in such an approach is not to introduce any bias into the obtained results, either by accident or intentionally. Since the previous chapters have clearly shown that the data model and the fitter results are fully consistent with the values we generally expect, namely at the level of the control sample measurement and the validity tests in the neutral mode, we can step to the last point of the analysis and open the "box".

For comparison, the previous measurement was done with SVD1 data and three statistically significant η_c decays: $p\bar{p}$, $K^0_S K^\pm \pi^\mp$ and $K^\pm K^\mp \pi^0$. The obtained result, $\mathcal{S}_{CP} = 1.26^{+0.27}_{-0.39} \pm 0.06_{\text{syst}}$, was 3σ away from the zero hypothesis and fully consistent with the measurement in $B^0 \to J/\psi K^0_S$. As the ensemble test has shown, with pure $\eta_c \to p\bar{p}$ decay but full Belle data sample we expect a result with roughly the same statistical significance.

7.1 Fit Results

All fit results have been summarized in Table 7.1, the individual plots, separately depicted for SVD1 and SVD2 experiment, are shown in Figures 7.1 and 7.2, respectively. The fit errors listed together with measured values in Table 7.1 are statistical only, the PDG values, added for comparison, are with a total error, statistical plus systematic. The measurement of $\mathcal{S}_{CP}$ parameter can be compared with a PDG value, representing a combined result of CP violation parameter from currently all $b \to c\bar{c}s$ measurements.

Similarly as for the control sample, the branching ratio ($\mathcal{B}$) has been determined from the 2D fit only. With this approach we can eliminate the systematic errors coming from the $(\Delta t \times q)$ component. As will be seen in the next section, the systematic errors coming right from the Δt measurement represent the highest contribution to the overall systematic error.

Configuration	$\mathcal{B}$ $[10^{-6}]$	$\mathcal{S}_{CP}$	$\mathcal{A}_{CP}$
2D fit	$0.59 \pm 0.07_{\text{stat}}$	–	–
4D fit	–	$0.68^{+0.38}_{-0.46}$	$0.00^{+0.23}_{-0.31}$
PDG values	0.59 ± 0.11	0.679 ± 0.020	consistent with zero

Tab. 7.1: Summary of fit results in $B^0 \to \eta_c K^0_S$, $\eta_c \to p\bar{p}$ and their PDG values [16].

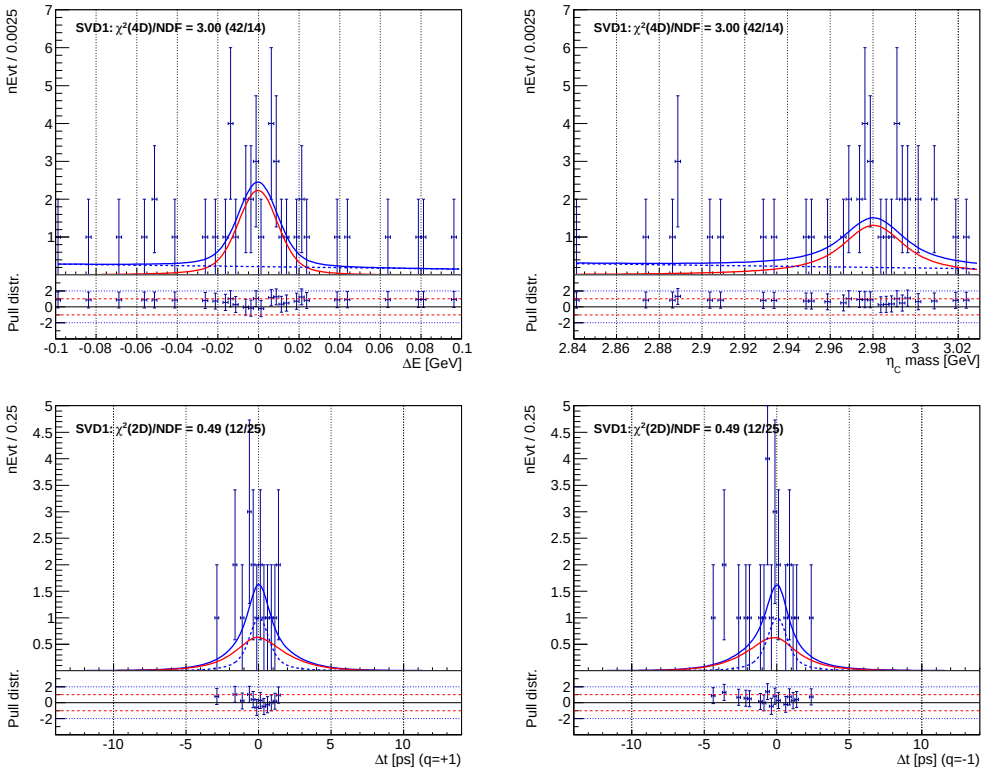

Fig. 7.1: Fit projections for **SVD1** experiment in $B^0 \to \eta_c K^0_S$, $\eta_c \to p\bar{p}$: ΔE (top left), η_c invariant mass (top right), Δt for B tagged with $q = +1$ (down left) and Δt for B tagged with $q = -1$ (down right).

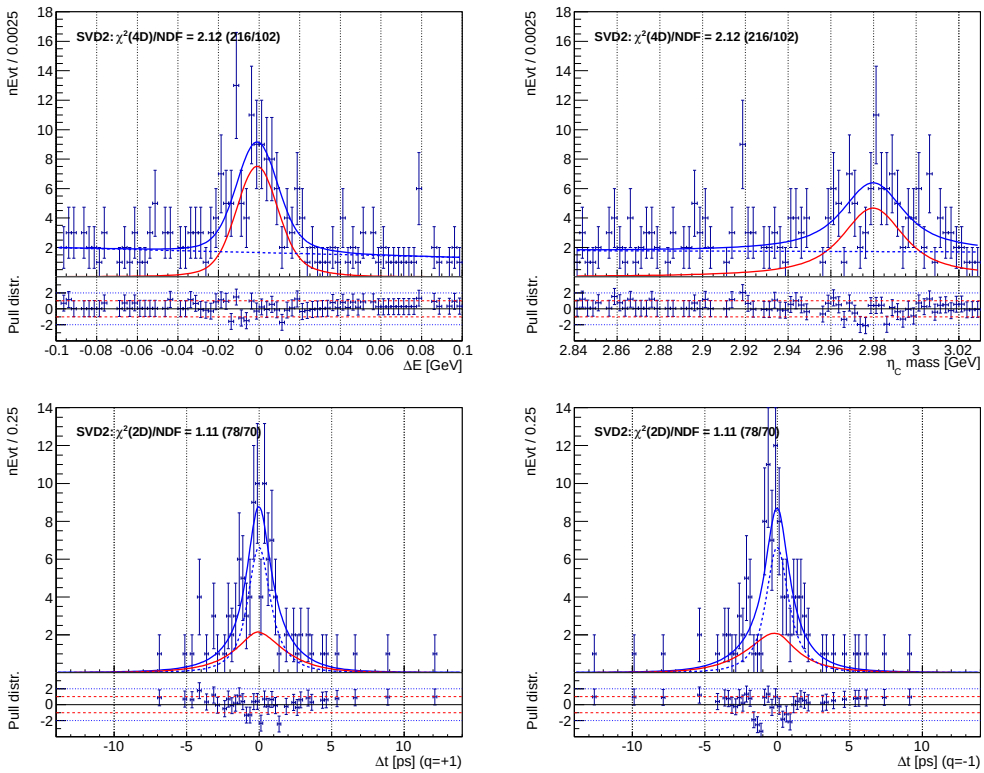

Fig. 7.2: Fit projections for **SVD2** experiment in $B^0 \to \eta_c K^0_S$, $\eta_c \to p\bar{p}$: ΔE (top left), η_c invariant mass (top right), Δt for B tagged with $q = +1$ (down left) and Δt for B tagged with $q = -1$ (down right).

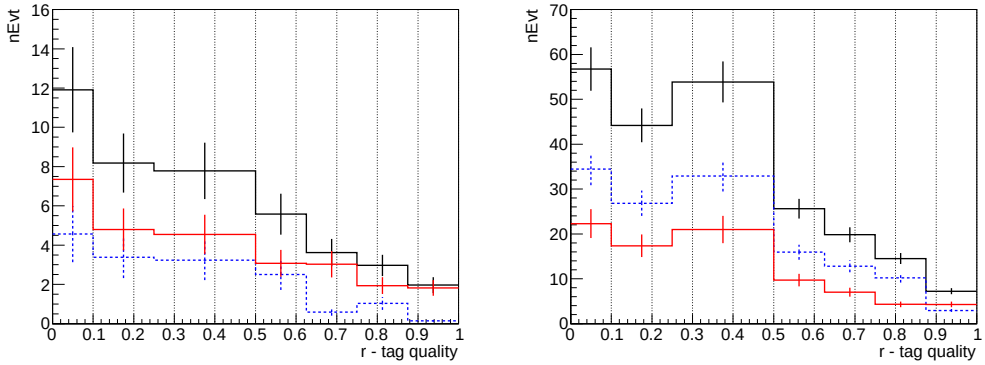

Fig. 7.3: Number of fit events versus tag quality, r, (r-bin fractions) for SVD1 (left) and SVD2 (right) experiment. The number of signal (background) events is represented by solid red (dashed blue) curve, the sum of both contributions by solid black curve.

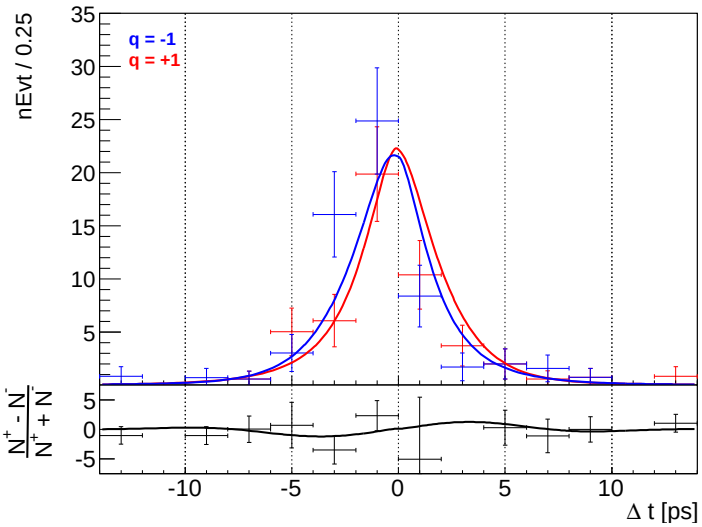

Fig. 7.4: The background subtracted Δt distributions for $q = +1$ (red curve), $q = -1$ (blue curve) and raw asymmetry (bottom black curve).

7.2 Consistency Check

As a consistency check we have performed a 4D fit to Belle data sample to measure the lifetime. The CP violating parameters have been fixed to the world average and zero value, for $\mathcal{S}_{CP}$ and $\mathcal{A}_{CP}$, respectively, while the parameter representing B^0 lifetime has been released. We have obtained:

$$\tau_{B^0} = (1.349 \pm 0.179_{\,\mathrm{stat}})\,\mathrm{ps}, \tag{7.1}$$

which is in full agreement with the current world average [18], $\tau_{B^0} = (1.519 \pm 0.007)$ ps.

7.3 Systematic Uncertainties

When estimating branching ratio systematic uncertainties we have followed the same analysis procedures as already described in a dedicated section of Control Sample Measurement, see Sec. 6.4. Most sources of the branching ratio systematic errors affect only the detection efficiencies, so their contribution to the measurement of CP violating parameters can be safely neglected. This is the reason, why zero values (denoted as "–") are listed for such contributions in the final summary table.

This section also deals with the systematic errors that directly affect the measurement precision of CP violating parameters, $\mathcal{S}_{CP}$ and $\mathcal{A}_{CP}$. These errors are mainly related to the precision of the fit procedure in $(\Delta t \times q)$ dimension. In order to estimate these errors carefully, we have closely followed the systematic procedures that have been established for the time-dependent analyses by Belle collaboration. Where not straightforward we have provided a detailed explanation of applied techniques together with an estimation of contributing systematic errors. In general, a conservative approach has been used, parameter values or cut values have been changed by their characteristic values (plus/minus sigma, etc.) and the bigger difference has been taken then as a systematic bias. If more parameters affect the measurement, the quadratic sum of their systematic contributions is taken as an estimate of the error. For lucidity, all systematic uncertainties, together with a total value, have been summarized at the end of this section, in Table 7.2.

- **Number of $B\bar{B}$ events** - contributes with a relative error of 1.37 % to $\mathcal{B}$ measurement.
- **Tracking efficiency** - contributes with a relative error of 0.70 % to $\mathcal{B}$ measurement. In contrast to the charged mode, only two high-momenta tracks are analysed in the final state.

- **Neutral kaon PID** - contributes with a relative error of 0.82 % to $\mathcal{B}$ measurement. To estimate the error, we have utilized the look-up tables provided by a dedicated Belle study [41]. As discriminating variables the $|p_{K^0_S}|$ and $\cos(\theta_{K^0_S})$ have been used.

- **Proton PID** - contributes with a negligible error.

- **Continuum suppression cut** - contributes with a negligible error.

- **Model shape** - contributes with a systematic error of 1.22 %, 3.96×10^{-2} and 2.38×10^{-2} to the measurement of $\mathcal{B}$, $\mathcal{S}_{CP}$ and $\mathcal{A}_{CP}$ parameter, respectively. Variations in the parametric model shape due to limited statistics are accounted for by varying each parameter of the data model within their errors, $\pm 2\sigma$ for parameters determined from MC studies, $\pm\sigma$ for parameters determined from side-band data or control sample. The biggest contributions come from the Δt background parameters, corrections to signal r-bin fractions and the background r-bin fractions.

- **Physics parameters** - contribute with a relative error of 1.01 %, 1.23×10^{-2} and 0.24×10^{-2} to $\mathcal{B}$, $\mathcal{S}_{CP}$ and $\mathcal{A}_{CP}$ measurement, respectively. Following physics related parameters have been varied by their respective PDG errors: M_{η_c}, Γ_{η_c}, τ_{B^0} and Δm_d. The biggest contribution comes from the Γ_{η_c}.

- **Fit bias** - contributes with a relative error of 0.73 %, 0.30×10^{-2} and 0.56×10^{-2} to the measurement of $\mathcal{B}$, $\mathcal{S}_{CP}$ and $\mathcal{A}_{CP}$, respectively. The fit biases have been estimated from several toy MC ensemble tests, which are separately discussed in a Validity Study Chapter, see Chap. 5.

- **Interference between η_c and J/ψ** - contributes with a negligible error.

- M_{bc} **signal window** - contributes with a negligible error.

- **IP profile** - contributes with 2.24×10^{-2} and 1.21×10^{-2} systematic error to the measurement of $\mathcal{S}_{CP}$ and $\mathcal{A}_{CP}$ parameter, respectively. As detailed in Sec. 3.1.8, the vertex position of B_{rec} and B_{tag} candidates have been determined from a constrained fit using information on charged daughters and an extra constraint on the vertex position using ellipsoidal IP profile dimensions. In order to additionally account for the effect of finite B meson flight length, the IP profile in $r\phi$ direction has been smeared by a gaussian distribution, with sigma equal to 21 µm. When varying this value by -10 µm or +20 µm we can roughly

estimate the systematic effect of the finite B meson flight length on CP violation measurement. This technique follows the standard Belle procedure.

- **Track helix errors** - contribute with a negligible error to the measurement of $\mathcal{S}_{CP}$ and $\mathcal{A}_{CP}$ parameters. The Δt uncertainty in time-dependent physics analysis is typically derived from an uncertainty on helix parameters. So if the helix errors are too optimistic/pessimistic, an observed bias is directly propagated to the Δt measurement. The errors on helix parameters determined from full simulations are found to be too optimistic, therefore a special correction factor(s), called scale error, has been introduced. This correction is estimated from the comparison of full Belle MC simulations of cosmic events versus the real data. More details about the scale error and its application can be found in [36]. To estimate the generated systematic effect we apply a new approach as described in [45], rather than a standard Belle conservative technique. The standard procedure consisted in switching on/off the scale error and taking the absolute difference between the two scenarios as a systematic uncertainty. In [45], the authors noticed that the errors on helix parameters are highly correlated with the lifetime and $\Delta m_{\rm d}$ fit results. So, if we find the bias in τ_{B^0} and $\Delta m_{\rm d}$ measurement compared to the PDG values, we can estimate this systematic error. It is derived as a difference between the fit results of CP violating parameters with τ_{B^0} and $\Delta m_{\rm d}$ values fixed from the high-statistics control samples and the nominal fit results, where the τ_{B^0} and $\Delta m_{\rm d}$ are taken from the PDG. The control sample values have not been extracted here, but taken from [45] instead : $\tau_{B^0} = (1.5299 \pm 0.0029)\,\text{ps}$, $\Delta m_{\rm d} = (0.5088 \pm 0.0019)\,\text{ps}^{-1}$.

- **Vertex quality parameters** - contribute with 7.26×10^{-2} and 7.20×10^{-2} to the systematic error of $\mathcal{S}_{CP}$ and $\mathcal{A}_{CP}$, respectively. The B vertex quality selection criteria, $h^{\rm rec,tag} < 50$, are varied by $+50$ and -25. The z vertex error requirements, $\sigma_{\rm z}^{\rm rec,tag} < 200$ (500) μm for multi (single) track vertices, are varied by $\pm 100\,\mu$m.

- **Selection criteria in B-tagging algorithm** - contribute with 4.19×10^{-2} and 3.40×10^{-2} systematic error to the measurement of $\mathcal{S}_{CP}$ and $\mathcal{A}_{CP}$ parameter, respectively. The tagging algorithm requires a set of selection criteria to be applied in order to significantly suppress tracks not originating from the primary vertex ($K^0_{\rm S}$ suppression and so-called "Tokyo" cut) or to remove tracks with a poor resolution in z-direction. So first, the impact parameter in $r\phi$, dr, is required to

be lower than 500 µm with respect to $B_{\rm rec}$ vertex. Second, the track positions must be measured more accurately than 500 µm in z direction, $\sigma_{\rm z} < 500\,\mu$m. The systematic effect on physics results has been investigated by a variation of these selection criteria by ±10 %. For more details about "Tokyo cut", read for example [38].

- Δt **selection range** - contributes with 0.08×10^{-2} and 0.12×10^{-2} to the systematic error of $\mathcal{S}_{CP}$ and $\mathcal{A}_{CP}$ parameter, respectively . The requirement of $|\Delta t| < 70$ ps is varied by ±30 ps to account for outliers and tails of resolution function.

- Δz **bias** - contributes with 0.39×10^{-2} and 0.50×10^{-2} to the systematic error of $\mathcal{S}_{CP}$ and $\mathcal{A}_{CP}$ parameter, respectively. Once the resolution function is applied, the average value of measured Δz value minus the true value may not be zero. Such a bias has been observed and it comes from a relative misalignment between SVD and CDC detectors. This effect has been studied in the final measurement of $B^0 \to J/\psi\ K^0_{\rm S}$, see [45], and is considered to be mode independent. Thus the error is taken from there.

- **SVD misalignment** - contributes with 0.24×10^{-2} and 0.41×10^{-2} to the systematic error of $\mathcal{S}_{CP}$ and $\mathcal{A}_{CP}$ parameter, respectively. There is thought to be an unknown intrinsic alignment fault within the SVD detector. This effect can be estimated by generating MC with and without misalignment and taking the difference as a systematic error. However, similarly as the Δz bias, this error is assumed not to be unique to a decay mode and therefore, the systematic uncertainty can be taken from the measurement of CP violation in the golden mode, $B^0 \to J/\psi\ K^0_{\rm S}$.

- Δt **resolution function** - contributes with 8.88×10^{-2} and 6.05×10^{-2} to the systematic error. The Δt resolution function is parametrized with different parameter values for experimental data and MC. To estimate the systematic effect, we have varied each of the parameters by ± 1 or $\pm 2\sigma$ (data or MC). The maximum difference from ± the error has been taken as a systematic shift. The largest contributions come from the $\mathcal{R}_{\rm det}$ part of the time resolution function.

- **Flavour tagging** - contributes with 0.71×10^{-2} and 0.63×10^{-2} to the systematic error of $\mathcal{S}_{CP}$ and $\mathcal{A}_{CP}$, respectively. The wrong tag fractions and wrong tag fraction differences in each r-bin, w and Δw, have been varied by their respective errors, $\pm 1\sigma$. The parameters including their errors are summarized in Table 3.6.

- **Tag-side interference** - contributes with 2.00×10^{-2} and 1.63×10^{-2} to the systematic error of $\mathcal{S}_{CP}$ and $\mathcal{A}_{CP}$, respectively. Throughout the analysis we have silently neglected the possible interference effect at the tagging side, between CKM favoured amplitude, $b \to c\bar{u}d$, and doubly CKM-suppressed amplitude, $b \to \bar{u}cd$. Such processes in the final state are used for flavour tagging and thus, the interference between them may result in deviations from the assumed time-dependent CP evolution. To account for this effect in terms of a systematic error, we have made use of interference corrections to the time dependent PDF estimated from a $B^0 \to D^* l\nu$ sample, namely $2r' \sin(2\phi_1 + \phi_3 + \delta') = 0.00964 \pm 0.00731$ and $2r' \sin(2\phi_1 + \phi_3 - \delta') = -0.00673 \pm 0.00731$. The strategy has been following, we have generated toy MC using a PDF with the interference effect implemented and afterwards, we have fitted the obtained data with an original PDF (without any interference) and the residual has been taken as a systematic uncertainty. The strength of the effect has been calculated using the $D^* l\nu$ interference corrections, mean values of $\mathcal{S}_{CP}$ and $\mathcal{A}_{CP}$ parameters obtained from the data and world average value of ϕ_3 angle obtained from the CKMFitter group [46]. In order to take into account interference experimental errors, we have made the toy MC ensemble tests several times with all the parameters changed by $\pm 1\sigma$. The maximum residual from all has been taken then as an estimate of the final systematic error. For more details about the tag-side interference see [47], the systematic determining technique is described in the internal Belle note [48].

Summarizing the systematic error studies, the biggest contributions to the CP violating parameters uncertainties come from the Δt fit component, namely from the Δt resolution function and vertex quality selection criteria. In the future, these errors can be reduced to the level of other systematic errors, as soon as we increase the number of signal events by adding more η_c decay channels to the analysis chain and thus, eliminate the statistical fluctuations in the final data model.

7.4 Summary

The measurement of branching ratio and CP violating parameters has provided following results:

$$\mathcal{B} = (0.59 \pm 0.07_{\text{stat}} \pm 0.01_{\text{syst}}) \times 10^{-6} \quad (7.2)$$

$$\mathcal{S}_{CP} = 0.68^{+0.38}_{-0.46} \pm 0.13_{\text{syst}} \quad (7.3)$$

$$\mathcal{A}_{CP} = 0.00^{+0.23}_{-0.31} \pm 0.08_{\text{syst}}, \quad (7.4)$$

Relative sys. error	$\mathcal{B}$ [%]	$\mathcal{S}_{CP}$ [10^{-2}]	$\mathcal{A}_{CP}$ [10^{-2}]
$\delta_{N_{B\bar{B}}}$	1.37	–	–
δ_{Tracking}	0.70	–	–
$\delta_{\text{K}^0_\text{S}\text{ reconstruction}}$	0.82	–	–
$\delta_{\text{Proton PID}}$	–	–	–
$\delta_{\mathcal{CS}}$	–	–	–
$\delta_{\text{Model shape}}$	1.22	3.96	2.38
$\delta_{\text{PDG values}}$	1.01	1.23	0.24
$\delta_{\text{Fit bias}}$	0.73	0.30	0.56
$\delta_{\text{Interference}}$	–	–	–
$\delta_{M_{\text{bc}}}$	–	–	–
$\delta_{\text{IP profile}}$	–	2.24	1.21
$\delta_{\text{Track helix errors}}$	–	–	–
$\delta_{\text{VTX quality}}$	–	7.26	7.20
$\delta_{B_{\text{tag}}\text{ selection}}$	–	4.19	3.40
$\delta_{\Delta t\text{ range}}$	–	0.08	0.12
$\delta_{\Delta z\text{ bias}}$	–	0.39	0.50
$\delta_{\text{SVD misalignment}}$	–	0.24	0.41
$\delta_{\Delta t\text{ resol. function}}$	–	8.88	6.05
$\delta_{\text{Flavour tagging}}$	–	0.71	0.63
$\delta_{\text{Tag side interference}}$	–	2.00	1.63
δ_{Total}	2.47	13.27	7.67

Tab. 7.2: Systematic uncertainties in measurement of branching ratio and CP violating parameters in: $B^0 \to \eta_c K^0_S$, $\eta_c \to p\bar{p}$. Relative errors are listed for branching ratio measurement, absolute values for CP violating parameters.

The statistical correlation coefficients between $\mathcal{S}_{CP}$, $\mathcal{A}_{CP}$ and signal/background yields are given in Table 7.3.

[%]	$N_{\text{sig SVD1}}$	$N_{\text{bkg SVD1}}$	$N_{\text{sig SVD2}}$	$N_{\text{bkg SVD2}}$	$\mathcal{S}_{CP}$	$\mathcal{A}_{CP}$
$N_{\text{sig SVD1}}$	+100					
$N_{\text{bkg SVD1}}$	-20.3	+100				
$N_{\text{sig SVD2}}$	-0.01	+0.01	+100			
$N_{\text{bkg SVD2}}$	+0.01	-0.01	-24.5	+100		
$\mathcal{S}_{CP}$	+0.09	-0.10	-3.92	+3.32	+100	
$\mathcal{A}_{CP}$	-0.49	+0.56	+1.79	+1.52	-8.50	+100

Tab. 7.3: Statistical correlation matrix (in percent) for the fit results.

In order to estimate the statistical significance of CP violation for $\mathcal{S}_{CP}$ parameter, we have performed a likelihood scan. This procedure involves repeating the minimisation for fixed values of this parameter over the range $[0, 1]$ and taking the statistical significance as $\sqrt{-2\log(\mathcal{L}_0/\mathcal{L}_{\text{max}})}$, where $\mathcal{L}_{\text{max}}$ represents the best likelihood value and $\mathcal{L}_0$ the likelihood with $\mathcal{S}_{CP}$ parameter fixed to zero. In conclusion, the statistical significance of CP violation is found to be 1.5σ as seen in Fig. 7.5 and the result is consistent with the current world average [18], which reads $\sin 2\phi_1 = 0.679 \pm 0.020$ $(0.018_{\text{stat-only}})$.

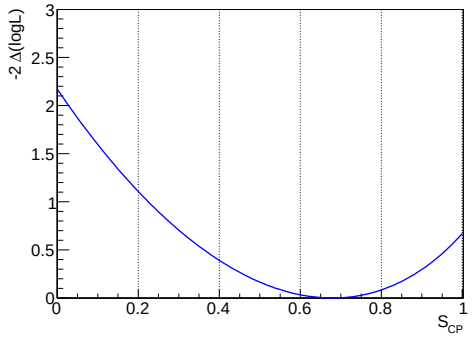

Fig. 7.5: Likelihood scan of $\mathcal{S}_{CP}$ parameter, where the likelihood accounts for statistical fluctuations only.

The CP violation parameter $\mathcal{A}_{CP}$ is found to be consistent within 1σ with zero value, which implies that there is no observed direct CP violation

in $b \to c\bar{c}s$ decay with pseudo-scalar particle in the final state. This result is consistent with the current world average [18], which is $\mathcal{A}_{CP} = 0.005 \pm 0.017$ $(0.012_{\text{stat-only}})$.

Comparing the branching ratio with a world average value (PDG value), $\mathcal{B}_{\text{PDG}} = (8.3 \pm 1.2) \times 0.5 \times (1.41 \pm 0.17) \times 10^{-7} \equiv (0.59 \pm 0.11) \times 10^{-6}$, the fit result is in a perfect agreement with the PDG value.

8 Conclusions and Outlook

In this part of the thesis we have presented a measurement of CP violating parameters in $B^0 \to \eta_c K^0_S$, $\eta_c \to p\bar{p}$, which at quark level can be schematically expressed as a measurement of $b \to c\bar{c}s$ transition with a pseudo-scalar $c\bar{c}$ resonance in the final state. According to the theoretical predictions calculated within the Standard model [15], one of the CP parameters, namely $\mathcal{S}_{CP}$, can be directly expressed in terms of the weak angle, ϕ_1, one of the angles of CKM unitarity triangle. The corresponding relation reads: $\mathcal{S}_{\mathcal{CP}} = -\xi \sin 2\phi_1$, where $\xi = -1(+1)$ for a CP-odd (CP-even) final state. The theoretical uncertainty, or more precisely, the difference between the measured ("effective") value and theoretical value, $\sin 2\phi_1$, is estimated to be less than 1 % [15] . Such a deviation appears due to a presence of penguin diagram with u quark in the loop and its different weak phase, compared to that of a dominant tree graph. Let us stress that for B decay with a pseudo-scalar η_c resonance observed together with K^0_S in the final state, we have expected to obtain $\xi = -1$ and no signs of direct CP violation; i.e. the other CP parameter, $\mathcal{A}_{CP}$, has been expected to be consistent with zero. The measurement has brought following results:

$$\mathcal{S}_{CP} = 0.68^{+0.38}_{-0.46} \pm 0.13_{\text{syst}} \tag{8.1}$$

$$\mathcal{A}_{CP} = 0.00^{+0.23}_{-0.31} \pm 0.08_{\text{syst}}, \tag{8.2}$$

These results are fully consistent with the current world average values, see the summary of the most precise measurements by B-factories in Figure 8.1. The statistical significance of $\mathcal{S}_{\mathcal{CP}}$ is found to be 1.5σ, as seen in Fig. 7.5, and the CP violation parameter $\mathcal{A}_{CP}$ is found to be consistent within 1σ with zero value. That implies that there is no observed direct CP violation in $b \to c\bar{c}s$ decay with a pseudo-scalar particle in the final state. Moreover, as already pointed out, the measured value of $\sin 2\phi_1$ has a correct sign of $+1$.

In comparison with previous Belle measurement [17], and currently the most precise measurement in this mode by BaBar experiment [12], we have come up with a different analysis approach, where the best B candidate has been chosen based on the best M_{bc} value and not the best χ^2 of the η_c vertex constrained fit. This method has its pros and cons, and the main motivation

has arisen from a possible physics bias, which might occur if the best B candidate based on the best η_c vertex fit were used. Let us recall the known fact that the CP measurement is based on the fit to proper-time difference, which is calculated from precisely determined B vertices, and that's exactly the point. The $B_{\rm rec}$ vertex is estimated as a vertex of $p\bar{p}$ tracks, i.e. η_c resonance, and as such should not be used in the B candidate selection method. The disadvantage of such an approach appears in the observation of different number of signal candidates in η_c and ΔE distributions. For $\eta_c \to p\bar{p}$ the difference can be safely neglected, but not for $\eta_c \to K^0_S K^{\pm}\pi^{\mp}$ and $\eta_c \to K^+K^-\pi^0$. This approach makes their data model more complex.

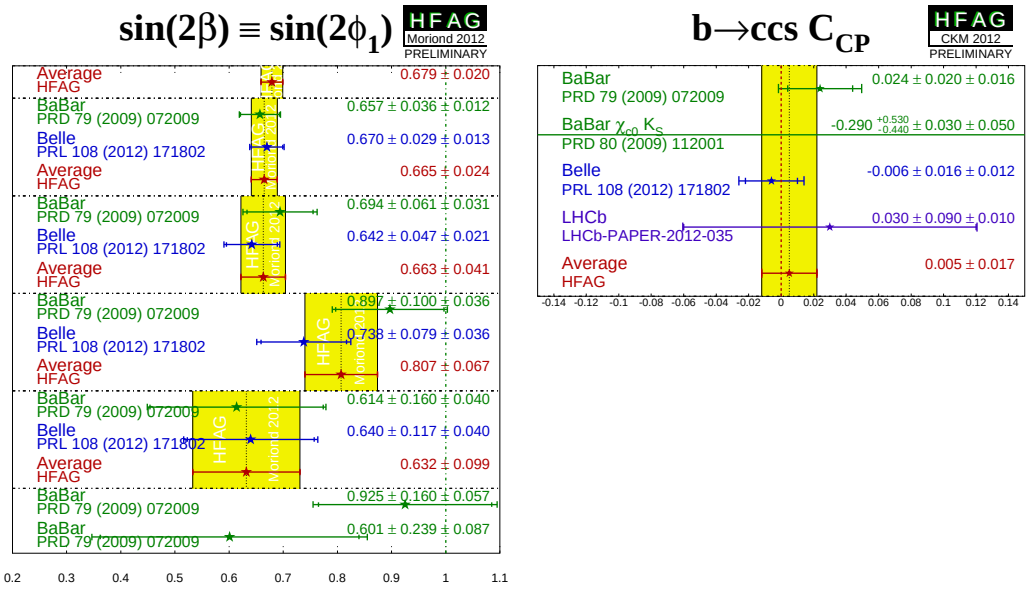

Fig. 8.1: Current average of $\sin 2\phi_1 \equiv \mathcal{S}_{CP}$ (left) and $C \equiv -\mathcal{A}_{CP}$ (right) from B-factories [18]. The left plot lists the following B decay measurements: world average with all channels included, $J/\psi K^0_S$, $J/\psi K^0_L$, $\psi(2S)K^0_S$, $\chi_{c1}K^0_S$ and $\eta_c K^0_S$, $J/\psi K^{*0}(K^{*0} \to K^0_S\pi^0)$ by BaBar only.

Furthermore, in contrast to previous Belle analysis we have chosen a technically more advanced fitting procedure, in which all physics related parameters: τ_B, $\mathcal{S}_{CP}$ and $\mathcal{A}_{CP}$, have been obtained in a simultaneous 4D unbinned ML fit: $\Delta E \times m_{\eta_c} \times \Delta t \times q$, instead of a previously applied two-step 2D fit procedure. That method was based on a determination of event-by-event signal/background fraction from a 2D fit: $\Delta E \times M_{\rm bc}$ (or m_{η_c}) and subsequently, the physics related parameters were found in a separate lifetime fit: $\Delta t \times q$. The disadvantage of the latter approach arose when the systematic effects

were calculated. All parameters together with r-bin fractions determined in $\Delta E \times M_{\rm bc}$ (or $m_{\eta_{\rm c}}$) fit had to remain fixed in the lifetime fit. On the other hand, the new method let us leave some parameters released, e.g. r-bin fractions, and thus, no related systematic effects have to be taken into account. In addition, a simultaneous multidimensional fit has brought another advantage, it helps reveal an incorrect description of observed data in the data model (or from the opposite side it confirms a correct and full description of signal and background components in the model), especially when this method applies to a high statistics control data sample. If some of the components is/are incorrectly modelled, the branching ratio measurement differs when using a 2D fit model instead of full 4D fit model. In conclusion, for $\eta_{\rm c} \to p\bar{p}$ decay the statistics in the corresponding data sample has been found rather low and both approaches brought the same results. We expect to have more precise results with the new method when a combined fit of all $\eta_{\rm c}$ decay channels: $\eta_{\rm c} \to K^0_{\rm S} K^{\pm}\pi^{\mp}$, $\eta_{\rm c} \to K^+K^-\pi^0$ and $\eta_{\rm c} \to p\bar{p}$ is performed.

In order to cross-check our method with a previous approach and simultaneously check consistency of the overall fitting method, we have performed a CP violation measurement in the control sample: $B^{\pm} \to \eta_{\rm c} K^{\pm}$, $\eta_c \to p\bar{p}$. As expected, both $\mathcal{S}_{CP}$ and $\mathcal{A}_{CP}$ parameters have been found statistically consistent with zero value:

$$\mathcal{S}_{CP} = -0.011 \pm 0.160_{\rm stat} \quad (8.3)$$

$$\mathcal{A}_{CP} = +0.137 \pm 0.118_{\rm stat}, \quad (8.4)$$

In addition, we have measured the branching ratios in both the neutral and charged B decay, and compared obtained values to the PDG [16]. Our results are expressed as a product of two branching fractions, and within their statistical and systematical errors agree with the world average values:

Measurement:

$$\mathcal{B}(B^0 \to \eta_{\rm c} K^0_{\rm S}) \times \mathcal{B}(\eta_{\rm c} \to p\bar{p}) = (0.59 \pm 0.07_{\rm stat} \pm 0.01_{\rm syst}) \times 10^{-6}$$

$$\mathcal{B}(B^{\pm} \to \eta_{\rm c} K^{\pm}) \times \mathcal{B}(\eta_c \to p\bar{p}) = (1.61 \pm 0.10_{\rm stat} \pm 0.06_{\rm syst}) \times 10^{-6}$$

PDG:

$$\mathcal{B}(B^0 \to \eta_{\rm c} K^0_{\rm S}) \times \mathcal{B}(\eta_{\rm c} \to p\bar{p}) = \tfrac{1}{2} \times (8.3 \pm 1.2) \times (1.41 \pm 0.17) \times 10^{-7}$$

$$\equiv (0.59 \pm 0.11) \times 10^{-6}$$

$$\mathcal{B}(B^{\pm} \to \eta_{\rm c} K^{\pm}) \times \mathcal{B}(\eta_c \to p\bar{p}) = (9.6 \pm 1.2) \times (1.41 \pm 0.17) \times 10^{-7}$$

$$\equiv (1.35 \pm 0.23) \times 10^{-6}.$$

Finally, in terms of statistical error and experimental precision, our measurement of CP violation parameters in the $b \to c\bar{c}s$ transition with a pseudoscalar $c\bar{c}$ resonance in the final state can't be still regarded as comparable

to that by BaBar experiment. Nevertheless, the BaBar result was obtained from a measurement of the $\eta_c \to K^0_S K^\pm \pi^\mp$ decay channel, which is statistically larger, and they used a different strategy, see above explanation, Figure 8.1 and the result compared to the world average [18]:

$$\mathcal{S}_{CP}(\text{BaBar}) = 0.925 \pm 0.160_{\text{stat}} \pm 0.057_{\text{syst}} \quad (8.5)$$

$$\mathcal{S}_{CP}(\text{World Avg}) = 0.679 \pm 0.020\ (0.018_{\text{stat-only}}) \quad (8.6)$$

With our approach, several issues appeared in $\eta_c \to K^0_S K^\pm \pi^\mp$ analysis and that's why our method had to be first verified on a relatively clean decay with a high detection efficiency: $\eta_c \to p\bar{p}$. The specific issues in $\eta_c \to K^0_S K^\pm \pi^\mp$ concerned the different number of signal events in ΔE and m_{η_c} distributions, which had to be modelled with a signal Monte Carlo taking carefully into account the nature of η_c three-body decay. Moreover, several peaking background sources with resonant structure appeared and had to be modelled via several specific signal Monte Carlos. This analysis is currently ongoing, and we expect to have 5.44 % detection efficiency in SVD1 and 8.41 % efficiency in SVD2, which will roughly bring 6.2 times more signal data to a combined fitter with $\eta_c \to p\bar{p}$ decay and thus, we might expect to have a measurement precision in $\mathcal{S}_{CP}$ parameter at the level $\delta(\mathcal{S}_{CP}) \sim 0.150 - 0.180$. Such a result will then be comparable to that by BaBar.

For illustration, all measurements of $\sin 2\phi_1$ obtained until now by different experiments (and averaged over several decay modes as measured by specified experiment) are shown in Figure 8.2.

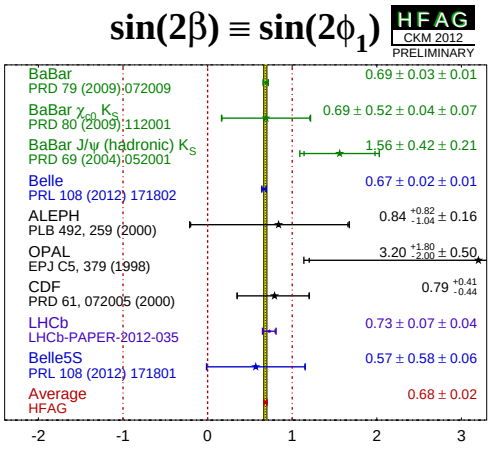

Fig. 8.2: Current average of $\sin 2\phi_1 \equiv \mathcal{S}_{CP}$ from all experiments [18].

A Flavour Tagging

A proper identification of B^0 flavour or in other words, of the charge of corresponding b quark, is necessary to be able to observe the effects of CP violation in B^0 physics, via e.g. a typical observable - raw B^0 asymmetry:

$$\frac{N(B^0) - N(\bar{B}^0)}{N(B^0) + N(\bar{B}^0)}, \tag{A.1}$$

where $N(B^0)$, $N(\bar{B}^0)$ stand for the measured number of B^0 mesons, having a quark content ("charge") $q = \bar{b}$, $q = b$, respectively. Such a procedure is called flavour tagging, and with a perfect detector, the corresponding tagging algorithm would correctly identify the "charge" of every B^0 meson that decays into a flavour specific mode. In reality, only a fraction of all B^0 events are tagged, tagging efficiency is lower than 100 %. In addition, from these B^0 mesons only a few are identified correctly. The fraction of misidentified B^0 mesons is called a wrong tag fraction, w, and plays an important role in the observed time-dependent decay rate as already shown in Eq. (1.1):

$$\begin{aligned} \mathcal{P}(\Delta t, q) \; = & \frac{e^{-|\Delta t|/\tau_{\mathrm{B}^0}}}{4\tau_{\mathrm{B}^0}} \Big\{ (1 - q.\Delta w) + \\ & q(1-2w) \times \Big[\mathcal{S}_{CP} \sin(\Delta m_{\mathrm{d}} \Delta t) + \mathcal{A}_{CP} \cos(\Delta m_{\mathrm{d}} \Delta t) \Big] \Big\} \end{aligned} \tag{A.2}$$

The incorrect flavour assignment is mainly because of particle misidentification. Besides, there also exist non-dominant physics processes, e.g. charged kaon arising from a colour suppressed $b \to c\bar{c}s$, and they give a flavour estimate exactly opposite compared to the dominant processes.

Let us stress that the measured CP violating quantities, $\mathcal{S}_{CP}$ and $\mathcal{A}_{CP}$, are observed right through a term $(1-2w) \equiv r$, see the Eq. A.2, and therefore, the precise determination of w is very important for the analysis. Even if one achieves high tagging efficiency, it starts to be meaningless if the value of w equals to 0.5, because no flavour information is known then.

In this appendix a brief summary of the flavour tagging procedure is provided, more dedicated descriptions can be found in the official Belle paper

[39] or Belle internal document [49]. The values of wrong tag fractions directly used in the analysis have been listed in Tab. 3.6, in dedicated Section 3.1.8.

A.1 Flavour Tagging Algorithm

Once the CP-side, B_{rec}, has been fully reconstructed, all remaining final state particles (tracks), assigned to the other B (denoted as B_{tag}), are used to determine the flavour information. At the lowest level, the B^0 charge, q, can be derived by searching for particular charged tracks, the charge of which would directly correspond to the flavour of B^0 meson. Some physics processes carry the same charge (primary decays of b quark), some the opposite charge (decays of b quark products). To summarize all the relevant physics processes, the following (see Fig. A.1) have been used to determine the B^0 flavour at

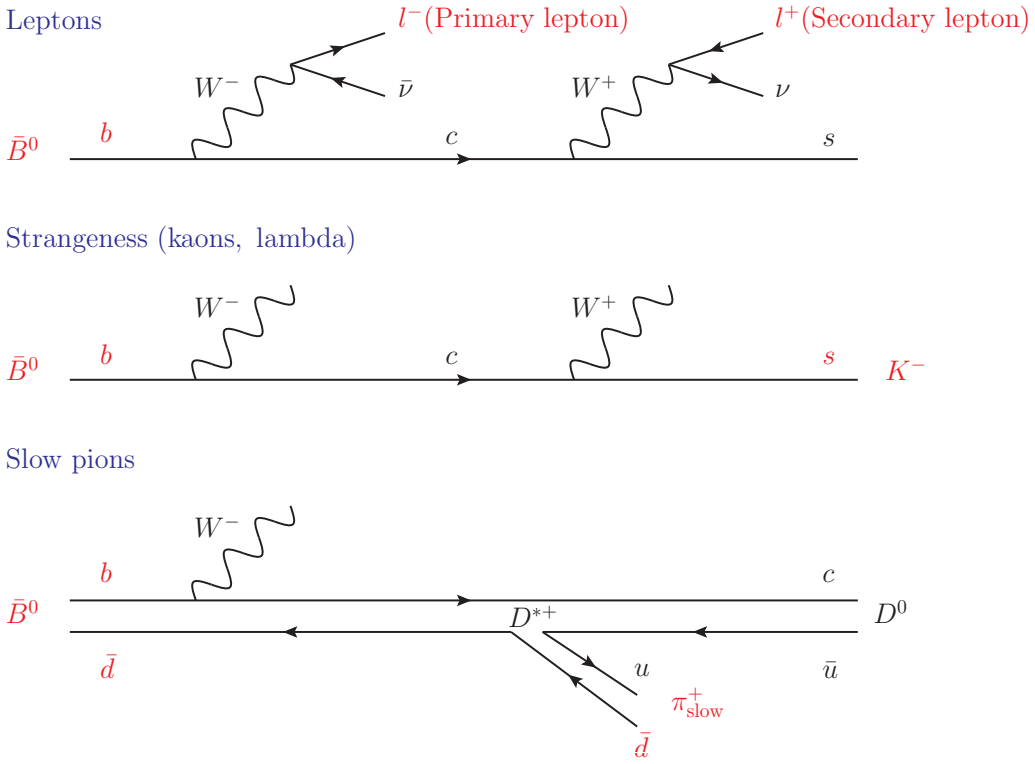

Fig. A.1: Schematic Feynman diagrams for physics processes used in flavour tagging algorithm.

Belle: primary leptons (high-momentum leptons) in decays $b \to c\, l^- \bar{\nu}_l$, sec-

ondary leptons (intermediate momentum leptons) in $b \to c \to l^+\nu_l$, slow pions coming from $B^0 \to D^{*-}\pi^+X$ decays, kaons originating from the cascade $b \to c \to s$ and similarly for Λ baryons.

The Belle tagging procedure consists of two consecutive steps, called layers: track layer and event layer, see a schematic drawing A.2. First, a signature of flavour specific categories in each charged track or in lambda

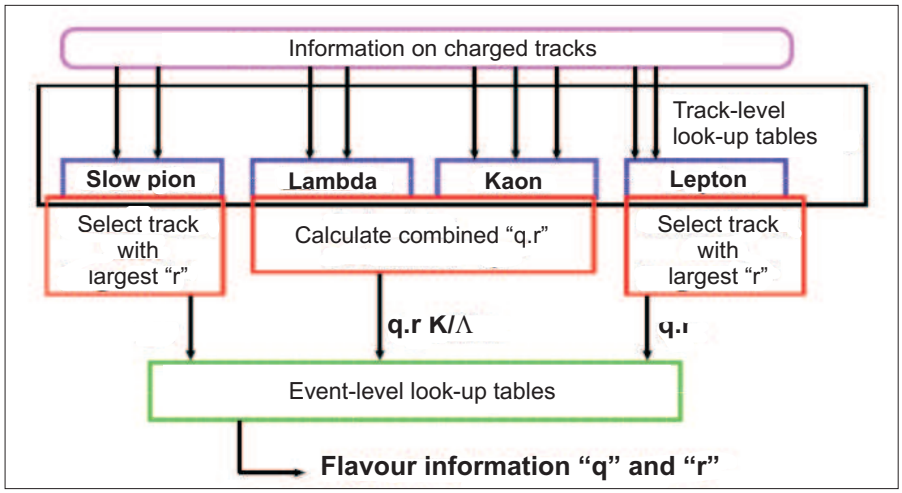

Fig. A.2: Flavour tagging algoritm.

candidates is found. As mentioned above, there are 4 different track-layer categories: leptons, kaons, lambdas and slow pions. Afterwards, based on multiple discriminants (as e.g. kinematic variables, PID information, ...), these flavour specific candidates are utilized to determine the B^0 flavour. As a method, a multi-dimensional likelihood look-up tables binned by the values of individual discriminants are used. Clearly, the flavour tagging method doesn't always return a correct flavour and thus, the dilution factor r has been introduced:

$$q.r = \frac{N(B^0) - N(\bar{B}^0)}{N(B^0) + N(\bar{B}^0)}, \tag{A.3}$$

It ranges from $r = 0$ (for no flavour determination) to $r = 1$ (for unambiguous determination) and its value has been determined from MC simulations. The variables $N(B^0)$, $N(\bar{B}^0)$ stand for the measured number of B, $\bar{B}$ events, respectively, in each "bin" of the look-up table.

The second layer, event-layer, combines the track results, $(q.r)_i$, together, where i represents the tagging category for each track. The main goal is to determine a single highest $q.r$ output for each event. For the lepton and slow pion categories, the track with the highest r value in each category is chosen.

For the kaon and Λ categories, the flavour and dilution factors of each track are combined. The main reason is to account for the cases, when events with multiple s quarks in the final state occur. In the end, the event-layer provides a three-dimensional look-up table, where the correlations between the flavour information for the four track categories are correctly taken into account.

As an example, let us describe this procedure for the lepton category [50]. This category is intended to accept high and middle momentum leptons together with fast pions. All tracks are required to have the CMS momentum, $p^* > 400\,\mathrm{MeV}/c$. Moreover, the category consists of two sub-categories according to the lepton flavour. Once the likelihood ratio of $e^{\pm}/K^{\pm}$ is greater than 0.8, the track is categorized into electron sub-category. On the other hand, the track with larger likelihood ratio of $\mu^{\pm}/K^{\pm}$ than 0.95 is passed to muon sub-category. Since the quality of lepton identification highly depends on the track polar angle, θ_{lab}, the angle is also examined. The fast leptons are considered to come from the semileptonic B decays, the middle momentum from the semileptonic D decays. The discrimination of fast leptons from the middle momentum is done using p^*, recoil mass (M_{recoil}) and missing momentum in the CMS (p^*_{miss}). The recoil mass is defined as the invariant mass made up by all B_{tag} tracks except for this lepton. The final look-up table has been constructed from the multi-dimensional likelihood using the p^*, lepton likelihood, $\cos\theta_{\mathrm{lab}}$, M_{recoil}, p_{miss} and lepton charge. The numbers of bins for each discriminant are 11, 4, 6, 10, 6, and 2, respectively. Thus, the total number of bins of the look-up table is $11 \times 4 \times 6 \times 10 \times 6 \times 2 = 31680$. For each of these bins, the $q.r$ value obtained from Eq. (A.3) has been assigned. The numbers of B^0 and $\bar{B}^0$ for each bin, and corresponding dilution factor, have been estimated from the Monte Carlo simulations.

A.2 Measurement of Wrong Tag Fractions

Using the MC-determined flavour dilution factor r as a measure of the tagging quality is a straightforward way of how to directly take into account correlations among various tagging discriminants. On the other hand, let us note that r equals to $(1-2w)$ only if the MC perfectly represents the data. To correct for MC imperfections, events have been divided into 7 r-bin regions: $0 < r \leq 0.1$, $0.1 < r \leq 0.25$, $0.25 < r \leq 0.5$, $0.5 < r \leq 0.625$, $0.625 < r \leq 0.75$, $0.75 < r \leq 0.875$ and $0.875 < r \leq 1.0$ and for each r-bin, the wrong tag fraction (mistag probability), w, and the difference between the wrong tag probabilities for B^0 and $\bar{B}^0$, Δw, have been obtained by fitting the time-dependent $B^0\bar{B}^0$ mixing oscillations of high statistics self-tagging

data samples: $B^0 \to D^{*-} l^+ \nu_l, D^{(*)-}\pi^+$ and $D^{*-}\rho^+$. These decays are already flavour-specific and thus, one knows their flavours independently on the flavor tagging method. The time evolution of $B^0\bar{B}^0$ pairs with the opposite flavour (OF) and the same flavour (SF) [50] are given by:

$$\mathcal{P}_{\rm OF}(\Delta t) \sim 1 + (1-2w)\cos(\Delta m \Delta t) \quad \text{(A.4)}$$

$$\mathcal{P}_{\rm SF}(\Delta t) \sim 1 - (1-2w)\cos(\Delta m \Delta t), \quad \text{(A.5)}$$

and the corresponding OF-SF asymmetry can be derived as:

$$\frac{\rm OF - SF}{\rm OF + SF} = (1-2w)\cos(\Delta m \Delta t) \quad \text{(A.6)}$$

After the final fit of time-dependent OF-SF asymmetry to the above listed data samples, the data driven values of w that correspond to the given r-bin have been extracted. As a result, one can use in any analysis the data based w values instead of those determined from MC studies.

B Time Resolution Function

The measurement precision of proper-time difference, Δt, can be highly influenced by several factors: vertexing capabilities of Belle experiment, various "parasitic" physics processes which additionally occur and different approximations used in the mathematical description of applied experimental method. Thus, the measured Δt distribution differs in many aspects from the theoretical predictions. Such effects have been naturally incorporated in the physics formula (4.5), referring to $(\Delta t \times q)$ measurement, using a convolution of the functional form given in Eq. (1.1) with a so-called time resolution function, $\mathcal{R}_{B\bar{B}}(\Delta t)$. This resolution function consists of three different components, which will be described in detail here:

1. Effect of detector resolution
2. Effect of non-primary tracks on tag side
3. Effect of kinematic approximation

This appendix explains only the relevant information for this analysis. The corresponding sources have been mainly: the Belle official paper [37], its update given in a Belle internal note [51] and Belle software package, named Tatami [52]. The fit parameters directly used in the analysis have been provided by an ICPV (Indirect CP Violation) working group via a database of the Tatami software package, version `2010mdlh`. For clarity, these parameters will be summarized in several Tables in the last section of this appendix.

B.1 Detector Resolution

The effects of detector resolution have been studied using a special MC, where all short-lived particles ($\tau < 10^{-9}$ s, including K^0_S and Λ particles) are forced to decay with a zero lifetime at the B meson decay points. As a simulation software, the QQ generator [53] and Geant3 framework [25] (to simulate the Belle detector response) have been used. The detailed study of various fits to the simulation results have shown that the obtained distributions can't

be simply expressed as a sum of several Gaussian distributions with a constant standard deviation. Instead, a more elaborate Gaussian function with an event-by-event dependent standard deviation (vertex error in z-direction, σ^z) has to be used. The value of this error is computed from the error matrix of the tracks and IP constraint used in the fit. Since the resolution function differs for multi-track vertices from those reconstructed just from a single track and IP constraint, the resolution function has been studied separately for these two cases: multi-track vertices and single-track vertices.

The detector resolution function for events with a multi-track vertex has been modelled as a single Gaussian:

$$\mathcal{R}^{\text{multi}}_{\text{det}_i}(\delta z_i) = G(\delta z_i, (s^0_i + s^1_i \xi)\sigma^z_i),\ i = \text{rec}, \text{tag} \tag{B.1}$$

On the other hand, for events with a single-track vertex, the resolution function has been expressed as a sum of two Gaussians, one to describe the main part and the other to describe long tails, arising due to poorly reconstructed tracks:

$$\mathcal{R}^{\text{single}}_{\text{det}_i}(\delta z_i) = (1 - f^{\text{tail}})G(\delta z_i, s^{\text{main}}\sigma^z_i) + f^{\text{tail}}G(\delta z_i, s^{\text{tail}}\sigma^z_i),\ i = \text{rec}, \text{tag} \tag{B.2}$$

In the above equations, δz has been defined as a difference in z-position between the reconstructed and generated vertex (or in other words, between the reconstructed and expected z-position); s^0_i, s^1_i represent free parameters for multi-track vertices, different for SVD1 and SVD2 experiment and for reconstructed and tagged B; f^{tail}, s^{main} and s^{tail} are free parameters for single-track vertices, different for SVD1 and SVD2 experiment but the same for reconstructed or tagged B. The vertex quality, ξ, and the vertex error in z direction, σ^z, represent event dependent quantities. It's interesting to note that the correlation between the detector resolution function width , $s^{\text{main}}_i \equiv (s^0_i + s^1_i \xi)\sigma^z_i$, and the event-by-event vertex resolution in z, σ^z_i, is corrected with a linear polynomial using vertex quality ξ, see Eq. (B.1).

Using the MC simulations it has been found that the standard χ^2 quantity (quality of a vertex fit) is correlated with the B decay length due to the tight IP constraint in transverse direction. For this reason, a new quantity characterizing vertex quality, ξ, using z information only, has been constructed[a]:

$$\xi \equiv \frac{1}{2n}\sum_i^n [(z^i_{\text{after}} - z^i_{\text{before}})/\varepsilon^i]^2, \tag{B.3}$$

where n is the number of tracks used in the fit; z^i_{before} and z^i_{after} are the z-positions of each track before and after the vertex fit, respectively; and $\varepsilon^i_{\text{before}}$

[a] ξ can be defined for multi-track vertices only

is the error of $z^i_{\rm before}$. Such a quantity ξ basically represents a projection of χ^2 into the z-direction.

B.2 Smearing Due to Non-primary Tracks

The next term of time resolution function, $\mathcal{R}_{\rm np}$, reflects the smearing effect on reconstructed z-position of the tag side vertex. The smearing occurs mainly due to inclusion of particle tracks coming from the secondary vertices, i.e. tracks not directly originating from the associated $B_{\rm tag}$ vertex but instead, from vertices of its decay products. These vertices are displaced from the primary vertex due to the finite lifetime of secondary particles.

In order to cover such effects, the resolution function has been expressed as a sum of prompt component given by Dirac delta distribution, $\delta^{\rm Dirac}(\delta z_{\rm tag})$, and components that account for smearing from $K^0_{\rm S}$ and charm decays:

$$\begin{aligned}\mathcal{R}_{\rm np}(\delta z_{\rm tag}) \; &= f_\delta \delta^{\rm Dirac}(\delta z_{\rm tag}) + \\ &(1-f_\delta)[f_{\rm p}E_{\rm p}(\delta z_{\rm tag},\tau^{\rm p}_{\rm np}) + (1-f_{\rm p})E_{\rm n}(\delta z_{\rm tag},\tau^{\rm n}_{\rm np})]\end{aligned} \tag{B.4}$$

Here, f_δ stands for a fraction of prompt component. The non-prompt part is described as a sum of two terms: $f_{\rm p}E_{\rm p}(\delta z_{\rm tag},\tau^{\rm p}_{\rm np})$, $(1-f_{\rm p})E_{\rm n}(\delta z_{\rm tag},\tau^{\rm n}_{\rm np})$; with $f_{\rm p}$ being the fraction of the term with $\delta z_{\rm tag} > 0$ and $E_{\rm p}$, $E_{\rm n}$ representing a positive, negative exponential, respectively:

$$E_{\rm p}(\delta z_{\rm tag},\tau^{\rm p}_{\rm np}) = \frac{1}{\tau^{\rm p}_{\rm np}}\exp(-\frac{\delta z_{\rm tag}}{\tau^{\rm p}_{\rm np}}),\ \text{for } \delta z_{\rm tag} > 0,\ \text{otherwise } 0 \tag{B.5}$$

$$E_{\rm n}(\delta z_{\rm tag},\tau^{\rm n}_{\rm np}) = \frac{1}{\tau^{\rm n}_{\rm np}}\exp(+\frac{\delta z_{\rm tag}}{\tau^{\rm n}_{\rm np}}),\ \text{for } \delta z_{\rm tag} \le 0,\ \text{otherwise } 0 \tag{B.6}$$

The overall functional form of non-prompt component has been found from the difference between results obtained from nominal MC studies and special MC in which all short-lived secondary particles were forced to decay promptly. Because of necessity for different approach for single and multi-track vertices, two functional forms for lifetime, $\tau^{\rm n,p}_{\rm np}$, have been defined. For multi-track vertices a multilinear relation in ξ and σ^z has been used:

$$\tau^i_{\rm np} = [\tau^0_i + \tau^1_i(\sigma^z_{\rm tag}/c(\beta\gamma)_\Upsilon) + \tau^2_i\xi + \tau^3_i\xi(\sigma^z_{\rm tag}/c(\beta\gamma)_\Upsilon)]s^{\rm global}_{\rm np},\ \ i = {\rm p,n}, \tag{B.7}$$

where $(\beta\gamma)_\Upsilon$ stands for the boost of $\Upsilon(4S)$ system, τ^0_i, τ^1_i, τ^2_i and τ^3_i are free parameters and $s^{\rm global}_{\rm np}$ represents a global $\mathcal{R}_{\rm np}$ parameter. For single track vertices no ξ information is available, thus the following parametrization is used:

$$(\tau^i_{\rm np}) = [\tau^0_i + \tau^1_i\sigma^z_{\rm tag}/c(\beta\gamma)_\Upsilon]s^{\rm global}_{\rm np} \tag{B.8}$$

Here, τ_i^0, τ_i^1 represent free parameters and $s_{np}^{\rm global}$ the global $\mathcal{R}_{\rm np}$ parameter.

Finally, to account for the dependence of f_δ on ξ and σ^z and simultaneously utilize the information whether or not a flavour tagging lepton exists in the vertex reconstruction tracks, a following multilinear form is used for f_δ. This form applies only to events with multi-track vertices:

$$f_\delta = [1 - f_{\rm np}^{\rm mlt}][f^0_{\delta(l/nl)} + f^1_\delta(\sigma^z_{\rm tag}/c(\beta\gamma)_\Upsilon) + f^2_\delta\xi + f^3_\delta\xi(\sigma^z_{\rm tag}/c(\beta\gamma)_\Upsilon)], \quad \text{(B.9)}$$

where $f^0_{\delta(l/nl)}$, f^1_δ, f^2_δ, f^3_δ and $f_{\rm np}^{\rm mlt}$ are free parameters. There exist two different values for $f^0_{\delta(l/nl)}$, one for events with a flavour tagging lepton in the vertex reconstruction tracks, l (a narrower distribution), the other for events without the lepton, nl. For single-track vertices only one parameter, f_δ, is simply used, no functional form has been applied.

Using $f_{\rm np}^{\rm mlt}$ and the relation for f_δ, one gets the last formula, namely for $f_{\rm p}$ as:

$$f_{\rm p} = [1 - f_{\rm np}^{\rm mlt}][1 - f^0_{\delta(l/nl)} + f^1_\delta(\sigma^z_{\rm tag}/c(\beta\gamma)_\Upsilon) + f^2_\delta\xi + f^3_\delta\xi(\sigma^z_{\rm tag}/c(\beta\gamma)_\Upsilon)]/[1 - f_\delta] \quad \text{(B.10)}$$

B.3 Kinematic Approximation

Throughout the analysis, the proper time interval, Δt, is defined via a relation (3.8), which is only true if motion of B meson in the CMS (centre of mass system) is neglected. The difference (correction) between Δt and true value can be calculated using relativistic kinematics of $\Upsilon(4S)$ system as:

$$\begin{aligned} x &\equiv \Delta t - \Delta t_{\rm true} \\ &= (z_{\rm rec} - z_{\rm tag})/c(\beta\gamma)_\Upsilon - (t_{\rm rec} - t_{\rm tag}) \\ &= (t_{\rm rec}c(\beta\gamma)_{\rm rec} - t_{\rm tag}c(\beta\gamma)_{\rm tag})/c(\beta\gamma)_\Upsilon - (t_{\rm rec} - t_{\rm tag}) \\ &= [(\beta\gamma)_{\rm rec}/(\beta\gamma)_\Upsilon - 1]t_{\rm rec} - [(\beta\gamma)_{\rm tag}/(\beta\gamma)_\Upsilon - 1]t_{\rm tag}, \quad \text{(B.11)} \end{aligned}$$

where $(\beta\gamma)_{\rm rec}$, $(\beta\gamma)_{\rm tag}$ represent Lorentz boost of reconstructed, tagged B, respectively. Their ratio to $(\beta\gamma)_\Upsilon$ is given as:

$$\begin{aligned} (\beta\gamma)_{\rm rec,\,tag} &= \frac{E_B^{\rm CMS}}{m_B c^2} \pm \frac{p_B^{\rm CMS}\cos\vartheta^{\rm CMS}}{(\beta)_\Upsilon m_B c} \equiv a_k \pm c_k \quad \text{(B.12)} \\ &\simeq 1 \pm 0.165\cos\vartheta^{\rm CMS}. \quad \text{(B.13)} \end{aligned}$$

Here, a positive and negative sign stand for the reconstructed and tagged B, respectively; $E_B^{\rm CMS}$, $p_B^{\rm CMS}$, $\cos\vartheta^{\rm CMS}$, m_B and c for B energy, momentum,

polar angle in the CMS, mass and velocity of light, respectively. The numerical evaluation has been obtained using following approximate values: $\beta_\Upsilon \sim 0.391/c$, $E_B^{\mathrm{CMS}} \sim 5.292$ GeV and $p_B^{\mathrm{CMS}} \sim 340$ MeV/c. As a result one obtains the difference (correction), x, as:

$$x = 0.165 \cos\vartheta^{\mathrm{CMS}}(t_{\mathrm{rec}} + t_{\mathrm{tag}}). \tag{B.14}$$

After considering that t_{rec} and t_{tag} follow an exponential distribution:

$$E_{\mathrm{p}}(t_i,\ \tau_B) = 1/\tau_B \exp(-t_i/\tau_B), \quad i = \mathrm{rec},\ \mathrm{tag} \tag{B.15}$$

and simultaneously, taking into accound that the last contribution to time resolution function accounting for kinematic approximation is given as a conditional probability density of getting x and Δt_{true} at the same time given Δt_{true}, one comes to the final expression for the last term of time resolution function:

$$\mathcal{R}_{\mathrm{k}}(x) = \mathcal{P}(x, \Delta t_{\mathrm{true}})/\mathcal{P}(\Delta t_{\mathrm{true}}) \tag{B.16}$$

After evaluation one obtains the final relation:

$$\mathcal{R}_{\mathrm{k}}(x) = \begin{cases} E_{\mathrm{p}}(x - \{(a_k - 1)\Delta t_{\mathrm{true}} + c_k|\Delta t_{\mathrm{true}}|\}, |c_k|\tau_B) & \text{for } c_k > 0 \\ \delta^{\mathrm{Dirac}}(x - (a_k - 1)\Delta t_{\mathrm{true}}) & \text{for } c_k = 0 \\ E_{\mathrm{n}}(x - \{(a_k - 1)\Delta t_{\mathrm{true}} + c_k|\Delta t_{\mathrm{true}}|\}, |c_k|\tau_B) & \text{for } c_k < 0 \end{cases} \tag{B.17}$$

B.4 Total Time Resolution Function

The total time resolution function, $\mathcal{R}_{B\bar{B}}$, is given as a convolution of four individual components: detector resolution for reconstructed B, detector resolution for tagged B, additional smearing due to non-primary tracks on the tag side and kinematic approximation that B mesons are at rest in the CMS of $\Upsilon(4S)$ resonance; $\mathcal{R}_{B\bar{B}}$ follows as:

$$\mathcal{R}_{B\bar{B}} = \mathcal{R}_{\mathrm{det_{rec}}} \otimes \mathcal{R}_{\mathrm{det_{tag}}} \otimes \mathcal{R}_{\mathrm{np}} \otimes \mathcal{R}_{\mathrm{k}} \tag{B.18}$$

The individual components have been described in previous sections.

B.5 Summary of Parameters

The parameters provided via the database of Tatami software package and used during the data analysis in the time resolution function and defining outliers in the Eq. (4.5) have been summarized, for lucidity, in the following

Tables: B.1 (detector resolution), B.2 (outliers), B.3 and B.4 (smearing due to non-primary tracks for the charged and neutral mode, respectively). Let us stress that these parameters have been determined in independent physics studies within an ICPV group, namely in lifetime fits to the data using various high statistics control samples. The set of parameters given here corresponds to the version of tatami database denoted as `2010mdlh`.

Parameter	**Vertexing**	**SVD1 Value**	**SVD2 Value**
$s^0_{\rm rec}$	Multi-track	$0.70^{+0.19}_{-0.11}$	$0.81^{+0.27}_{-0.15}$
$s^1_{\rm rec}$		$0.21^{+0.04}_{-0.05}$	$0.23^{+0.07}_{-0.05}$
$s^0_{\rm tag}$		$0.48^{+0.28}_{-0.08}$	$0.64^{+0.39}_{-0.07}$
$s^1_{\rm tag}$		$0.24^{+0.04}_{-0.06}$	$0.23^{+0.03}_{-0.05}$
$s^{\rm main}$	Single-track	$0.98^{+0.28}_{-0.04}$	$1.01^{+0.44}_{-0.04}$
$f^{\rm tail}$		–	$0.11^{+0.02}_{-0.04}$
$s^{\rm tail}$		–	$3.66^{+3.61}_{-0.39}$

Tab. B.1: Parameters used in $\mathcal{R}_{\rm det}$ part of time resolution function for single and multi-track vertices; SVD1 and SVD2 experiments.

Parameter	**Vertexing**	**SVD1 Value**	**SVD2 Value**
$\sigma_{\rm ol}$	Global	$43.7^{+15.0}_{-13.4}$	$33.5^{+1.6}_{-9.2}$
$f^{\rm mlt}_{\rm ol}$	Multi-track	$0.037^{+0.025}_{-0.011}$	$0.027^{+0.002}_{-0.005}$
$f^{\rm sng}_{\rm ol}$	Single-track	$0.00011^{+0.00014}_{-0.00007}$	$0.00015^{+0.00007}_{-0.00007}$

Tab. B.2: Parameters of outlier component defined in Eq. (4.5).

Parameter	**Vertexing**	**SVD1 Value**	**SVD2 Value**
$s_{\rm np}^{\rm global}$	Global	$+1.06^{+0.12}_{-0.17}$	$+1.01^{+0.08}_{-0.16}$
$f_\delta^0({\rm nl})$	Multi-track	$+0.41^{+0.04}_{-0.04}$	$+0.53^{+0.01}_{-0.01}$
$f_\delta^0({\rm l})$		$+0.61^{+0.04}_{-0.04}$	$+0.71^{+0.01}_{-0.01}$
f_δ^1		$+0.31^{+0.07}_{-0.07}$	$+0.19^{+0.03}_{-0.03}$
f_δ^2		$-0.18^{+0.02}_{-0.02}$	$-0.19^{+0.01}_{-0.01}$
f_δ^3		$+0.20^{+0.03}_{-0.03}$	$+0.23^{+0.01}_{-0.01}$
$f_{\rm np}^{\rm mlt}$		$+0.14^{+0.01}_{-0.01}$	$+0.12^{+0.01}_{-0.01}$
$\tau_{\rm p}^0$		$-0.007^{+0.013}_{-0.012}$	$+0.024^{+0.004}_{-0.004}$
$\tau_{\rm p}^1$		$+0.647^{+0.032}_{-0.032}$	$+0.741^{+0.017}_{-0.017}$
$\tau_{\rm p}^2$		$-0.028^{+0.005}_{-0.005}$	$-0.020^{+0.002}_{-0.002}$
$\tau_{\rm p}^3$		$+0.242^{+0.013}_{-0.013}$	$+0.275^{+0.007}_{-0.006}$
$\tau_{\rm n}^0$		$-0.040^{+0.020}_{-0.020}$	$+0.066^{+0.007}_{-0.007}$
$\tau_{\rm n}^1$		$+0.605^{+0.050}_{-0.049}$	$+0.524^{+0.026}_{-0.026}$
$\tau_{\rm n}^2$		$-0.038^{+0.010}_{-0.010}$	$-0.019^{+0.004}_{-0.004}$
$\tau_{\rm n}^3$		$+0.337^{+0.027}_{-0.026}$	$+0.331^{+0.014}_{-0.013}$
f_δ	Single-track	$+0.83^{+0.01}_{-0.01}$	$+0.81^{+0.01}_{-0.01}$
$f_{\rm p}$		$+0.85^{+0.02}_{-0.02}$	$+0.83^{+0.04}_{-0.04}$
$\tau_{\rm p}^0$		$+1.42^{+0.08}_{-0.08}$	$+0.99^{+0.04}_{-0.04}$
$\tau_{\rm p}^1$		–	–
$\tau_{\rm n}^0$		$+1.98^{+0.29}_{-0.26}$	$+0.43^{+0.09}_{-0.08}$
$\tau_{\rm n}^1$		–	–

Tab. B.3: Parameters used in $\mathcal{R}_{\rm np}$ for $B^\pm$ decays. Different parameters are provided for multi, single-track vertices and SVD1, SVD2 experiments.

Parameter	**Vertexing**	**SVD1 Value**	**SVD2 Value**
$s_{\rm np}^{\rm global}$	Global	$+1.06^{+0.12}_{-0.17}$	$+1.01^{+0.08}_{-0.16}$
$f_\delta^0({\rm nl})$	Multi-track	$+0.47^{+0.04}_{-0.04}$	$+0.56^{+0.01}_{-0.01}$
$f_\delta^0({\rm l})$		$+0.64^{+0.04}_{-0.04}$	$+0.75^{+0.01}_{-0.01}$
f_δ^1		$+0.27^{+0.07}_{-0.07}$	$+0.16^{+0.03}_{-0.03}$
f_δ^2		$-0.22^{+0.02}_{-0.02}$	$-0.20^{+0.01}_{-0.01}$
f_δ^3		$+0.22^{+0.03}_{-0.03}$	$+0.23^{+0.01}_{-0.01}$
$f_{\rm np}^{\rm mlt}$		$+0.12^{+0.02}_{-0.01}$	$+0.12^{+0.01}_{-0.01}$
$\tau_{\rm p}^0$		$-0.005^{+0.015}_{-0.015}$	$+0.039^{+0.006}_{-0.005}$
$\tau_{\rm p}^1$		$+0.717^{+0.039}_{-0.039}$	$+0.765^{+0.020}_{-0.021}$
$\tau_{\rm p}^2$		$-0.030^{+0.005}_{-0.005}$	$-0.026^{+0.002}_{-0.002}$
$\tau_{\rm p}^3$		$+0.251^{+0.014}_{-0.014}$	$+0.321^{+0.007}_{-0.007}$
$\tau_{\rm n}^0$		$+0.045^{+0.027}_{-0.027}$	$+0.083^{+0.009}_{-0.009}$
$\tau_{\rm n}^1$		$+0.515^{+0.064}_{-0.063}$	$+0.534^{+0.031}_{-0.031}$
$\tau_{\rm n}^2$		$-0.078^{+0.013}_{-0.013}$	$-0.030^{+0.004}_{-0.004}$
$\tau_{\rm n}^3$		$+0.430^{+0.034}_{-0.033}$	$+0.390^{+0.016}_{-0.016}$
f_δ	Single-track	$+0.78^{+0.01}_{-0.01}$	$+0.77^{+0.08}_{-0.01}$
$f_{\rm p}$		$+0.82^{+0.02}_{-0.02}$	$+0.80^{+0.02}_{-0.02}$
$\tau_{\rm p}^0$		$+1.85^{+0.09}_{-0.08}$	$+1.63^{+0.05}_{-0.05}$
$\tau_{\rm p}^1$		–	–
$\tau_{\rm n}^0$		$+2.04^{+0.28}_{-0.24}$	$+0.92^{+0.08}_{-0.08}$
$\tau_{\rm n}^1$		–	–

Tab. B.4: Parameters used in $\mathcal{R}_{\rm np}$ for B^0 decays. Different parameters are provided for multi, single-track vertices and SVD1, SVD2 experiments.

C Summary of Fit Parameters

This appendix summarizes all fit parameters used in the data model. Two various sets are listed here, one for the control sample, see Table C.1, the other for the neutral mode, see Table C.2. Since the data model significantly differs for SVD1 and SVD2 experiments, the two parameter sets, in addition, consist of two experiment-oriented subsets – with different values for SVD1 and SVD2, respectively.

In order to make clear, which parameters and from which data samples are fixed in the final data fit or which parameters remain free, an extra abbreviations have been introduced in the above defined Tables: MC for parameters fixed from the signal MC, BB for parameters fixed from the $B\bar{B}$ generic MC, SB for parameters fixed from the Belle side-band data, CS for parameters fixed from the control sample, PDG for parameters fixed from the PDG [16] or HFAG [18] and F for parameters that remain free in the final fit. If a parameter has not been used at all, a dash mark "–" is used instead.

Parameter	Free/Fixed	SVD1 Value	SVD2 Value
SVD1, SVD2-specific			
$\mu_{\text{main}}(\Delta E)$	MC	$+0.0013 \pm 0.0007$	$+0.0002 \pm 0.0006$
$\mu^{\text{CF}}_{\text{main}}(\Delta E)$	F	-0.0013 ± 0.0013	-0.0013 ± 0.0008
$\sigma_{\text{main}}(\Delta E)$	MC	$+0.0087 \pm 0.0018$	$+0.0090 \pm 0.0009$
$\sigma^{\text{CF}}_{\text{main}}(\Delta E)$	F	$+1.02 \pm 0.13$	$+1.10 \pm 0.08$
$\mu^{1}_{\text{tail}}(\Delta E)$	MC	-0.0016 ± 0.0049	$+0.0031 \pm 0.0036$
$\sigma^{1}_{\text{tail}}(\Delta E)$	MC	$+1.69 \pm 0.94$	$+1.81 \pm 0.62$
$f_1(\Delta E)$	MC	$+0.208 \pm 0.444$	$+0.178 \pm 0.186$
$\mu^{2}_{\text{tail}}(\Delta E)$	MC	-0.0114 ± 0.0063	-0.0100 ± 0.0129
$\sigma^{2}_{\text{tail}}(\Delta E)$	MC	$+4.65 \pm 0.98$	$+5.28 \pm 1.65$
$f_2(\Delta E)$	MC	$+0.106 \pm 0.052$	$+0.058 \pm 0.031$
M_{η_c} [GeV]	PDG	$+2.9803 \pm 0.0012$	
Γ_{η_c} [GeV]	PDG	$+0.0286 \pm 0.0022$	
μ^{Voigt}	MC	-0.0003 ± 0.0007	-0.0005 ± 0.0007
$\sigma^{\text{Voigt}}_{\text{main}}$	MC	$+0.0057 \pm 0.0020$	$+0.0059 \pm 0.0018$
$\sigma^{CF\,\text{Voigt}}_{\text{main}}$	–	1.0	
$\sigma^{\text{Voigt}}_{\text{tail}}$	MC	$+8.20 \pm 5.05$	$+9.64 \pm 11.84$
$f(\text{Voigt})$	MC	$+0.083 \pm 0.072$	$+0.041 \pm 0.058$
$k_{\text{corr}}(m_{\eta_c})$	MC	$+0.058 \pm 0.015$	$+0.056 \pm 0.013$
τ_{bkg} [ps]	SB	$+0.903 \pm 0.176$	$+0.546 \pm 0.067$
f_δ	SB	$+0.635 \pm 0.129$	$+0.390 \pm 0.087$
μ_δ	SB	$+0.010 \pm 0.064$	0.013 ± 0.036
$f^{\text{tail}}_{\text{bkg sngl}}$	SB	$+0.012 \pm 0.007$	$+0.070 \pm 0.018$
$\mu_{\text{bkg sngl}}$	SB	0.162 ± 0.161	0.013 ± 0.035
$s^{\text{main}}_{\text{bkg sngl}}$	SB	$+1.20 \pm 0.10$	$+1.22 \pm 0.05$
$s^{\text{tail}}_{\text{bkg sngl}}$	SB	$+12.51 \pm 4.02$	$+5.64 \pm 0.66$
$f^{\text{tail}}_{\text{bkg mult}}$	SB	$+0.562 \pm 0.337$	$+0.182 \pm 0.086$
$\mu_{\text{bkg mult}}$	SB	0.494 ± 0.424	0.044 ± 0.095
$s^{\text{main}}_{\text{bkg mult}}$	SB	$+0.689 \pm 0.324$	$+1.08 \pm 0.10$
$s^{\text{tail}}_{\text{bkg mult}}$	SB	$+2.23 \pm 0.78$	$+2.62 \pm 0.43$
$f^{\Delta t}_{\text{bkg}}$	F	$+0.849 \pm 0.106$	$+0.719 \pm 0.043$

Table continues on the next page ...

Parameter	Free/Fixed	SVD1 Value	SVD2 Value
$c^1(\Delta E)$	F	-0.042 ± 0.156	-0.066 ± 0.062
$c^1(m_{\eta_c})$	F	-0.363 ± 0.160	-0.181 ± 0.061
$\tilde{f}^0_{\rm sig}$ (r-bin)	MC	$+0.570 \pm 0.042$	$+0.547 \pm 0.041$
$\tilde{f}^1_{\rm sig}$ (r-bin)	MC	$+0.494 \pm 0.030$	$+0.518 \pm 0.028$
$\tilde{f}^2_{\rm sig}$ (r-bin)	MC	$+0.271 \pm 0.023$	$+0.276 \pm 0.022$
$\tilde{f}^3_{\rm sig}$ (r-bin)	MC	$+0.248 \pm 0.019$	$+0.259 \pm 0.018$
$\tilde{f}^4_{\rm sig}$ (r-bin)	MC	$+0.303 \pm 0.017$	$+0.289 \pm 0.016$
$\tilde{f}^5_{\rm sig}$ (r-bin)	MC	$+0.154 \pm 0.013$	$+0.153 \pm 0.012$
$\tilde{\eta}^0_{\rm sig}$ (r-bin)	F	$+0.90 \pm 0.28$	$+1.04 \pm 0.14$
$\tilde{\eta}^1_{\rm sig}$ (r-bin)	F	$+0.83 \pm 0.25$	$+0.97 \pm 0.11$
$\tilde{\eta}^2_{\rm sig}$ (r-bin)	F	$+1.17 \pm 0.38$	$+0.97 \pm 0.15$
$\tilde{\eta}^3_{\rm sig}$ (r-bin)	F	$+1.54 \pm 0.31$	$+1.06 \pm 0.13$
$\tilde{\eta}^4_{\rm sig}$ (r-bin)	F	$+1.25 \pm 0.20$	$+0.77 \pm 0.10$
$\tilde{\eta}^5_{\rm sig}$ (r-bin)	F	$+1.35 \pm 0.29$	$+0.89 \pm 0.16$
$\tilde{f}^0_{\rm bkg}$ (r-bin)	F	$+0.321 \pm 0.100$	$+0.482 \pm 0.044$
$\tilde{f}^1_{\rm bkg}$ (r-bin)	F	$+0.469 \pm 0.077$	$+0.493 \pm 0.031$
$\tilde{f}^2_{\rm bkg}$ (r-bin)	F	$+0.326 \pm 0.062$	$+0.235 \pm 0.023$
$\tilde{f}^3_{\rm bkg}$ (r-bin)	F	$+0.142 \pm 0.046$	$+0.237 \pm 0.020$
$\tilde{f}^4_{\rm bkg}$ (r-bin)	F	$+0.300 \pm 0.047$	$+0.278 \pm 0.018$
$\tilde{f}^5_{\rm bkg}$ (r-bin)	F	$+0.142 \pm 0.034$	$+0.178 \pm 0.014$
$N_{\rm sig}$	F	105.84 ± 12.67	359.67 ± 25.18
$N_{\rm bkg}$	F	141.15 ± 13.99	916.34 ± 34.51
Global			
τ [ps]	PDG	$+1.641 \pm 0.008$	
$\mathcal{S}_{CP}$	F	-0.012 ± 0.160	
$\mathcal{A}_{CP}$	F	$+0.137 \pm 0.118$	
$\tau_{\rm eff}$ [ps]	BB	$+1.468 \pm 0.095$	

Tab. C.1: Fit parameters obtained from the control sample.

Parameter	Free/Fixed	SVD1 Value	SVD2 Value
SVD1, SVD2-specific			
$\mu_{\text{main}}(\Delta E)$	MC	$+0.00134 \pm 0.00007$	$+0.00055 \pm 0.00007$
$\mu^{\text{CF}}_{\text{main}}(\Delta E)$	CS	-0.0013 ± 0.0013	-0.0013 ± 0.0008
$\sigma_{\text{main}}(\Delta E)$	MC	$+0.0088 \pm 0.0001$	$+0.0087 \pm 0.0001$
$\sigma^{\text{CF}}_{\text{main}}(\Delta E)$	CS	$+1.02 \pm 0.13$	$+1.10 \pm 0.08$
$\mu^{1}_{\text{tail}}(\Delta E)$	MC	-0.00049 ± 0.00047	$+0.0037 \pm 0.0004$
$\sigma^{1}_{\text{tail}}(\Delta E)$	MC	$+1.88 \pm 0.11$	$+1.99 \pm 0.06$
$f_1(\Delta E)$	MC	$+0.198 \pm 0.026$	$+0.210 \pm 0.016$
$\mu^{2}_{\text{tail}}(\Delta E)$	MC	-0.0099 ± 0.0010	-0.0057 ± 0.0015
$\sigma^{2}_{\text{tail}}(\Delta E)$	MC	$+4.21 \pm 0.13$	$+4.99 \pm 0.21$
$f_2(\Delta E)$	MC	$+0.093 \pm 0.009$	$+0.050 \pm 0.005$
M_{η_c}	PDG	$+2.9803 \pm 0.0012$	
Γ_{η_c}	PDG	$+0.0286 \pm 0.0022$	
μ^{Voigt}	MC	-0.00001 ± 0.00010	-0.00052 ± 0.00008
$\sigma^{\text{Voigt}}_{\text{main}}$	MC	$+0.0059 \pm 0.0003$	$+0.0058 \pm 0.0002$
$\sigma^{CF\,\text{Voigt}}_{\text{main}}$	–	1.0	
$\sigma^{\text{Voigt}}_{\text{tail}}$	MC	$+7.24 \pm 0.73$	$+9.22 \pm 2.17$
$f(\text{Voigt})$	MC	$+0.073 \pm 0.011$	$+0.030 \pm 0.008$
$k_{\text{corr}}(m_{\eta_c})$	MC	$+0.059 \pm 0.002$	$+0.057 \pm 0.002$
τ_{bkg} [ps]	SB	$+1.03 \pm 0.67$	$+1.02 \pm 0.18$
f_δ	SB	$+0.721 \pm 0.230$	$+0.605 \pm 0.122$
μ_δ	SB	$+0.047 \pm 0.131$	0.030 ± 0.060
$f^{\text{tail}}_{\text{bkg sngl}}$	SB	–	$+0.016 \pm 0.008$
$\mu_{\text{bkg sngl}}$	SB	–	$+0.253 \pm 0.180$
$s^{\text{main}}_{\text{bkg sngl}}$	SB	–	$+1.35 \pm 0.11$
$s^{\text{tail}}_{\text{bkg sngl}}$	SB	–	$+15.65 \pm 4.74$
$f^{\text{tail}}_{\text{bkg mult}}$	SB	$+0.079 \pm 0.057$	$+0.137 \pm 0.039$
$\mu_{\text{bkg mult}}$	SB	0.099 ± 0.543	0.419 ± 0.428
$s^{\text{main}}_{\text{bkg mult}}$	SB	$+0.913 \pm 0.145$	$+1.25 \pm 0.12$
$s^{\text{tail}}_{\text{bkg mult}}$	SB	$+8.67 \pm 4.14$	$+9.33 \pm 2.31$
$f^{\Delta t}_{\text{bkg}}$	–	1.0	

Table continues on the next page ...

Parameter	Free/Fixed	SVD1 Value	SVD2 Value
$c^1(\Delta E)$	SB	-0.30 ± 0.16	-0.20 ± 0.06
$c^1(m_{\eta_c})$	SB	-0.29 ± 0.17	-0.02 ± 0.06
$\tilde{f}^0_{\rm sig}$ (r-bin)	MC	$+0.439 \pm 0.003$	$+0.420 \pm 0.003$
$\tilde{f}^1_{\rm sig}$ (r-bin)	MC	$+0.338 \pm 0.003$	$+0.357 \pm 0.002$
$\tilde{f}^2_{\rm sig}$ (r-bin)	MC	$+0.131 \pm 0.002$	$+0.143 \pm 0.002$
$\tilde{f}^3_{\rm sig}$ (r-bin)	MC	$+0.086 \pm 0.001$	$+0.086 \pm 0.001$
$\tilde{f}^4_{\rm sig}$ (r-bin)	MC	$+0.063 \pm 0.001$	$+0.068 \pm 0.001$
$\tilde{f}^5_{\rm sig}$ (r-bin)	MC	$+0.051 \pm 0.001$	$+0.056 \pm 0.001$
$\tilde{\eta}^0_{\rm sig}$ (r-bin)	CS	$+0.90 \pm 0.28$	$+1.04 \pm 0.14$
$\tilde{\eta}^1_{\rm sig}$ (r-bin)	CS	$+0.83 \pm 0.25$	$+0.97 \pm 0.11$
$\tilde{\eta}^2_{\rm sig}$ (r-bin)	CS	$+1.17 \pm 0.38$	$+0.97 \pm 0.15$
$\tilde{\eta}^3_{\rm sig}$ (r-bin)	CS	$+1.54 \pm 0.31$	$+1.06 \pm 0.13$
$\tilde{\eta}^4_{\rm sig}$ (r-bin)	CS	$+1.25 \pm 0.20$	$+0.77 \pm 0.10$
$\tilde{\eta}^5_{\rm sig}$ (r-bin)	CS	$+1.35 \pm 0.29$	$+0.89 \pm 0.16$
$\tilde{f}^0_{\rm bkg}$ (r-bin)	SB	$+0.426 \pm 0.067$	$+0.438 \pm 0.026$
$\tilde{f}^1_{\rm bkg}$ (r-bin)	SB	$+0.289 \pm 0.052$	$+0.349 \pm 0.020$
$\tilde{f}^2_{\rm bkg}$ (r-bin)	SB	$+0.183 \pm 0.040$	$+0.145 \pm 0.014$
$\tilde{f}^3_{\rm bkg}$ (r-bin)	SB	$+0.041 \pm 0.020$	$+0.104 \pm 0.011$
$\tilde{f}^4_{\rm bkg}$ (r-bin)	SB	$+0.067 \pm 0.025$	$+0.077 \pm 0.010$
$\tilde{f}^5_{\rm bkg}$ (r-bin)	SB	$+0.010 \pm 0.009$	$+0.022 \pm 0.005$
$N_{\rm sig}$	F	24.38 ± 5.45	86.75 ± 11.05
$N_{\rm bkg}$	F	17.61 ± 4.79	135.30 ± 13.07
Global			
τ [ps]	PDG	$+1.519 \pm 0.007$	
$\mathcal{S}_{CP}$	F	$+0.680 \pm 0.429$	
$\mathcal{A}_{CP}$	F	$+0.001 \pm 0.306$	
$\tau_{\rm eff}$ [ps]	–	–	

Tab. C.2: Fit parameters obtained from the measurement of CP asymmetries in the neutral mode.

Part II

Belle II Optimisation Studies

9 Introduction II

The successful asymmetric e^+e^- collider machine, KEKB, is now being upgraded to a new SuperB flavour factory called SuperKEKB [5, 54], located in the same tunnel of the High Energy Accelerator Research Organization in Tsukuba Japan. By fall 2014 the SuperKEKB will start its operation at $\Upsilon(4S)$ center-of-mass energy with electrons being accelerated to 7.0 GeV, positrons to 4.0 GeV. The targeted instantaneous luminosity will be $8 \times 10^{35}\,\mathrm{cm}^{-2}\mathrm{s}^{-1}$. The main goal of the project, driven mostly by flavour physics precision measurements, is to significantly increase statistics of previous machine by a factor of 40, and simultaneously, deliver to Belle II, an upgrade of its experiment predecessor Belle, an integrated luminosity of $50\,\mathrm{ab}^{-1}$. Such a large data sample will provide physicists with a unique tool for investigation of various extensions to the Standard model physics, namely through precision measurements in the B, charm and τ sectors [55]. Moreover, compared to hadron colliders, SuperKEKB will provide us with a clean and low background environment, where the data can be used to perform various inclusive measurements and also to detect final states with multiple missing particles.

A new solution providing such extreme values of instantaneous luminosity was first proposed for the SuperB factory in Italy [56, 57] and consists in a successful adoption of a so-called nano-beam option. This scheme requires several conditions to be fulfilled: a relatively large horizontal crossing angle at the IP (83 mrad), extremely small horizontal emittances and extremely small horizontal beta functions at the interaction point for both beams. In addition, new superconducting quadrupole magnets located close to the beam collision point will be installed in order to squeeze the vertical beta function at the IP [5]. All these changes, in the end, naturally lead to very focused beams in their cross sections at the interaction region ($\sim$ tens of nanometres), and thus, significantly reduce electron/positron currents needed for the planned head-on-head collision rate. On the other hand, the requirement on extremely high luminosity, leading to acquisition of large data statistics, has its side effects. It's accompanied by a significant increase in background level, with a Touschek effect (intra-beam scattering) being a dominant component.

In order to exploit all these conditions together with a requirement on high-precision measurement of particle decay vertices, a completely new vertex detector (VXD) is necessary. Especially, the following two factors has played a crucial role in its proposal: first, detector operation capabilities under increased level of particle background, and second, high sensitivity to low momenta particles. From this prospective only a vertex detector consisting of a low material budget sensors, providing true 2D position information and located as close as possible to the interaction point, can fulfill such conditions. Therefore, compared to Belle, installation of pixel detectors within the VXD is a must. The Belle II vertex detector [5, 58] will consist of 2 layers of 75 µm thick Depfet based pixel detectors (PXD) and 4 barrel layers of 320 µm thick double-sided silicon micro-strip sensors (SVD), complemented with 3 forward layers.

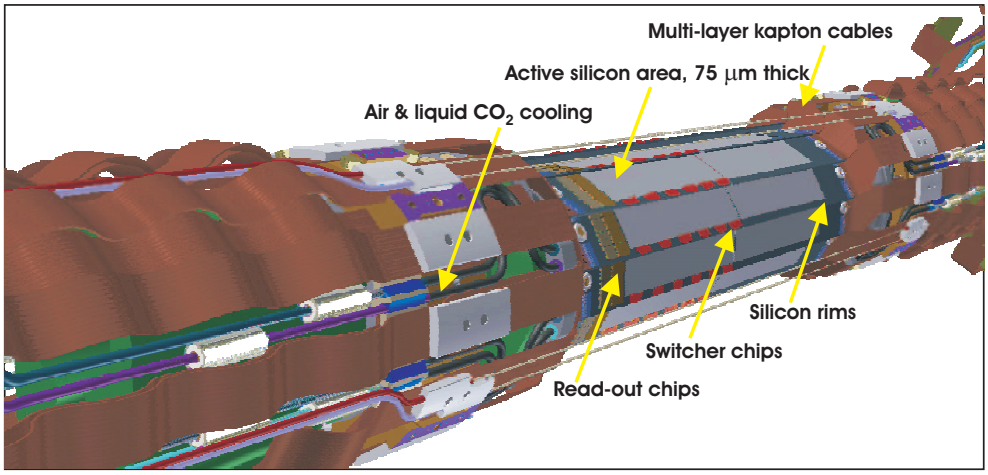

Fig. 9.1: Belle II PXD mechanical design.

The PXD, with its 40 sensors, will read out a total of 7.68 million pixels and will be positioned in two layers, at radii 14 and 22 mm, respectively, from the interaction point. The beam pipe, which represents a main limitation to the positioning of PXD has an outer radius of 12 mm. In order to reduce the amount of silicon material in the sensitive area, the PXD sensors are thinned down to 75 µm, except for its silicon rims providing PXD with a necessary mechanical stability. These rims remain 450 µm thick. The detection area is covered by Depfet-type pixels, the sizes of which did represent one of the key parameters to be determined in optimization studies. The PXD mechanical design is depicted in Figure 9.1[a]; together with active sensors,

[a]Courtesy of Karlheinz Ackermann, Max-Planck Institute München, Germany.

applied electronics (switch and read-out chips), necessary air & liquid CO_2 cooling and support structures are clearly shown.

In order to provide sufficient space for the PXD, the SVD is positioned further from the IP. It will consist of 4 layers, installed at 38, 80, 105 and 135 mm, and in contrast to the PXD, the fourth, fifth and sixth layer will be complemented with slanted V-shaped like sensors in the forward region. Rotation of these sensors with respect to the beam axis will be 11.9, 16.0 and 21.1 degrees, respectively. The detailed description of SVD mechanical structure can be found elsewhere [5][b], but for clarity, let us describe several key components here. Each SVD layer is designed to consist of several ladders, each of which is built of individual double-sided micro-strip sensors: 2, 3, 4 and 5, in the third, fourth, fifth and sixth layer, respectively (see Fig. 9.2[c]). To provide sufficient stability, these sensors are glued together on two

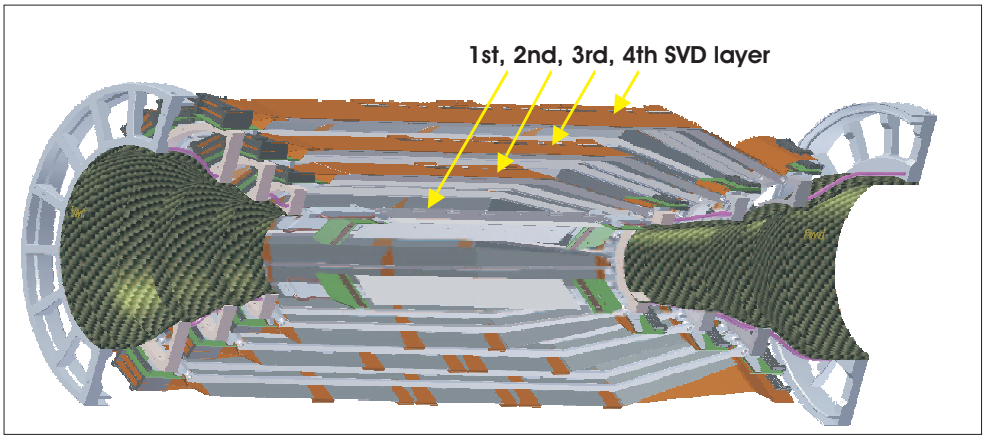

Fig. 9.2: Belle II SVD mechanical design, with a beam pipe and PXD being cut out for clarity. The read-out boards are shown in green colour, kaptons in brown and the endrings (especially distinctive for the sixth layer) in grey.

composite sandwich carbon fiber ribs, where the filling between the two ribs is made of a low mass, but rigid foam. The read-out of the SVD is designed in two ways: the sensors in the central part of each ladder use a so-called origami chip-on-sensor concept, the outer sensors are read out using read-out boards located outside of the acceptance area. The origami concept can be in a simplified way described as follows: the chips reading both sensor sides are placed on a single flexible circuit, mounted on the top of the sensor. The strips at the top are connected by a pitch adapter, whereas the strips

[b] All parameters given here are updated with their actual values compared to those given in [5, 58].

[c] Courtesy of Karlheinz Ackermann, Max-Planck Institute München, Germany.

at the bottom (reading out the other coordinate) are attached by a small flexible fan-out, wrapped around the edge of the sensor. In order to demonstrate a complexity of the origami concept a following Figure 9.3 shows its scheme, together with a main source of passive material in the SVD active region depicted: a stainless steal cooling pipe (liquid CO_2 cooling). The outer diameter of the cooling pipe is 1.5 mm, its wall is 50 µm thick. Full SVD ladders are fixed on stainless steel endrings (see Fig. 9.2), which in addition, provide necessary cooling for the readout boards. Finally, the read-out pitch, expressed as R-$\Phi \times Z$ coordinates, is 50×160 µm for the third layer and 75×240 µm for other 3 layers. Let us stress that the read-out pitch is a factor of 2 times bigger than the physical strip-to-strip pitch, so every second channel is read-out in reality. The V-shaped like sensors provide pitch in a range from $50 - 75$ µm in R-Φ direction and 240 µm in Z.

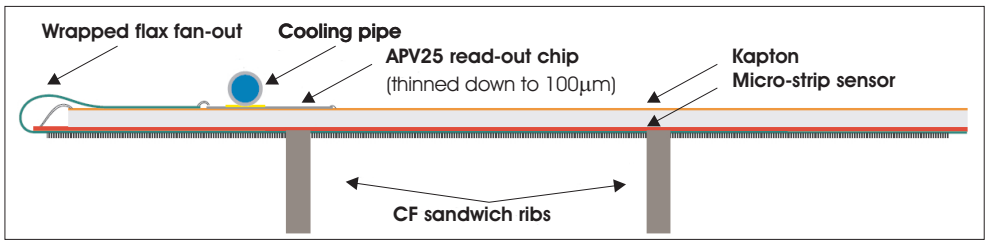

Fig. 9.3: Cross section of origami chip-on-sensor concept [5].

During the design phase of such a complex detection system the collaboration has been facing several technological solutions on one hand and requirements on expected physics performance on the other. To answer which configuration provides the best solution, we've effectively used Monte Carlo (MC) simulations, into which we provided several scenarios and based on the physics results, we've decided for the most suitable solution. Due to our previous experience in the ILC software framework [59], we have utilized its modular design and used it in full MC simulations for multi-parameter studies. The key parameters for optimization have been PXD/SVD material budget, pixel/strip layout configurations, PXD/SVD geometry layout. Finally, we have determined what impact parameter resolution, compared to Belle vertex detector, can be expected for the Belle II VXD. Before these studies have been performed a necessary development of simulation software had to be done. Particularly, the software simulating response of individual silicon pixel/micro-strip detectors to charged/gamma particles (so-called digitization) has been crucial. Our approach to the digitization, including all details connected with a simulation of particle passage through material environment in Geant4 framework [60, 61], can be found in the next Chap-

ter 10. The multi-parameter optimization studies together with the most important results for the VXD final configuration are given in Chapter 11.

For illustration the "simplified" geometry of the VXD as implemented for optimization studies in the Geant4 software, digitization and track reconstruction is depicted in Figures 9.4 (PXD, beam-pipe + PXD + SVD) and 9.5 (beam-pipe + VXD + central drift chamber).

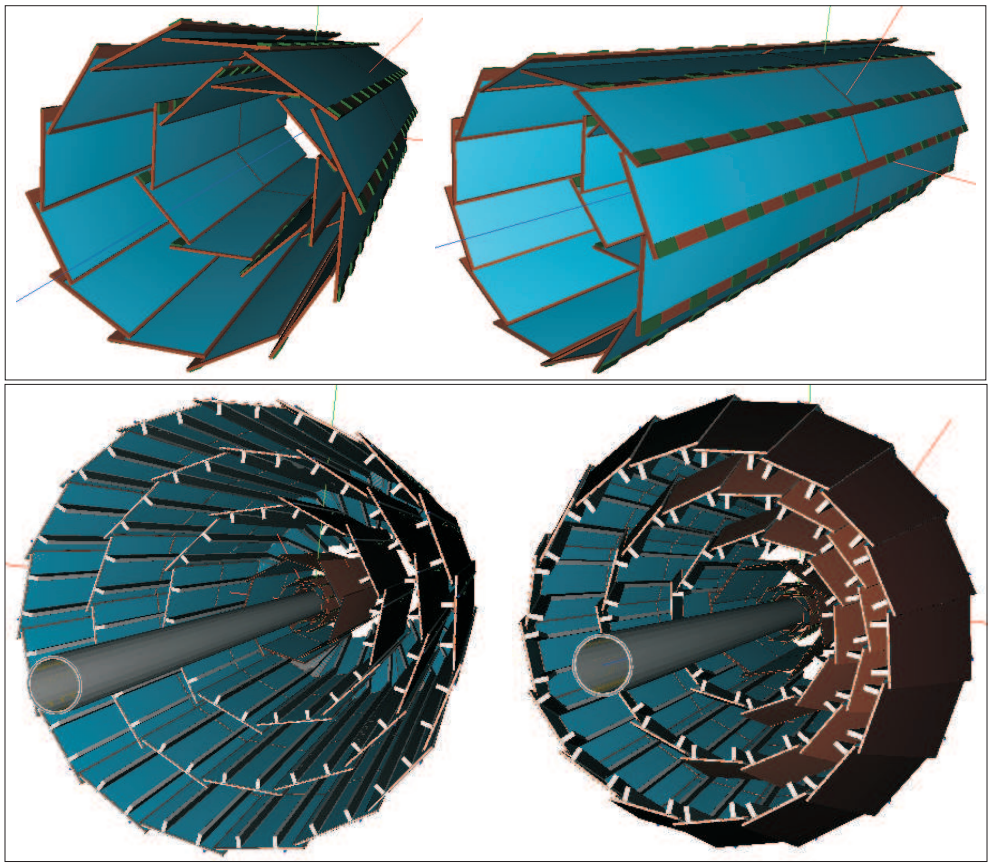

Fig. 9.4: Geant4 model used in MC simulation studies: PXD (top), beam pipe and VXD (bottom: left - backward region, right - forward region).

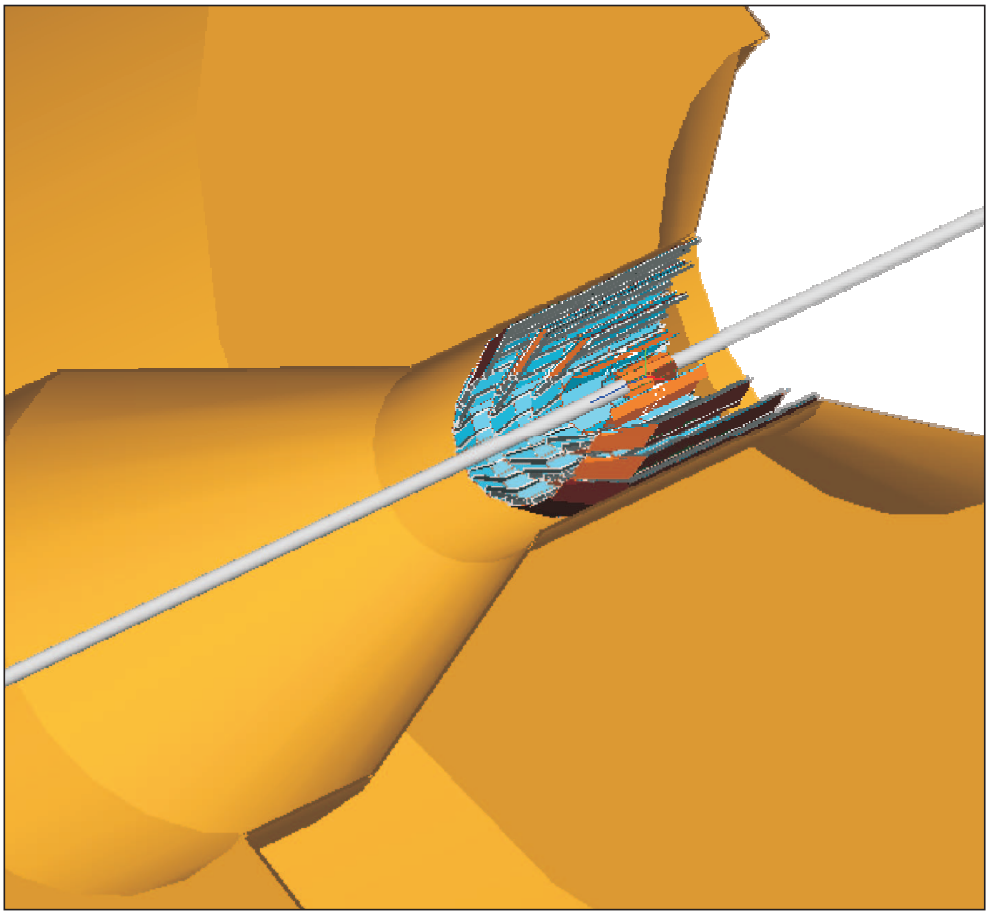

Fig. 9.5: Geant4 model used in MC simulation studies: cross section of a Belle II tracker, including beam pipe, PXD, SVD and central drift chamber. The high energy electron beam (boost) directs from the right to the left.

PROCEEDINGS OF SCIENCE

Silicon Simulation Code for Belle II and ILC

Zbynek DRASAL[*†]
Charles University Prague, Czech Republic
E-mail: drasal@ipnp.troja.mff.cuni.cz

Kolja PROTHMANN[‡]
MPI München, Germany
E-mail: kolja@mpp.mpg.de

Benjamin SCHWENKER[§]
Georg-August-Universität Göttingen, Germany
E-mail: benjamin.schwenker@phys.uni-goettingen.de

Monte Carlo simulations in high-energy physics experiments face the non-trivial task of simulating realistically the response of individual detector components, while keeping the costs in terms of CPU time reasonably low. Such simulation procedures are called digitization and have to incorporate detector physics in as much detail as possible, while performing fast enough. Here, we present our approach to the simulation of the Belle II vertex detector (VXD) using the ILC software framework. We simulate the response of DEPFET (DEPleted Field Effect Transistor) pixel detectors (PXD) and double-sided silicon micro-strip detectors (SVD) in the presence of a magnetic field. To achieve sufficient performance, we use a combination of fast numerical techniques and reasonable simplification of in-detector physics. The simulation itself is divided into 3 steps: particle propagation through matter (using Geant4 with a detailed implementation of the VXD geometry), charge collection in the silicon detectors (digitization) and clustering. The second and third steps are performed in separate reconstruction modules – Marlin modules: SiPxlDigi (pixel detectors) and SiStripDigi (micro-strip detectors). The following physics processes are considered: continuous energy loss fluctuations, generation of e-h pairs, drift in electric field, diffusion, Lorentz shift, mutual crosstalk (strips), read-out/geometric pitch effect (strips), electronics/digital noise. The clustering procedure is based on the center-of-gravity and analog head-tail algorithms. All effects have been studied and compared to test beam data in order to validate the algorithms and to determine the relative importance of individual processes.

The 20th Anniversary International Workshop on Vertex Detectors - VERTEX 2011
June 19 - 24, 2011
Rust, Lake Neusiedl, Austria

[*]Speaker.

[†]This work has been supported by the Czech Science Foundation Grant No. 203/10/0777 and the Ministry of Education, Youth and Sports of the Czech Republic No. LA10033 and MSM0021620859.

[‡]This work has been supported by the DFG cluster of excellence "Origin and Structure of the Universe" of Germany.

[§]This work has been supported by the Volkswagen Foundation.

PoS(Vertex 2011)027

1. Introduction

SuperKEKB, an upgrade of the successful asymmetric e^+e^- collider and current world luminosity record holder ($2.11 \times 10^{34}\,cm^{-2}s^{-1}$) KEKB (Tsukuba, Japan), is foreseen by fall 2014 [1]. The main goal of the new Super Flavour Factory is to dramatically increase statistics by a factor of 40 and thus deliver an integrated luminosity of $50\,ab^{-1}$ by end of 2021. For this reason, the nano-beam option has been chosen, which, as a side effect, leads to a significant increase in background level, with Touschek effect being a dominant component. To exploit the new conditions and provide high-precision measurements of the decay vertex of B meson systems, a new Belle II silicon vertex detector will be operated. Due to the increased background level and required sensitivity to low momenta particles, a low material budget pixel detector closest to the interaction point is a must. Belle II VXD will consist of 2 layers of 75 µm thick DEPFET-type pixel detectors and 4 barrel layers of 320 µm thick double-sided strip detectors, complemented with 3 forward layers. Precise and fast silicon (Si) simulations are absolutely necessary to optimize such a detector.

2. Software Framework

Due to its convenient modular design (Fig. 1) and sufficient flexibility, a software framework for ILC (International Linear Collider) [2] has been adopted to the special needs of Belle II experiment and new software packages: SiPxlDigi and SiStripDigi have been developed. The framework

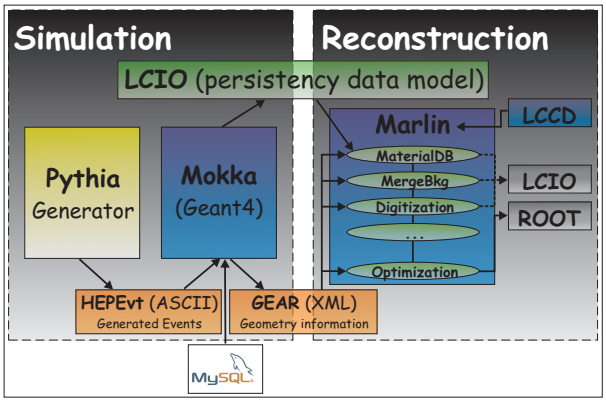

Figure 1: Scheme of ILC software framework

itself provides a typical chain of high energy physics tools: generator (Pythia), simulation (Mokka – Geant4 based toolkit), digitization (Marlin modules: SiPxlDigi & SiStripDigi), reconstruction (Marlin module: SiTracking and other modules) and analysis. As the geometry information is required with different level of detail throughout the chain, two different interfaces are provided. An interface to access a MySQL database at Geant4 level (with full detail of detector geometry) and a GEAR interface at reconstruction level (with limited geometry description provided via XML). The data model, which is used to describe the event data throughout the chain, is based on the LCIO persistency framework. It provides all necessary structures (C++ objects) to store data produced in silicon simulation: simulated hits (SimTrackerHits) $\rightarrow$ digits (TrackerPulses) $\rightarrow$ hits (TrackerHits), etc. All data types hold the relation to MC truth information (MCParticle).

3. Silicon Simulation & Geant4 Toolkit

Several specific issues closely related to Geant4 will be addressed in this section. The first issue is the right choice of a suitable physics model describing continuous energy loss fluctuations for ionizing particles traversing a silicon detector. Years ago, when Geant3 (Fortran-based predecessor of Geant4) was used, we noticed that the default model (denoted as `G3Landau`) didn't provide correct distributions of dE/dx for thin material (typically 10–100 μm of Si absorber). The main limitation is that, in the Landau model, the typical energy loss in the absorber should be large compared to the binding energy of the most tightly bound electron, which was not fullfilled in thin silicon sheets. The more accurate Photo-Absorption Ionisation (PAI) model, which takes into account the atomic structure of the absorber, provided accurate description of measured data, but with more CPU needed. For details see [3].

Similarly, Geant4 comes with several different models. The `G4UniversalFluctuations` model is used by default. It is based on a simplified model of atoms with two energy levels, and an atom-particle interaction that can either be an excitation, with energy loss E_1 or E_2, or ionisation, distributed according to $1/E^2$ distribution [4]. If this data description is not sufficient enough, one can use the `G4PAIModel` instead. In order to validate the physics model, two detailed simulations in Geant3 and Geant4, with 8 GeV/c pions traversing 290 μm thick silicon bulk have been performed and compared to real data cited in [5]. The results are shown in Fig. 2 and summarized in Table 1. The discrepancy between the Geant4 simulation (using either two-levels atom model or PAI model) and the experimental data is reasonably small.

	G3 Landau	**G3 PAI**	**G4 Universal**	**G4 PAI**	**Experiment**
MPV $\left\langle \frac{dE}{dx} \right\rangle$ [keV]	96 ± 1	79 ± 1	84 ± 1	81 ± 1	79.43
FWHM w [keV]	20 ± 1	29 ± 1	30 ± 1	30 ± 1	29.24

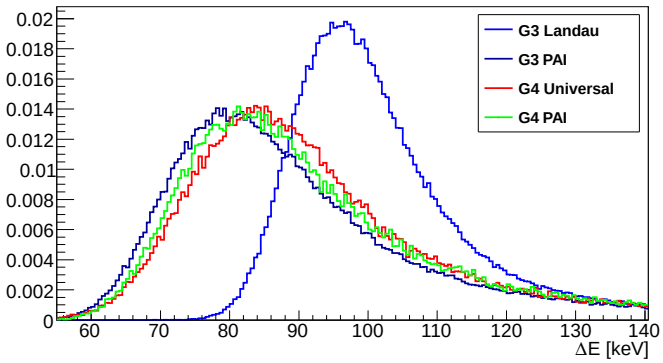

Figure 2: and **Table 1:** Energy loss distributions of 8 GeV/c pions in 290 μm thick silicon for different Geant3 and Geant4 models. MPV stands for the most probable value and depends on material thickness, etc.

Another issue is the correct setting of a Geant4 production threshold cut, which has strong impact on the number of generated δ–electrons. The optimal choice of the cut defines a compromise between the spatial precision of the simulation and the total number of generated particles. Generally speaking, if the kinetic energy of a secondary electron is below the threshold cut, no soft

secondary particle is generated and the transferred energy is simulated as a continuous energy loss by the incident particle. There are two use cases: in case of a test beam (TB) study, one wants to precisely describe measured data and avoid systematic shift in the reconstruction of a cluster position due to incident δ–electron. Such a shift might be comparable to detector precision, i.e. several μm. As a solution, we recommend to set the cut so that $T_{\text{cut}} \ll MPV$, which automatically generates a realistic number of δ–electrons. In a full simulation, on the other hand, the main concern is speed, which is related to the number of simulated particles. In this situation, the preferrable choice is $T_{\text{cut}} \gg MPV$. In order to demonstrate that the amount of δ–electrons is far from being negligible and to study how they contribute to the energy distribution tail, we have simulated energy losses in 75 μm thick silicon and set $T_{\text{cut}} \ll MPV$ (see Fig. 3).

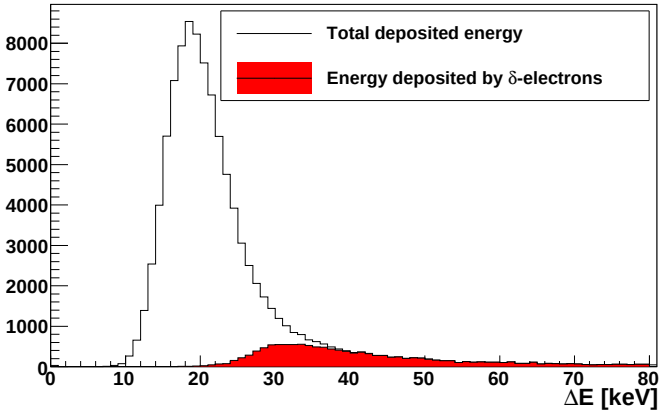

Figure 3: Deposited energy by 0.5 GeV/c pions in 75 μm thick silicon (threshold cut set to 0.4 μm). Red histogram corresponds to the fraction of deposited energy generated by δ-electrons.

The last issue concerns the definition of a sensitive detector and Geant4 step size calculation. In a full simulation, we use the default Geant4 optimal calculation of individual steps (2-3 steps per detector) and accumulate them to create 1 SimTrackerHit per particle and detector (except for loopers). The main advantage of such procedure is its simplicity (1 MC particle ↔ 1 SimTrackerHit) and speed. The disadvantage is that fluctuations are not simulated precisely and have to be re-sampled at digitization level again. In case of detector resolution studies (no speed issues) we force Geant4 to set the step size comparable to detector spatial resolution and thus simulate the fluctuations precisely. For comparison of different approaches see Fig. 4.

4. Digitization

Digitization is the simulation of detector response to ionizing particles and/or photons in magnetic field, based on detector physics. We implemented the digitization in two new Marlin packages: SiPxlDigi, simulating the response of a DEPFET pixel detector, and SiStripDigi, simulating the response of either single- or double-sided micro-strip detector. We would note that the implementation is very generic and can be easily adapted to various pixel and/or micro-strip technologies.

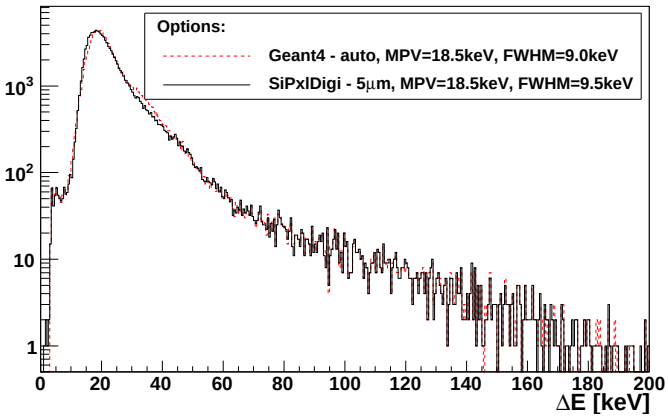

Figure 4: Comparison of energy loss fluctuations by 0.5 GeV/c pions in 80 μm thick silicon generated at Geant4 level, with MPV = 18.5 keV and FWHM = 9.0 keV (red dashed line), versus digitization level, with MPV = 18.5 keV and FWHM = 9.5 keV (black solid line). To emphasize agreement in distribution tails, log-scale is used.

4.1 Geometry and Data Flow

At the input, the packages require SimTrackerHits collected within a detector integration time window. At the output, the TrackerPulses or TrackerHits (after clustering) are saved. All hits have relations to MC truth information and if more than one particle has contributed to the signal creation, the one with the highest weight is saved. The typical vertex geometry design consists of several silicon layers, each consisting of a few ladders and each ladder has usually more than one active sensor (right Fig. 5). In order to separate the physics model and geometry implementation, each package has its own geometry interface providing all necessary information. The whole digitization procedure is performed within the sensor local coordinate system, where for VXD it is defined as follows: x'-axis is perpendicular to the sensor plane and to the beam axis, y'-axis lies in a sensor plane and is perpendicular to the beam axis, z'-axis is parallel to the beam axis. Position $(0,0,0)$ is defined such as the x',y',z' coordinates are always positive (right Fig. 5).

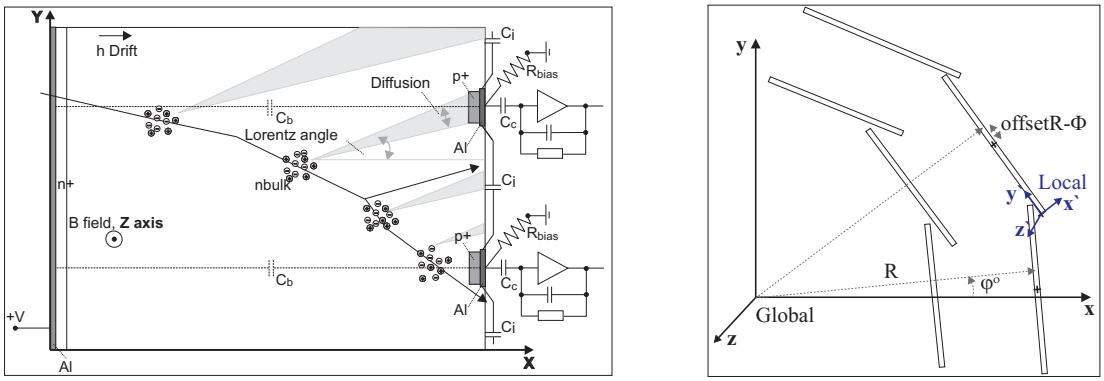

Figure 5: Left: Schematic layout of charge collection in silicon micro-strip detector. **Right:** Local $\vec{x'}$ (in blue) versus global $\vec{x}$ (in black) reference system with detailed VXD layer $\rightarrow$ ladder structure.

4.2 SiStripDigi - Physics Model

After a Geant4 particle enters a sensitive detector, bunches of e-h pairs are equidistantly generated along its path, with a user-defined segment of several μm (see left Fig. 5). The segment size is usually set at the level of the detector intrinsic resolution ≈ 5-20 μm. A fraction of charge, which is then assigned to each bunch of e-h pairs, is either calculated as a ratio of the total deposited charge, associated with each simulated hit, divided by the number of segments, or simulated through internal implementation of Geant4 `G4UniversalFluctuation` routine. The first method is preferred if Geant4 step size can be set to the required precision (TB studies). The latter approach is used when no limitation to Geant4 step size has been applied and one wants to take into account the energy loss fluctuations with the required spatial accuracy. As the fluctuation depends on particle type and its energy, detailed calculations of mean ionisation losses are required by the `G4UniversalFluctuation` and thus different Geant4 models have been utilized: `G4BetheBlochModel` for hadrons, `G4MuBetheBlochModel` for muons and `G4MollerBhabhaModel` for electrons & positrons [4]. The disadvantage of that approach is that it may require a crosscheck with Geant4 (see Fig. 4). Finally, the number of created e-h pairs in each bunch is calculated and Poisson fluctuated. The energy needed to create an e-h pair is 3.65 eV.

All generated electrons (holes) are drifted in the electric field towards *n*-type (*p*-type) electrodes. As micro-strip sensors have a non-trivial distribution of the electric field and thus the calculation of the weighting field would be necessary (see [3]), we have simplified the micro-strip structure to a simple p-n junction. Importantly, we have retained the dependence of carrier mobility on temperature and carrier position x. The dependence is defined in (4.1) and v_m, E_c, β are temperature dependent parameters [6]. The strong dependence of mobility on temperature and corresponding intensity is illustrated in Fig. 6.

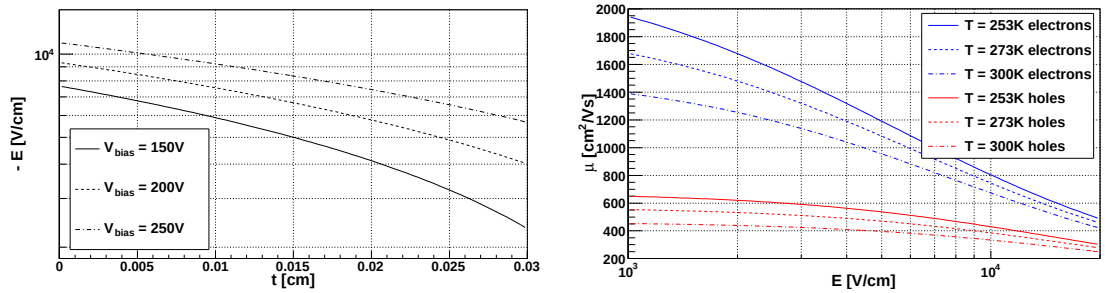

Figure 6: Left: Electric intensity versus position in a 300 μm thick silicon sensor for different bias voltages: 150 (solid), 200 (dashed) and 250 V (semi-dashed). **Right:** Corresponding mobility of electrons (blue) and holes (red) for different temperature: 253 (solid), 273 (dashed) and 300 K (semi-dashed).

Solving the following ordinary differential equation (4.1):

$$v(x(t)) = \mu E(x) \quad \begin{cases} E(x) = -\left(\frac{V+V_{dep}}{d} - \frac{2xV_{dep}}{d^2}\right) \\ \mu(E(x),T) = \left(\frac{v_m/E_c}{(1+(E(x)/E_c)^\beta)^{1/\beta}}\right) \end{cases} \tag{4.1}$$

where v stands for velocity, μ for mobility, E for intensity, V_{dep} for depletion voltage, V for bias voltage and d for detector thickness, one gets the carrier drift time t_{drift}. The time is used to estimate

the effect of diffusion, where diffusivity D is calculated using the Einstein relation (4.2):

$$D = \frac{kT}{q}\bar{\mu} \quad \longrightarrow \quad \sigma = \sqrt{2Dt_{\text{drift}}} \tag{4.2}$$

Here, k represents the Boltzman constant, T temperature, q carrier charge and $\bar{\mu}$ average mobility. As a fast numerical technique the Romberg integration method has been used. The algorithm exploits a very general idea of Richardson's deferred approach to the limit, where a function is first integrated using trapezium rule and then the result is extrapolated to the limit (see [7]). After the carrier bunches have migrated to the electrode surface, they are diffused by multiple collisions and final Gaussian distributions (with σ defined by (4.2)) are mapped to the strip layout. In the presence of a magnetic field B, the centers of such distributions are first shifted by Lorentz angle (4.3). The right panel of Fig. 7 illustrates the dependence of Lorentz angle on V_{bias} and carrier position x.

$$\tan(\vartheta_{\text{L}}) = \frac{\int_x^d \mu(E(x))rB\,dx}{\int_x^d dx} \quad \begin{cases} r = 1.13 + 0.0008(273 - T) & \text{for e} \\ r = 0.72 - 0.0005(273 - T) & \text{for h} \end{cases} \tag{4.3}$$

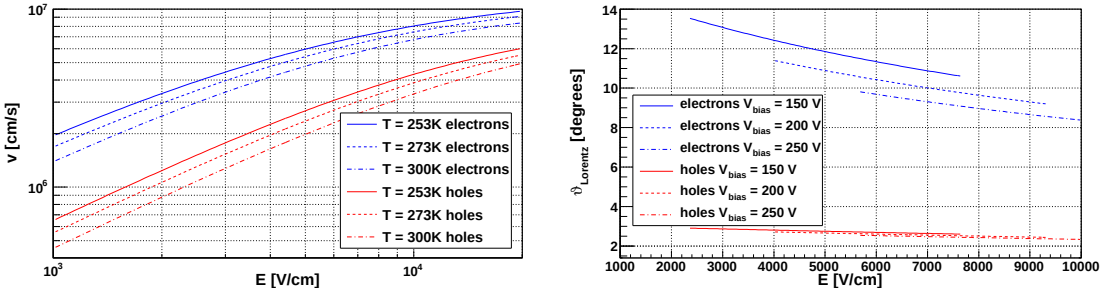

Figure 7: Left: Dependence of drift velocity versus intensity in a 300 µm thick sensor for electrons (blue) and holes (red), both for different temperature: 253 (solid), 273 (dashed) and 300 K (semi-dashed). **Right:** Lorentz angle in 1.5 T magnetic field versus intensity (corresponding to x position) for electrons (blue) and holes (red), both for different bias voltages: 150 (solid), 200 (dashed) and 250 V (semi-dashed), T=273 K.

Several electronic effects influence the final distribution of the collected charge on each strip. First, if the geometrical pitch is different from the read-out pitch, half of the charge is naturally collected by the left strip and the other half by the right strip. Furthermore, interstrip capacitance C_{i}, strip-to-backside capacitance C_{b} and capacitive coupling C_{c}, in case of AC coupled front-end electronics, are natural sources of mutual micro-strip crosstalk (charge sharing). Due to this effect, the charge collected on each read-out strip is redistributed again to neighbouring read-out strips as follows:

$$i_{\text{neighbour}} = \frac{i_{\text{strip}} C_{\text{i}}}{C_{\text{b}} + C_{\text{c}} + C_{\text{i}}} \tag{4.4}$$

An important capacitance here is the coupling capacitance, as it effectively enables to avoid the DC load by the continuously generated leakage current.

Second, common mode subtracted noise (CMS) is generated (using Gaussian distribution) and added to the signal. The typical sigma σ_{cms} of such a distribution usually depends on the length

(capacitance) of the sensor and might be from several hundreds to thousands of e. Finally, if the read-out is binary, the charge above a specified threshold is set to 1, and to 0 (discarded) otherwise. In case of an analog read-out, strips with a seed charge are found ($\sim 5\,\sigma_{\text{cms}}$ cut) and then the neighbouring strips with charge above a given threshold ($\sim 2\,\sigma_{\text{cms}}$) are added to the cluster.

After clustering, the double-sided or single-sided back-to-back detectors provide 2D spatial information, while single-sided can provide 1D information only. In case of shallow tracks, the number of hit strips, i.e. cluster size, might be higher than 3 and the center-of-gravity algorithm is not optimal anymore. Thus, the head-tail algorithm has been used, where q_{L} and q_{R} are the charges in the left- and rightmost strips and $\bar{q}_{\text{Inbtw}}$ is the average charge of intermediate strips [8].

$$x_{\text{COG}} = \frac{\sum\limits_{\text{cluster}} x_i q_i}{\sum\limits_{\text{cluster}} q_i} \qquad x_{\text{HeadTail}} = \frac{x_{\text{R}} + x_{\text{L}}}{2} + \frac{q_{\text{R}} - q_{\text{L}}}{2\bar{q}_{\text{Inbtw}}} pitch \tag{4.5}$$

In case of double-sided sensors, the position is calculated independently in both directions and then combined into a TrackerHit. This gives rise to artificial hits (ghosts). Together with a 1D or a 2D spatial position a covariance matrix is estimated. The procedure consists in generating reasonable statistics of muons passing individual detectors at several ϑ angles (20°, 30°, ...) and calculating the residuals (using MC truth information). The sigma of the gaussian, fitting the central 90% area of the residual distribution, defines then the TrackerHit resolution in the respective direction.

4.3 SiPxlDigi - Physics Model

Unlike a strip detector, the DEPleted Field Effect Transistor (DEPFET, [9]), represents a complex 2D device and a substantial simplification of in-detector physics processes is crucial for the digitization to perform in reasonable time. DEPFET can be described as a MOS-type field effect transistor integrated on a sidewards depleted *p*-on-*n* silicon detector (Fig. 8). The device combines the advantages of fully depleted silicon sensor with in-pixel amplification. By means of sidewards depletion an additional deep *n*-implantation (a potential minimum for electrons) is created right underneath the transistor channel (see right Fig. 8). This can be regarded as an internal gate and when a particle creates e-h pairs, holes drift to the back contact and electrons are collected in the internal gate, where they accumulate. The signal charge then leads to a change in the potential of the internal gate, resulting in a modulation of the channel current of the transistor. After read-out, the signal charge is cleared out by a positive voltage pulse at the clear contact.

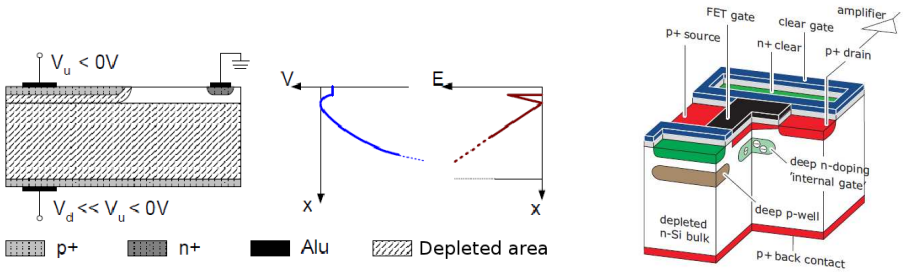

Figure 8: Left and **Middle:** Cross section of a sidewards depleted *p*-on-*n* silicon detector and corresponding distribution of electric potential. **Right:** 2D scheme of DEPFET pixel.

The generation of e-h pairs and continuous energy loss fluctuation is simulated in the same way as in SiStripDigi. What differs significantly is drift and diffusion (see Fig. 9). Based on full 3D device simulation[1], we have divided a pixel matrix (see right Fig. 9) into drift and non-drift regions, which are defined as regions with and without lateral field (y-axis) respectively. In drift

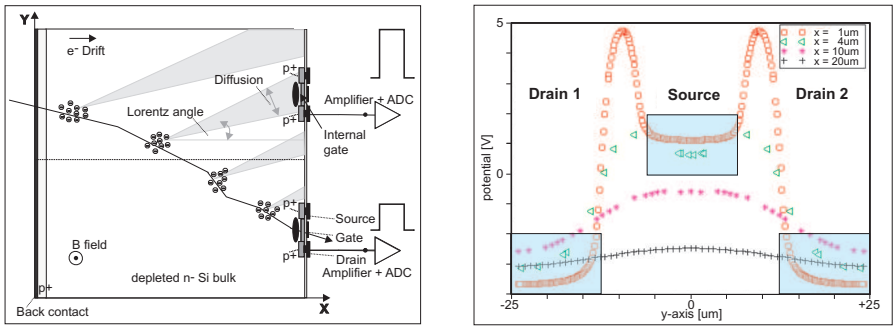

Figure 9: Left: A scheme of digitization procedure in DEPFET. **Right:** In-pixel potential distribution in y-direction for double-pixel structure and for different distances x=1, 4, 10, 20 µm from the bottom of the FET structure. Blue regions with no lateral field are emphasized.

regions, longitudinal drift (x-axis) of electrons in 1D parabolic shaped potential:

$$\phi(x) = \frac{qN_D}{2\varepsilon}x(d-x) + \frac{x}{d}(V_{\mathrm{x=d}} - V_{\mathrm{x=0}}) + V_{\mathrm{x=0}} \quad \text{for} \quad N_{\mathrm{D}} \ll N_{\mathrm{A}} \tag{4.6}$$

is performed up to a distance $\sim 10\,\mu$m below surface. From there, electrons achieve potential minimum by lateral drift. The total drift time determines, as in SiStripDigi, a diffusion sigma and thus influences the diffusion spread. In non-drift regions, electrons achieve the minimum by mere diffusion (simulated as a random walk), which significantly increases the drift time and the corresponding cluster size. In the presence of magnetic field, the charge distribution is first shifted by the Lorentz angle (the angle is given as an input parameter) and the final charge distribution is then mapped to the pixel layout, so no FET effect is directly simulated. In the above relation: q stands for carrier charge, ε for permitivity, d for detector thickness and N_{D} for the dopants concentration.

As DEPFET has almost no capacitive coupling between individual pixels, no charge-sharing effect is assumed. But there are other electronics effects, which are taken into account. A common-mode subtracted noise is added to the generated signal and an effect of ADC (analog-to-digital converter) is considered. In the ADC, the analog data are compared to digital thresholds (for a given number of bits: 5, 6, 7 and 8) and the total charge is then translated into digits. After digitization, clustering is performed and COG or head-tail algorithms are used.

4.4 Results and Models Validation

The physics model implemented in the SiStripDigi package has been validated against the ATLAS SCT test beam data. For the validation, a simulation of 180 GeV/c pions passing a binary read-out micro-strip detector has been performed. Concerning the simulation and test beam conditions, the binary threshold has been set to 1 fC, detector noise to $\sigma_{\mathrm{cms}} \approx 1500\,$e and telescope spatial

[1] performed by R. Richter, MPI Munich

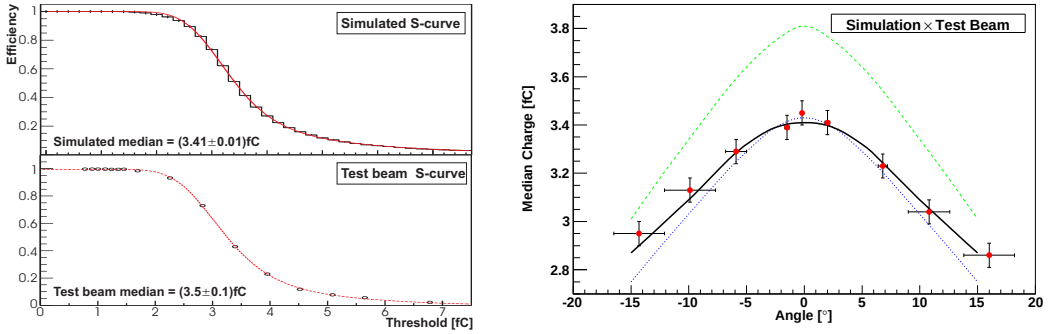

Figure 10: Left: Typical efficiency versus threshold for binary read-out detectors (S-curve): simulated median = (3.41 ± 0.01) fC (top), experimental median = (3.5 ± 0.1) fC (bottom). **Right:** Median collected charge versus incidence angle: simulations with drift and diffusion, no δ-electrons simulated (green), drift, diffusion and cross-talk effects (blue), and full simulation with δ-electrons and all digitization effects (black). Measurement results (test beam) are shown as red markers.

resolution to $\approx 5\,\mu$m. See [10] and [3] for details. To determine the importance of individual effects, the simulation has been performed with and without δ-electrons (difference between black and blue curve in Fig. 10), and with and without mutual cross-talk effect (difference between green and blue curve). The simulated S-curve (binary threshold scan) and the corresponding median, as well as the median charge versus incidence angle, perfectly agree with the measured data.

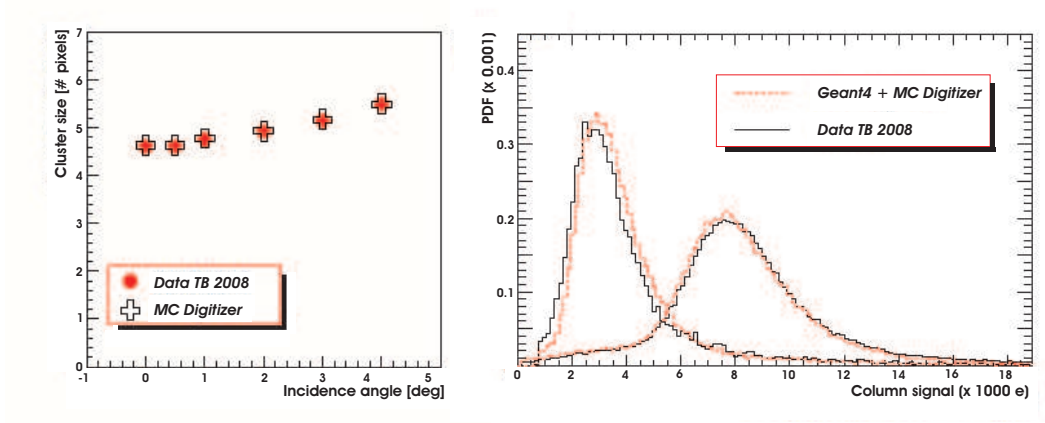

Figure 11: Left: Cluster size versus incidence angle. **Right:** Single-column signal distribution for inclined tracks. Right peak corresponds to passage through 450 µm thick silicon (no inclined tracks), left peak corresponds to effective passage through 50 µm thick silicon (inclined tracks) - signal extraction from the thick detector in order to estimate signal generation in thinned detectors.

The physics model implemented in SiPxlDigi has been validated against DEPFET test beam data [11]. For the validation a simulation of 120 GeV/c pions in a 450 µm thick DEPFET detector has been performed and particular focus has been given on correct explanation of cluster size measurements and signal charge generation, namely for inclined tracks. Both distributions are depicted in Fig. 11. Particularly interesting is the signal generation for inclined incident particles,

where the charge deposited in each pixel cell might be roughly the same as in future thinned down Belle II-like DEPFET detectors.

5. Summary

We have described our approach to the simulation of pixel detectors (DEPFETs) and silicon micro-strip detectors for the Belle II experiment using the ILC software framework. Furthermore, we have addressed possible issues connected with such simulation in Geant4 and explained in detail our physics models, which are used to describe in-detector physics processes to simulate the response of such devices. And finally, we have demonstrated the validity of the models against the test beam data.

References

[1] Belle II collaboration, *Belle II Technical Design Report*, arXiv: 1011.0352, KEK 2010

[2] ILC collaboration, [`http://ilcsoft.desy.de/portal`]

[3] Z. Drasal, *Simulation of Charge Collection in Semiconductor Microstrip Detectors*, Charles University, Prague 2006, [`http://www-ucjf.troja.mff.cuni.cz/diploma.php`]

[4] Geant4 collaboration, *Physics Reference Manual*, CERN, Geneve 2010, [`http://geant4.cern.ch/support/userdocuments.shtml`]

[5] H. Bichsel, *Straggling in Thin Silicon Detectors*, *Reviews of Modern Physics* **60** (663–699)

[6] M. Brigida et al., *A new Monte Carlo code for full simulation of silicon strip detectors*, *NIMA* **533** (322–343)

[7] J.Stoer, R.Bulirsch, *Introduction to Numerical Analysis*, 3rd edition Springer, New York 2002

[8] R. Turchetta, *Spatial resolution of silicon microstrip detectors*, *NIMA* **335** (44–58)

[9] J. Kemmer, G. Lutz, *New semiconductor detector concepts*, *NIMA* **253** (356)

[10] F. Campabadal et al., *Beam Tests of ATLAS SCT Silicon Strip Detector Modules*, *NIMA* **538** (384–407)

[11] L. Andricek et al., *Intrinsic resolutions of DEPFET detector prototypes measured at beam tests*, *NIMA* **638** (24–32)

PoS(Vertex 2011)027

PROCEEDINGS OF SCIENCE

Optimization of the Belle II Vertex Detector

Zbynek DRASAL[*†]
Charles University Prague, Czech Republic
E-mail: drasal@ipnp.troja.mff.cuni.cz

Kolja PROTHMANN[‡]
Max-Planck-Institut für Physik München, Germany
E-mail: kolja@mpp.mpg.de

At the high luminosities envisaged for the new Super Flavour Factory - SuperKEKB, the detection system closest to the beam pipe - a new Belle II silicon vertex detector will have to face an extremely harsh beam-related background and, consequently, high hit event rates, but still provide precise measurements of primary and secondary decay vertices. During the design phase of the vertex detector, consisting of two layers of pixel sensors and four layers of double-sided microstrip sensors, one has to carefully take into account all available technological options and optimise the detector design to fully reach the expected physics performance. For that reason we have initially utilized a modular design of ILC software framework and used it in full MC simulations for multi-parameter studies. In this paper we present the description of the Belle II vertex detector, our approach to the multi-parameter optimisation studies and finally, the obtained results: the detailed study of the expected material distributions of the vertex detector; optimisation study of the pixel detector layout with the final determination of the most optimal configuration; the influence of the slanted microstrip detectors in the forward region on the detector in-plane resolution and hit occupancy; and the expected impact parameter resolutions using or not using the two innermost pixel layers (to demonstrates the improvement of impact parameter resolutions by implementation of pixel sensors at Belle II). For consistency, the software chain has been validated against the official Belle software framework and cosmic muons data taken at Belle.

The XIth International Conference on Heavy Quarks and Leptons,
June 11-15, 2012
Prague, Czech Republic

[*]Speaker.

[†]This work has been supported by the Czech Science Foundation Grant No. 203/10/0777 and the Ministry of Education, Youth and Sports of the Czech Republic No. LA10033 and MSM0021620859.

[‡]This work has been supported by the DFG cluster of excellence "Origin and Structure of the Universe" of Germany.

PoS(HQL 2012)073

1. Introduction

SuperKEKB, an upgrade of the successful asymmetric e^+e^- collider and actual world luminosity record holder ($2.11 \times 10^{34}\,cm^{-2}s^{-1}$) KEKB (Tsukuba, Japan), will start commissioning by fall 2014 [1]. The main goal of the new Super Flavour Factory is to dramatically increase instantaneous statistics by a factor of 40 and thus deliver an integrated luminosity of 50 ab^{-1} by end of 2022. For that reason, the nano-beam option has been chosen. The beam pipe radius in the interaction region will be then only about 10 mm, which has a positive effect on the physics related to vertex reconstruction, but it presents a big challenge for the vertex detector itself due to harsh background environment. The background level generally increases roughly as the inverse square of the radius. In Belle, the innermost layers of the vertex detector consisted of microstrip sensors. But due to the expected large hit occupancy and, consequently, increased amount of false 2D hits, so-called ghosts, the innermost layers of the new precision vertex detector can no longer be composed of microstrip sensors and pixel sensors have to be used instead. The pixel detectors have much larger number of read-out channels, and thus lower occupancy, and will provide hits with true 2D information (unlike the strips combining two pieces of 1D information into a common hit, which is ambiguous). Furthermore, as low momentum particles ($\sim$ several hundreds of MeV) dominate at B-factories, multiple Coulomb scattering plays an important role in vertex reconstruction. Therefore, the material budget of the vertex detector, particularly of the innermost part, has to be seriously constrained. The pixel detector concept, based on the Depfet [2] technology, allows for such low material budget.

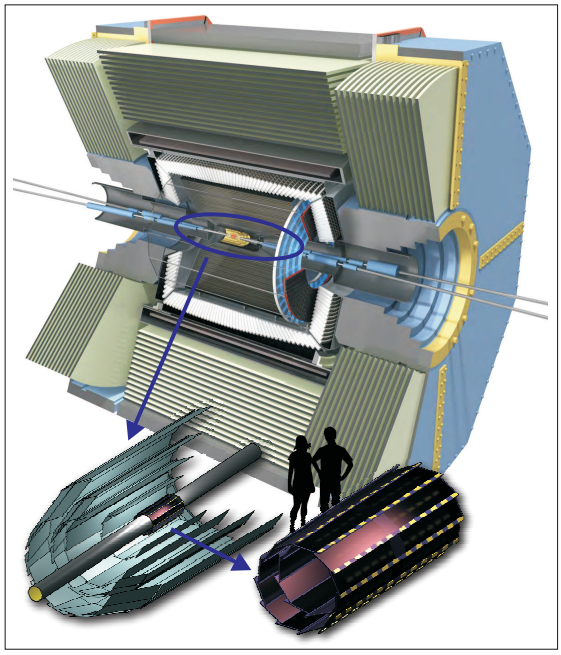

Figure 1: A scheme of the future Belle II detection system with a detail of the silicon vertex detector. The SVD together with PXD and a beam pipe is shown on the left, the standalone PXD on the right.

In order to deal with the challenging working conditions, particularly the increased background level and higher event rates, and, simultaneously, provide the required high precision measurements

of B meson decay vertices, a new design of the Belle II silicon VerteX Detector (VXD) is planned, see Fig. 1. The vertex detector will consist of 2 layers of thinned (75μm) Depfet-type pixel detectors (PXD), with radii of 14 and 22 mm, and 4 layers of double-sided microstrip detectors (SVD), with radii of 38, 80, 115 and 140 mm. The three outermost layers of SVD are extended to the forward region (slanted design) to fully cover, together with a central drift chamber (CDC), Belle II angular acceptance from 17° to 150° in polar angle.

2. Multi-Parameter Optimization Study & Software Framework

During the initial phase of each vertex detector project one has to carefully take into account the different aspects of detector technical design, such as layout, materials, cooling, etc., and choose the optimal configuration to fully achieve the planned physics performance. An ideal tool for such multi-parameter optimisation studies are simulations, allowing to try out all available design options. For that reason we have initially utilized a modular design of ILC software framework [3] and adapted its functionality to the Belle II needs. In the software framework we have implemented the full chain of the following tools: generator (Evtgen and KoralW for generation of Belle physics events and expected QED background respectively), Geant4 simulation - Mokka (with full material implementation of VXD geometry), digitization (pixel and microstrip silicon detectors simulation [4]). Furthermore, we have utilized the ILC software pattern recognition and adapted the tracking software (Marlin modules). For detailed scheme of the simulation chain see Fig. 2. In the simulations, the influence of following parameters (configurations) has been studied: material budget, layer radius, layer thickness, pixel geometry arrangements, pixel size, geometry setup in the forward region.

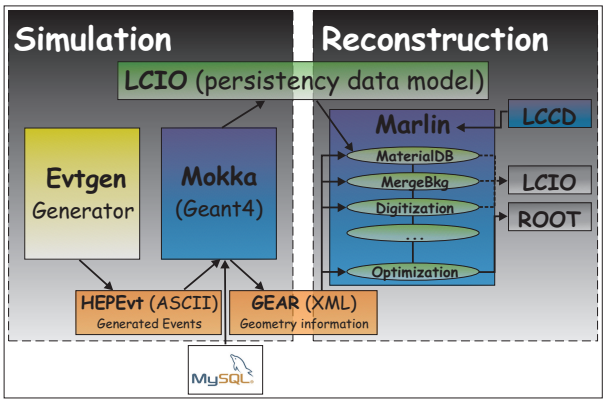

Figure 2: The scheme of software simulation and reconstruction chain (based on ILC software framework).

2.1 The Expected Material Budget of the VXD

The expected material distributions of the whole vertex detector have been studied using Geant4 simulations for two different options (Fig. 3). One with a barrel-like geometry configuration in the forward region, the other one with a conical-like geometry, i.e. with SVD with slanted sensors in the forward part. The latter represents the current Belle II baseline configuration.

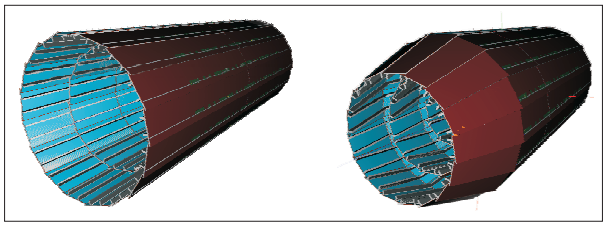

Figure 3: Vertex detector geometry in two options, with the barrel-like geometry in the forward region (barrel-like SVD), depicted on the left, the other one with the conical-like geometry in the forward region (conical-like SVD), depicted on the right.

The following key components have been implemented: a beryllium beam pipe with a 10μm thick golden foil (meant as a protection against soft synchrotron radiation) and a cooling gap filled with paraffin as a cooling medium, active PXD silicon sensors together with their passive parts (silicon rims, support and electronics chips, so-called switchers), and, finally, active SVD silicon sensors together with their passive parts (sandwich carbon fiber ribs, thermal and eletrical insulation (Rohacell layer), kaptons, read-out chips and a steel cooling pipe filled with CO_2 as a cooling medium). The parameters of the baseline geometry, used in the simulations, are summarized in Tab. 1, the results are shown in Fig. 4. Comparing the two options one can clearly see the substantial increase in material budget for the SVD barrel-like geometry in the region from 17° to 45°, which grows up by 50 %.

	R [mm]	**#Ladders**	**#Sensors**	**ϑ [deg]**
PXD layer 1	14	8	2	0.0
PXD layer 2	22	12	2	0.0
SVD layer 1	38	8	2	0.0
SVD layer 2	80	10	3	11.9
SVD layer 3	115	14	4	17.2
SVD layer 4	140	17	5	21.1

Table 1: The parameters of Belle II baseline geometry with slanted detectors in the forward region.

2.2 Optimization Study of the Depfet Pixel Layout

The Depfet pixel sensors can be manufactured in several layout options. The final physics performance, for different options, can be efficiently studied with single particles (0.5 GeV muons), generated at the unsmeared e^+e^- interaction point with selected values of polar angle θ and uniformly distributed in azimuth ϕ. For evaluation, we have used the quantity of the in-plane (intrinsic) resolution in both sensor directions: in R-Φ plane (perpendicular to the beam) and Z direction (parallel to the beam). The first option, Fig. 5, have been a study of constant (CPS) versus variable (VPS) pixel size in Z direction. The study has been performed for two configurations: with 800 pixels in Z ($p_1 \sim 123\,\mu$m, $p_2 \sim 147\,\mu$m for CPS and $p_1 \sim 117-178\,\mu$m, $p_2 \sim 145-174\,\mu$m for VPS, where p stands for the pitch of the first and second layer respectively) and with 1600 pixels

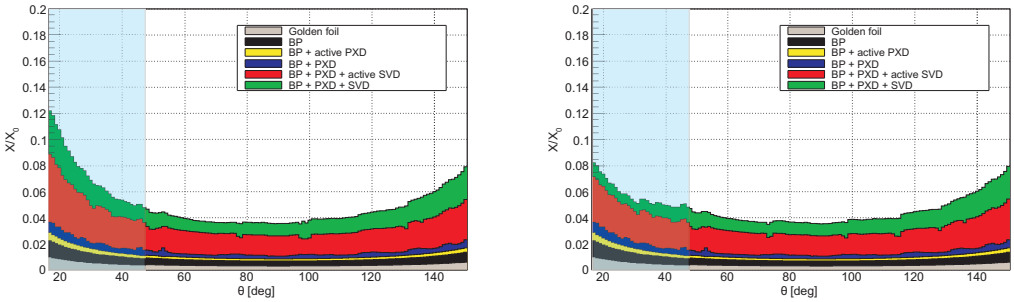

Figure 4: Expected material distributions obtained from Geant4 simulation: SVD barrel-like geometry on the left, SVD conical-like geometry on the right. The individual bands correspond to: the beam pipe golden foil, beryllium beam pipe and cooling gap filled with paraffin, active PXD sensors, passive PXD material (silicon rims, support and electronics chips), active SVD sensors, passive SVD material (sandwich carbon fiber ribs, Rohacell layer, kaptons, read-out chips and the steel cooling pipe filled with CO_2.

in Z, the baseline, ($p_1 \sim 61\,\mu$m, $p_2 \sim 73\,\mu$m for CPS and $p_1 \sim 38-177\,\mu$m, $p_2 \sim 56-174\,\mu$m for VPS). The key idea of the variable pixel size consists in keeping the cluster size (and thus resolution) constant along the Z-axis, independently on the polar angle of emitted particles. This can be practically done by decreasing the pixel size gradually from the edges of each ladder to the point closest to the interaction point. So, we have first geometrically evaluated (using a line from the interaction region) the optimal pixel size starting at the edges of the ladder, further we have kept on decreasing the pitch until we reached the minimal size, limited by the given number of pixels in Z. The minimal pixel size has been used then for the remaining pixels to the point (on the ladder) closest to the interaction point. For details, see schematic drawing in Fig. 6.

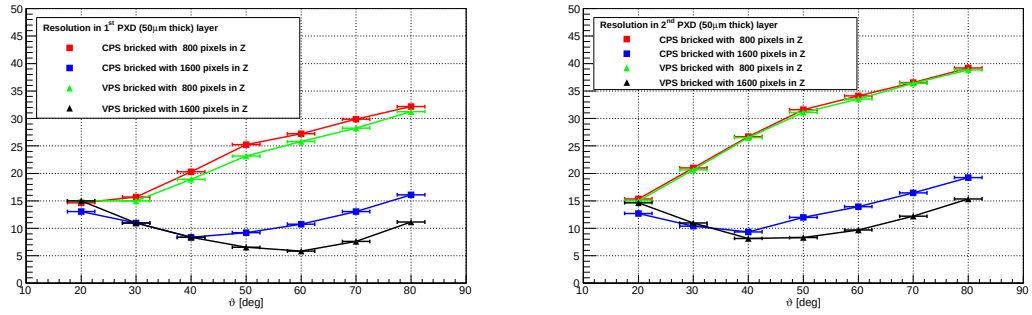

Figure 5: PXD in-plane resolution [μm] in Z direction for different design options: CPS with bricked structure, 50 μm pitch in R-Φ and 800 pixels in Z (filled red squares); CPS with bricked structure, 50 μm pitch in R-Φ and 1600 pixels in Z (filled blue squares); VPS with bricked structure, 50 μm pitch in R-Φ and 800 pixels in Z (filled green triangles); VPS with bricked structure, 50 μm pitch in R-Φ and 1600 pixels in Z (filled black triangles). The resolution for the first layer is depicted on the left side, for the second layer on the right side. PXD thickness has been set to 50 μm.

The studies have been performed for 50 μm thick PXD sensors, the originally considered design, and the in-plane resolution has been defined as a root mean square of the 95 % area of in-

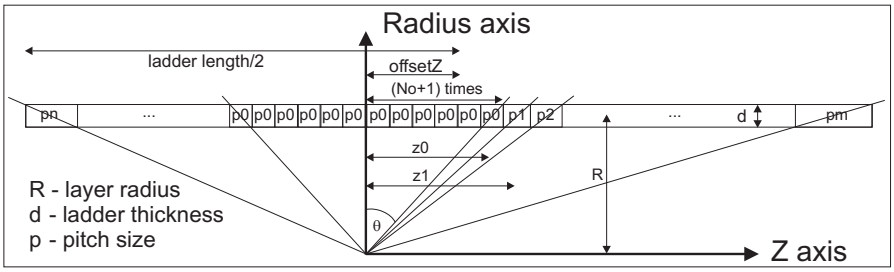

Figure 6: The schematic drawing of VPS option. The p_0 parameter corresponds to the pitch of smallest pixels, repeated $(N+1)$ times, then the pitch increases continuously until the ladder edge is reached. Due to the asymmetry of ladder position with respect to the interaction point, the pitch on the left is of different size than on the right.

plane signal residuals distribution. Such a definition has excluded non-gaussian tails and provided good stability independently on the polar and azimuthal angle of reconstructed particles.

The second line of optimisation studies, Fig. 7, has been the study of bricked versus non-bricked structure in R-Φ plane, where the bricked stands for a layout with pixels shifted by a half of pitch every even row. The key idea of bricked structure consists in increasing signal/noise ratio for edge pixels in clusters of size higher than one in Z, and thus increasing resolution for non-perpendicular tracks. The pixel pitch has been set to two sizes: $p \geq 50\,\mu$m for unbricked structure and $p \geq 70\,\mu$m for bricked structure (lower not technologically achievable).

Due to the technological limits on pixel pitch (bricked technology available for $p \geq 70\,\mu$m only) and expected gain in resolution limited to the forward region only, the unbricked layout has been preferred. The variable pixel size brings significant improvement in resolution in the area where most of the produced particles fly (due to B-factory boost), but requires internal implementation of extra drift fields in Depfet (too large pixels at the edges of sensors would lead to inefficiencies in charge collection), which complicates the pixel design. So, the Depfet baseline has been finally fixed to: 75 μm thick PXD with CPS along Z-axis and unbricked structure in R-Φ plane and will consist of: 2×768 rows in Z ($256 \times 55\,\mu$m $+ 512 \times 60\,\mu$m for the first layer, $256 \times 70\,\mu$m $+ 512 \times 85\,\mu$m for the second layer), 250 columns $\times$ 50 μm pitch in R-Φ.

2.3 Optimization Study of the SVD Forward Region

Due to the asymmetry of energy of colliding particles at the SuperKEKB factory, the SVD design with slanted sensors in the forward region brings a significant reduction in terms of the number of needed sensors to fully cover the required Belle II acceptance region. On the other hand, the mechanical design and consequently, mechanical stability, alignment, etc. are more challenging than for the same geometry, but with extended (barrel-like) sensors in the forward region. In order to see the difference in terms of material budget (see section 2.1), detector in-plane resolution (defined as a root mean square of the 90 % area of signal residuals distribution) and final hit occupancy (correlated with a cluster size and important for efficiency of charged particles reconstruction), we have studied the cluster size (Fig. 8) and in-plane resolution (Fig. 9) in Z direction. There is no difference between the geometries in R-Φ plane.

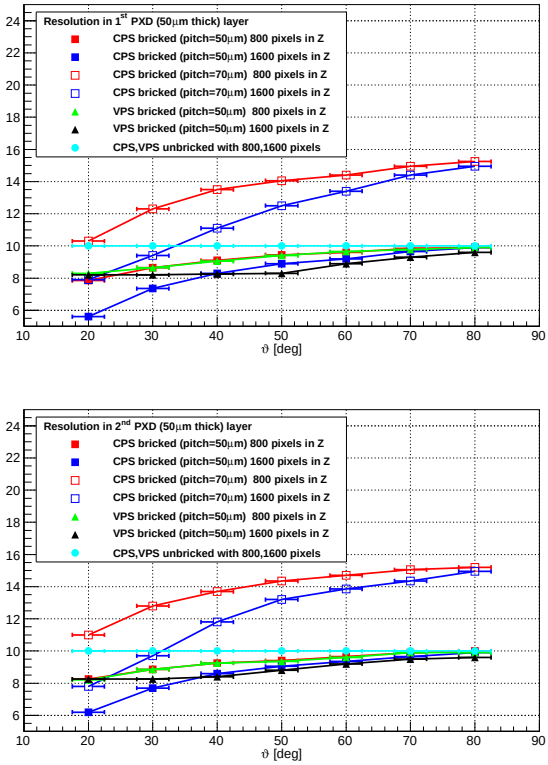

Figure 7: PXD in-plane resolution [μm] in R-Φ direction for different design options: CPS with bricked structure, 50 μm pitch in R-Φ and 800 pixels in Z (filled red squares); CPS with bricked structure, 50 μm pitch in R-Φ and 1600 pixels in Z (filled blue squares); CPS with bricked structure, 70 μm pitch in R-Φ and 800 pixels in Z (open red squares); CPS with bricked structure, 70 μm pitch in R-Φ and 1600 pixels in Z (open blue squares); VPS with bricked structure, 50 μm pitch in R-Φ and 800 pixels in Z (filled green triangles); VPS with bricked structure, 50 μm pitch in R-Φ and 1600 pixels in Z (filled black triangles); and CPS or VPS with unbricked structure, 50 μm pitch in R-Φ and 800 or 1600 pixels in Z (filled cyan circles). The resolution for the first layer is depicted on the top, for the second layer at the bottom. PXD thickness has been set to 50 μm.

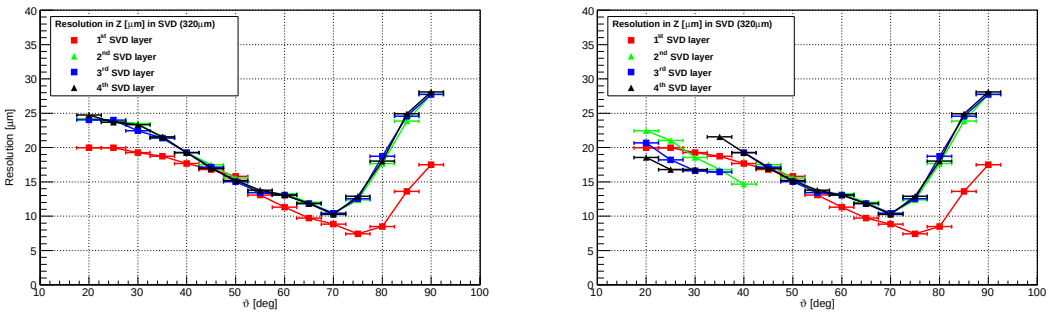

Figure 8: SVD in-plane resolution [μm] in Z for different vertex detector geometry options: SVD barrel-like (left) and SVD conical-like (right). The first layer is depicted with red, second with green, third with blue and fourth with black colour. SVD sensors are 320 μm thick.

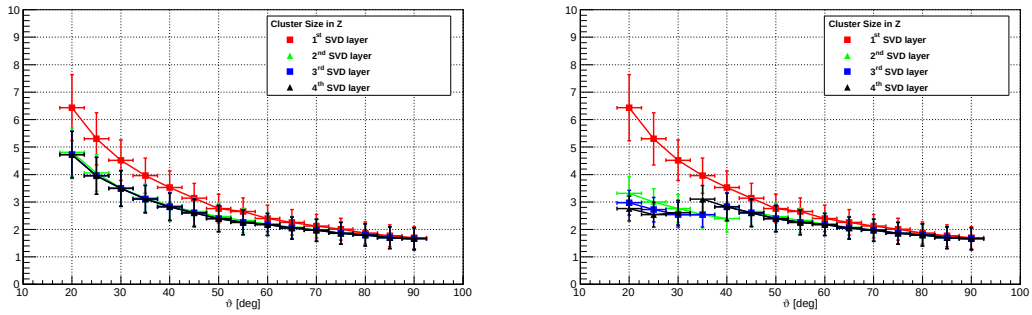

Figure 9: SVD cluster size in Z direction for different vertex detector geometry options: SVD barrel-like (left) and SVD conical-like (right). The first layer is depicted with red, second with green, third with blue and fourth with black colour. SVD sensors are 320 μm thick.

2.4 Impact Parameter Studies

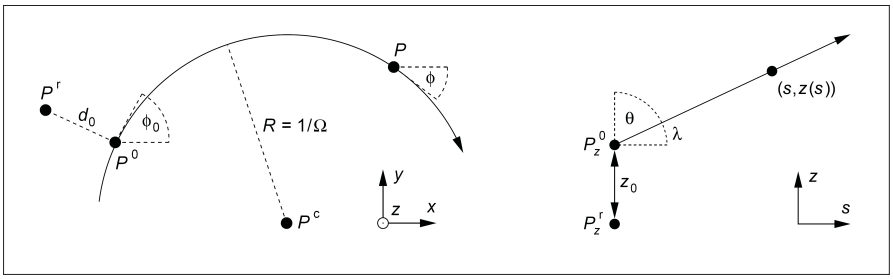

Figure 10: Definition of impact parameters in R-Φ plane - d_0 and in $s-Z$ plane - z_0, where s denotes the length of the trajectory arc in R-Φ plane. All parameters are expressed with respect to the reference point P^{r}, the point of closest approach is denoted as P^0.

The resolution of impact parameters (IP) - d_0 and z_0, defined (Fig.10) as the projections of distance from the point of closest approach P^0 to the reference point P^{r} (identical to the origin for single particle studies and to the vertex for decay studies), are a good measure of the overall performance of the tracking system and are used to find the optimal tracker (vertex detector) configuration. The main reason is that the parameters naturally test the interplay between the geometrical setup of individual sensitive detectors and physics effects, particularly multiple Coloumb scattering and ionization losses. The mathematical formula describing the IP resolution σ can be then written as a sum of two terms: intrinsic detector resolution and the term related to multiple Coloumb scattering, which depends on particle momenta:

$$\sigma = \sqrt{a^2 + b^2/\tilde{p}^2} \quad \text{often written as} \quad \sigma = a \oplus b/\tilde{p}$$

, where

$$\tilde{p} = p\beta \sin\vartheta^{3/2} \quad \text{stands for} \quad d_0 \tag{2.1}$$

$$\tilde{p} = p\beta \sin\vartheta^{5/2} \quad \text{stands for} \quad z_0 \tag{2.2}$$

More details about how d_0 and z_0 are defined in the ILC software framework can be found in [5].

In order to validate the whole software chain in the ILC software framework, we have first studied the IP resolution $\sigma(z_0)$ for positive muons reconstructed from the J/Ψ decay (coming from the decay of neutral B-mesons) in both BASF [6] and ILC framework. (For that purpose we have implemented the Belle detector geometry.) Further, we have compared achieved results with the distributions from Belle cosmic muons measurements [7]. The IP resolution curves are depicted in Fig. 11 and clearly demostrate a very good agreement between the Belle standard simulation tool BASF and the new software used here.

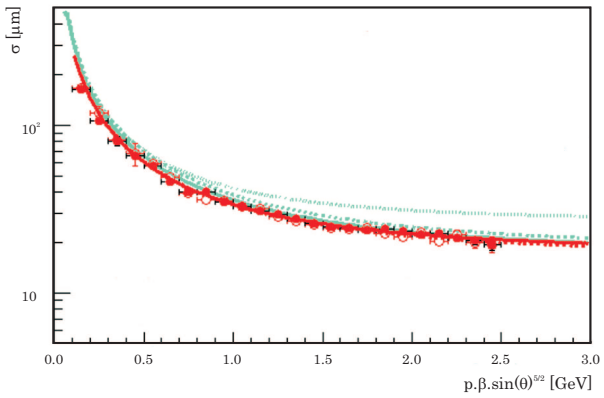

Figure 11: IP resolution - $\sigma(z_0)$ for positive muons reconstructed from J/Ψ decay in BASF (red open circles, red dashed curve) and ILC software (red filled circles, red solid curve). In addition, the resolutions from Belle data/MC cosmic muons are depicted: data (dotted cyan curve - upper curve), Monte Carlo in BASF (dashed cyan curve - lower curve).

Finally, we have studied the expected performance of the Belle II vertex detector: PXD+SVD for typical Belle II particle energies, see the resolution region below 1 GeV in Fig. 12 and compared obtained results with the performance of SVD only, Fig. 12. The IP resolution has been defined as the sigma of double gaussian core (for fitter stability), where the double gaussian has been fitted in the 90 % area, the non-gaussian (exponential) tails have been excluded. The obtained results clearly demonstrate the substantial improvement in IP resolution due to the installation of PXD at Belle II:

Parameters for PXD+SVD:

$$\sigma(d_0) = (9.7 \pm 0.5) \oplus (11.1 \pm 0.7)\mu\text{m}/\tilde{p} \quad (2.3)$$

$$\sigma(z_0) = (12.1 \pm 0.5) \oplus (17 \pm 1)\mu\text{m}/\tilde{p} \quad (2.4)$$

Parameters for SVD only:

$$\sigma(d_0) = (13.8 \pm 0.9) \oplus (37 \pm 2)\mu\text{m}/\tilde{p} \quad (2.5)$$

$$\sigma(z_0) = (15 \pm 1) \oplus (44 \pm 2)\mu\text{m}/\tilde{p} \quad (2.6)$$

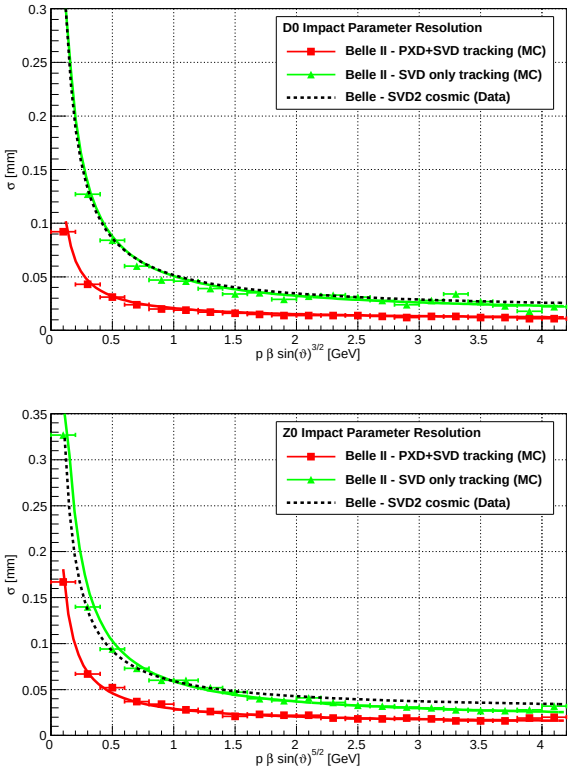

Figure 12: The impact parameter resolution in R-Φ plane - $\sigma(d_0)$ (on the left) and in Z direction - $\sigma(z_0)$ (on the right) for Belle II detector geometry. Two options have been simulated: results from the combined PXD and SVD tracking (red squares) and from SVD only tracking (green triangles). For comparison, in dashed curve, the resolution of Belle vertex detector (SVD2), obtained from the cosmic data, has been depicted.

For comparison, the resolution of Belle vertex detector (SVD - version 2) [7], [8] has been depicted. It clearly shows how the PXD detector improves the IP resolution also compared to the Belle experiment.

3. Summary

For the optimisation studies of the Belle II experiment we have developed a full simulation, digitization, pattern recognition and tracking chain in the ILC software framework. We have validated its functionality comparing impact parameter resolutions with those obtained in the Belle software framework (BASF). Concerning the optimisation results, we have studied the expected material budget of the future vertex detector (Belle II PXD and SVD) and significantly helped to understand the resolution of the new pixel and micrstrip detectors. Moreover, we have contributed to the final determination of the Depfet pixel layout. And finally, we have studied the improvement of impact parameter resolutions due to the installation of PXD vertex detector at the Belle II experiment and compared the results with those of a vertex detector consisting of SVD only.

References

[1] Belle II collaboration, *Belle II Technical Design Report*, arXiv: 1011.0352, KEK 2010

[2] DEPleted Field Effect Transistor, [`http://www.depfet.org`]

[3] ILC Software, official web page, [`http://ilcsoft.desy.de/portal`]

[4] Z. Drasal, K. Prothmann, B. Schwenker, *Silicon Simulation Code for Belle II and ILC*, PoS (Vertex 2011), **027**

[5] T. Krämmer, *Track Parameters in LCIO*, [`www-flc.desy.de/lcnotes/notes/LC-DET-2006-004.pdf`]

[6] BASF, official Belle Analysis Software, [`http://belle.kek.jp`]

[7] H.Ishino et al., *Alignment Method for the SVD2 and Its Performance*, internal Belle note **BN715**

[8] H.Aihara et al., *Belle SVD2 vertex detector*, Nuclear Instruments and Methods in Physics Research A (2006), **568**, issue 1, p. 269–273

12 Conclusions and Outlook II

In the second part of the thesis we have presented, first, our approach to the simulation of the response of silicon vertex detectors to ionizing particles and/or gamma, and second, the optimization studies of the vertex detector under development for the Belle II experiment.

The digitization procedure has been in detail discussed with an accent on its interplay with the Geant4 framework; particularly, the questions concerning the right choice of a suitable physics model, generation of δ-electrons and definition of sensitivity in Geant4 software have been addressed. Further, the digitization model in both pixel and micro-strip detectors, together with clustering procedures are discussed. The peculiarities typical for the 2D Depfet pixel devices, compared to silicon micro-strip devices (simplified as a p-n junction), are explained too and our proposed solution is given in detail. Finally, the verification of developed software using various test-beam data is demonstrated.

In the optimization studies we have dealt with several proposed options. First, we have demonstrated the expected material budget of the overall VXD in two configurations: with and without V-shaped like sensors in the forward region. Then, we have studied the impact of several pixel layout configurations on the final VXD performance, expressed in terms of so-called in-detector resolution. Namely, we have focused on scenarios with: bricked structure, constant pixel size along Z direction and a completely novel idea of variable pixel size along Z axis. The final decision made by Depfet collaboration has been strongly supported by results from these simulation studies, and the decision follows: the Depfet active sensors will be 75 µm thick with constant pixel size along Z-axis and unbricked structure in R-Φ plane; further, the Depfet sensors will consist of 2×768 rows in Z ($256 \times 55\,\mu\text{m} + 512 \times 60\,\mu\text{m}$ for the first layer and $256 \times 70\,\mu\text{m} + 512 \times 85\,\mu\text{m}$ for the second layer) and of 250 columns with 50 µm pitch in R-Φ plane. The final study, and probably the most important one, has been an estimation of VXD performance in terms of tracking capabilities. For that purpose the software results have been first validated against Belle software framework, BASF, and then the impact parameter resolutions in R-Φ plane and Z direction

have been estimated as:

Parameters for PXD+SVD:

$$\sigma(d_0) = (9.7 \pm 0.5) \oplus (11.1 \pm 0.7)\mu\text{m}/\tilde{p} \quad (12.1)$$
$$\sigma(z_0) = (12.1 \pm 0.5) \oplus (17 \pm 1)\mu\text{m}/\tilde{p} \quad (12.2)$$

Parameters for SVD only:

$$\sigma(d_0) = (13.8 \pm 0.9) \oplus (37 \pm 2)\mu\text{m}/\tilde{p} \quad (12.3)$$
$$\sigma(z_0) = (15 \pm 1) \oplus (44 \pm 2)\mu\text{m}/\tilde{p} \quad (12.4)$$

which clearly demonstrates a significant improvement right due to installation of PXD within the Belle II VXD.

During the work on optimization studies a common effort to develop a new Belle II software framework has slowly arisen. The ILC software, though very successful for our needs, was developed by a different collaboration, and from base principals, couldn't provide a full simulation framework for the Belle II experiment. It simply lacks sufficient support for any changes inside the collaboration. Nevertheless, the digitization software, successfully tested using test-beam data, and ideas used in these studies have been gradually transferred by VXD collaboration into this new framework, named basf2 [62], and the software remain under further development.

References

[1] Depfet web page [online], `http://www.depfet.org`

[2] Belle II web page [online], `http://belle2.kek.jp`

[3] Belle web page [online], `http://belle.kek.jp`

[4] K. Abe *et al.* (Belle Collab.), SuperKEKB Letter of Intent [online], `http://superb.kek.jp/documents/loi/loi.html`

[5] T. Abe *et al.* (Belle II Collab.), Belle II Technical Design Report, arXiv:**1011.0352** (2010)

[6] Private communication with B. Schwenker, Georg-August-Universität Göttingen, Germany

[7] Private communication with K. Prothmann, Max-Planck Institute München, Germany

[8] Z. Drasal, K. Prothmann, B.Schwenker, PoS (Vertex2011) **027** (2011)

[9] Z. Drasal, K. Prothmann, PoS (HQL 2012) **073** (2012)

[10] N. Cabbibo, Phys. Rev. Letters **10**, 531 (1963)

[11] M. Kobayashi and T.Maskawa, Prog. of Theor. Physics **49**, 652 (1973)

[12] B. Aubert *et al.* (BaBar Collab.), Phys. Rev. D **79**, 072009 (2009)

[13] I. Adachi *et al.* (Belle Collab.), Phys. Rev. Letters **108**, 171802 (2012)

[14] L. Wolfenstein, Phys. Rev. Letters **51**, 1945 (1983)

[15] I.I. Bigi and A.I. Sanda, CP Violation, Cambridge monographs on particle physics, nuclear physics and cosmology Vol. 9, Cambridge University Press (2000)

[16] K. Nakamura *et al.* (Particle Data Group), J. Phys. G **37**, 075021 (2010)

[17] F. Fang, Measurement of Branching Fractions and CP Violation in $B \to \eta_C K$ and Observation of $B^{\pm} \to p\bar{p}K^{\pm}$, Dissertation, University of Hawaii (2003)

[18] Y. Amhis *et al.* (Heavy Flavor Averaging Group), arXiv:1207.1158 (2012)

[19] B. Aubert *et al.* (BaBar Collab.), Phys. Rev. D **80**, 112001 (2009)

[20] B. Aubert *et al.* (BaBar Collab.), Phys. Rev. D **69**, 052001 (2004)

[21] A. Abashian *et al.* (Belle Collab.), Nuclear Instruments and Methods in Physics Research A **479**, 117 (2002)

[22] S. Kurokawa, E. Kikutani, Nuclear Instruments and Methods in Physics Research A **499**, 1, and other papers included in this volume

[23] B. Barish *et al.* (CLEO Collab.), Phys. Rev. Letters **76**, 1570 (1996)

[24] D. G. Cassel, Int. J. Mod. Phys. **A**, 17, 2951 (2002)

[25] Geant3 web page (CERN-IT Division) [online], `http://wwwasd.web.cern.ch/wwwasd/geant`

[26] Z. Natkaniec *et al.* (Belle SVD Group), Nuclear Instruments and Methods Physics Research A **560**, 1 (2006)

[27] Belle Collab. internal web page [online], `http://belle.kek.jp/secured/nbb/nbb.html`

[28] T. Iijima *et al.* (Belle ACC Group), Nuclear Instruments and Methods Physics Research A **453**, 321 (2000)

[29] B. Casey, Hadron B, Belle internal note #**390**

[30] H. Tajima *et al.*, Nuclear Instruments and Methods in Physics Research A **533**, 370 (2004)

[31] S. Nishida, Study of Kaon and Pion Identifiation Using Inclusive D^* Sample, Belle internal note #**779**

[32] F. Fang, Study of $K_S \to \pi^+\pi^-$ Selection, Belle internal note #**323**

[33] See for example: G. Cowan, Statistical Data Analysis, p. 51, Oxford University Press (2002)

[34] G. C. Fox and S. Wolfram, Phys. Rev. Letters **41**, 1581 (1978)

[35] K. Abe *et al.* (Belle Collab.), Phys. Rev. Letters **87**, 101801 (2001)

[36] T. Higuchi, Vertexing, Belle internal document, Belle Analysis School (2009)

[37] H. Tajima *et al.* (Belle Collab.), Nuclear Instruments and Methods Physics Research A **533**, 370 (2004)

[38] T. Higuchi, Time-Dependent Analysis, Belle internal document, Belle Analysis School (2009)

[39] H. Kakuno *et al.* (Belle Collab.), Nuclear Instruments and Methods Physics Research A **533**, 516 (2004)

[40] K. Sumisawa, Resolution Function & Wrong Tag Fractions, Belle internal document, CPFit (2011)

[41] E. White, Determination of K_S Efficiency and Systematic Uncertainty, Belle internal note #**1207**

[42] Minuit2 web page (CERN-IT Division) [online], `http://seal.web.cern.ch/seal/snapshot/work-packages/ /mathlibs/minuit/`

[43] ROOT TMath web page (CERN-IT Division) [online], `http://root.cern.ch/root/html534/TMath.html`

[44] B. Bhuyan, High $P_{\rm T}$ Tracking Efficiency Using Partially Reconstructed D^* Decays, Belle internal note #**1165**

[45] K. Miyabayashi, Measurement of time-dependent CP violation in $B^0 \to (c\bar{c})\ K^0$ decays with 772 M BB, Belle internal note #**1149**

[46] CKMfitter Group web page [online], `http://ckmfitter.in2p3.fr`

[47] O. Long *et al.*, Phys. Rev. D **68**, 034010 (2003)

[48] K. Hara, Study of tag side interference effect in time-dependent CP violating asymmetry measurement, Belle internal note #**872**

[49] H. Koji, Flavour Tagging, Belle internal document, Belle Analysis School (2009)

[50] T. Higuchi, Observation of CP Violation with B^0 Meson Decaying to the J/ψ K_S State, Dissertation, University of Tokyo, (2001)

[51] T. Higuchi, Resolution Function Update for ICHEP06, Belle internal note #**924b**

[52] Tatami software - version `2010mdlh` (Belle Collab.) [online - internal], `http://belle.kek.jp/secured/indirectcp/cpfit`

[53] QQ B meson decay event generator (CLEO Collab.) [online], `http://www.lns.cornell.edu/public/ CLEO/soft/QQ`

[54] J. W. Flanagan *et al.* (Belle Collab.), SuperKEKB Letter of Intent (Accelerator part) [online], `http://superb.kek.jp/documents/loi/loi.html`

[55] S. Hashimoto *et al.* (Belle Collab.), SuperKEKB Letter of Intent (Physics part) [online], `http://superb.kek.jp/documents/loi/loi.html`

[56] P. Raimondi, 2nd LNF Workshop on SuperB, Frascati, Italy (2006) [online], `http://www.lnf.infn.it/conference/superb06/talks/raimondi1.ppt`

[57] M. Baszczyk *et al.* (SuperB Collab.), SuperB Technical Design Report, arXiv:**1306.5655** (2013)

[58] Z. Dolezal *et al.* (Depfet Collab.), The PXD Whitebook [online - internal], `http://www.depfet.org/`

[59] ILC software framework (ILC Collab.) [online], `http://ilcsoft.desy.de/portal`

[60] S. Agostinelli *et al.*, Nuclear Instruments and Methods Physics Research A **506**, 250 (2003)

[61] J. Allison *et al.*, IEEE Transactions on Nuclear Science **53** No. 1, 270 (2006)

[62] A. Moll, Journal of Physics: Conference Series **331.3** (2011)